NORTHWESTERN UNIVERSITY

Experimental Investigation and Multi-Physics Computational Modeling for Assessment, Mitigation and Prevention of Concrete Deterioration

A DISSERTATION

SUBMITTED TO THE GRADUATE SCHOOL
IN PARTIAL FULFILLMENT OF THE REQUIREMENTS

for the degree

DOCTOR OF PHILOSOPHY

Field of Civil and Environmental Engineering

By

BOUSIKHANE Faysal

EVANSTON, ILLINOIS

September 2018

Abstract

Experimental Investigation and Multi-Physics Computational Modeling for Assessment, Mitigation and Prevention of Concrete Deterioration

BOUSIKHANE Faysal

Precise assessment of long-term aging and deterioration play a major role in life-time predictions of concrete structures. One of the primary challenges in studies of cementitious materials such as concrete comes from the fact that multiple chemical reactions are happening in parallel. Environmental conditions present another challenge as they can influence greatly chemical kinetics, further complicating the analysis. The deterioration mechanism studied in this thesis is a chemical reaction called Alkali Silica Reaction (ASR) wherein an expansive gel is formed causing significant concrete degradation over time. ASR induced degradation of concrete is first investigated through experimental methods to assess ASR affected concrete mechanical properties evolution over one year. The influence of environmental properties, aggregates silica content, aging, shrinkage, creep and sample geometry on ASR are fully characterized through a comprehensive experimental program involving destructive and non-destructive evaluations of reactive and non-reactive concrete samples at different stages.

While experimental investigations happen to be the first step in the study of physical phenomenons, practical limitations in physical testing have constantly led researchers to develop numerical models capable of modeling accurately concrete properties. Besides, the long term assessment of concrete properties evolution is only achievable through the development of powerful models that can couple realistically the aforementioned physical phenomenon. The Lattice Discrete Particle Model (LDPM), a three-dimensional mesoscale discrete model, is employed in this study to simulate the mechanical response of concrete at the level of coarse aggregate pieces. The LDPM is capable of characterizing strain localization, distributed cracking in tension and compression, and to reproduce accurately post peak softening behavior. The M-LDPM, an extension of LDPM, includes multiple models that describe heat transfer, moisture transport as well as ASR, creep, aging, shrinkage, fiber contribution to concrete strengthening and their full coupling. The M-LDPM is calibrated and validated by modeling the experimental results obtained during the initial phase of the ASR study.

High costs associated with concrete structure rehabilitation has pushed researchers to develop a new promising generation of self-healing concretes. As their name suggests, self-healing concretes are capable of mitigating damages associated with a given deterioration mechanism (ASR for example) by automatically regenerating themselves post-damage. This feature is crucial in the mitigation of deterioration mechanisms since fractures behave like hydraulic pathways, significantly increasing local permeability and promoting water ingress. The presented work includes an experimental study characterizing the effects cracks and of a self-healing admixture (Penetron) on concrete permeability. This study

is completed by the development calibration and validation of a multi-physics computational framework which couples successfully mechanical and moisture transport behavior in concrete.

Last but not least, prophylactic methods have been developed to counter and limit deterioration mechanism consequences. One example is the use of Fiber Reinforced Ultra High Performance Concrete (FRUHPC) mixes as overlays on cracked bridge decks. In this thesis, simulations were performed to identify the impact of various steel fiber types on the mechanical response of an ultra-high performance concrete (UHPC) developed by the US army Corps of Engineers. This type of concrete has outstanding mechanical properties in compression as well as in tension in comparison to regular concrete. The simulations were performed with the LDPM-F, an extension of the LDPM capable of modeling fiber effects.

Acknowledgements

Words cannot suffice to describe how thankful I am to Allah (s.w.t) for giving me that chance to join Northwestern University and work on my Doctorate degree.

I also would like to express my deepest gratitude to my adviser and mentor Professor Gianluca Cusatis for giving me this chance to learn and grow in his group. His valuable support at both intellectual and personal levels were key for me to complete my doctoral program.

I am particularly grateful for the advice given by Professor D'Ambrosia which have been of great help in achieving properly the various experiments presented in this thesis.

Many thanks to Daniele Pelessone and Xinwei Zhou from ES3 for providing MARS, their constant support and assistance.

I would also like to acknowledge Professor Giovanni Di Luzio for his help on the Full Coupling Between Diffusion and Mechanical Analysis in a Discrete Model project.

A special thank you to Minh Q Vo for his continuous help and support. I am looking forward to see the bun shops travel to Europe.

I would like to take this opportunity to thank my colleagues and friends in the department, especially M. Pathirage, R. Rezakhani, W. Li, J. Smith, B. Liang, L. Wan, K. Luo, F. Mete, E. Ramayar, H. Luan, Z. Pan and the whole Civil and Environmental Engineering (CEE) department.

The ASR research was conducted under funds provided by the Nuclear Regulatory Commission (NRC). The UHPC simulations were performed with funds provided by the Engineer Research and Development Center (ERDC). These financial supports are gratefully acknowledged.

Last but not least, my gratitude goes to my mother Naima Bousikhane and my father Mostafa Bousikhane who supported me throughout this journey at any imaginable levels. Finally, I thank my older sister Itabe Bousikhane and brother Anouar Bousikhane who always looked out for me like nobody could.

Table of Contents

List of Tables

List of Figures

CHAPTER 1

Introduction

Concrete is undeniably the most widely used material in the construction field worldwide. Some of the reasons contributing to the unanimous popularity of concrete are its durability, strength, low maintenance, versatility, thermal resistance and affordability. However, concrete is composed of a complex heterogeneous internal structure, which includes several characteristic lengths from the scale of cement nanoparticles to the macroscale. This leads to mechanical properties that evolve during its lifetime due to different phenomena such as hydration, creep, shrinkage, drying and deterioration mechanisms such as alkali-silica-reaction, ettringite formation, freeze-thaw, carbonation, just to name a few. Due to this inherent complexity, detailed computational models must be developed to simulate accurately concrete behavior and its evolution in time.

The research conducted in this study focuses on the following objectives:

1) To investigate experimentally ASR effects on concrete mechanical properties evolution through destructive and non-destructive testing (Chapter 2). ASR has been a topic of study for many years by many researchers. In spite of that, experimental results available in the literature lead to divergent conclusions. This experimental program includes tests in compression, tension (fracture and Brazilian test) along with creep, shrinkage, self-desiccation and expansion measurements under various environmental conditions to clarify some of the unanswered questions concerning ASR consequences on concrete. Further qualitative investigations involving Los Alamos test, non-polarized, and polarized

light petrographic observations were performed. This portion of the thesis aims to provide readers with a comprehensive experimental study of ASR effects on concrete mechanical properties and their evolution in time. The long term deterioration assessments associated with such a mechanism can only be captured via the development of a model capable of simulating and combining precisely the main influential chemical/physical mechanisms involved in concrete strength evolution (i.e. aging, ASR, creep, shrinkage, thermal effect). The M-LDPM was developed along these lines and showed superior capability in not only modeling the damages associated to ASR but also predicting strength reduction which, to our knowledge, yet has to be accomplished in the literature (Chapter 3).

2) To explore the effect of cracking and a self-healing admixture (Penetron) on concrete permeability under a controlled drying environment. This chapter explores deterioration mitigation through a comprehensive experimental program which studies the to self-healing capacity of commercial admixture to counteract crack effects on concrete permeability. The tested specimens consist in regular, cracked and self healing C-Shaped beams, first designed and studied by Bažant et al. [**6**], drying in a controlled environment with a periodic monitoring of their relative weight loss. This information is further used to quantify the effect of cracks and self healing on concrete permeability. Along these lines, Chapter 4 also includes the formulation and implementation of a three dimensional numerical model based on the M-LDPM framework to study and model damaged concrete permeability behavior. The calibration and validation of the LDPM is performed by modeling the results of water penetration into cracked reinforced concrete provided by Zhang and coworkers [**81**].

3) Finally, the prevention and mitigation aspects of concrete deterioration are studied via

the modeling of fiber size and shape effects on the quasi-static and dynamic testings of UHPC mechanical response. The considered set of fibers involves ZP305, Nycon type V, OL 10 mm and OL 6 mm fibers. The relevant experimental results provided by the U.S. Army Engineer Research and Development Center (ERDC) included quasi-static as well as dynamic testings. The considered quasi static tests contained uniaxial compression tests, Direct Tension Test (DTT) in the cases or randomly distributed and oriented fibers and 4 point bending tests. The dynamic tests consisted in penetration and perforation tests of UHPC fiber reinforced panels of various thicknesses. The LDPM-F was successfully calibrated and validated based on the provided experimental data providing results once again in excellent agreement with the experimental data.

CHAPTER 2

Experimental Investigation of Alkali-Silica Reaction Effects on Aging Concrete Mechanical Properties

2.1. Introduction

Concrete is the most common material in the construction of civil engineering structures such as bridges, high rise buildings, or even Nuclear Power Plants (NPP). In new constructions concrete structures' durability can be extended using, for instance, self-healing agents that will over time increase concrete strength and reduce the risk of failure of modern UHPC. However in already built structures, deterioration mechanisms exist and can significantly reduce the lifetime of concrete structures. Some examples of degradation mechanisms are corrosion, ASR, freeze and thaw, delayed ettringite and several others.

Concrete is one of the most challenging materials to study and it isknown to have a complex internal structure, which includes several characteristic lengths from the scale of cement nano-particles to the macro-scale. Moreover, numerous chemical reactions happen in parallel within concrete, further increasing the difficulty in defining accurately the range of action of a given chemical reaction. Over the past few years, researchers have tried to understand these degradation mechanism phenomena such as Alkali-Silica Reaction in an effort to predict their effect precisely with the objective extend structural durability.

The interest in accurately decoding these degradation mechanisms is two fold: safety and money. Indeed, it is necessary to understand the underlying mechanisms behind a given deterioration mechanism to predict the damages associated with it to avoid unexpected structural failure. This is important from a cost standpoint as well as for public safety. This chapter of the dissertation adopts an experimental approach to determine ASR effects on concrete mechanical properties.

Alkali Silica Reaction (ASR) is a chemical reaction discovered in the nineties by Stanton et al. [**68**], where an expansive gel forms. This gel is the product of the chemical reaction between alkalies contained in cement, crystalline silica from siliceous aggregates and water. Deschenes et al. [**7**] identified two stages of ASR evolution in concrete which are now commonly accepted by the scientific community. During the first stage of the reaction a gel is formed by the dissolution of the crystalline silica. And in the second stage, the ASR gel absorbs water and swells at the same time, which generates high pressures that typically result in concrete deterioration. At early stages of ASR in concrete, micro-cracks usually begin to develop, while at more advanced stages of the gel formation, macro-cracks become visible. Sanchez et al. [**63**] studied the ASR mechanisms and identified three of such types: a) peripheral reaction rim, b) pockets of gel and finally c) gel veins being formed within the aggregate itself. The failure mode and ASR mechanism associated with a given concrete is known to depend on the silica distribution within the reactive aggregate but also the aggregate's geometry as demonstrated by Akira Otsuki et al. [**54**].

ASR has been studied extensively over the past 50 years to identify the minimum requirements for the reaction to initiate. The parameters that were identified as influentials are the silica, alkali and moisture contents, temperature, aggregate size and shape, concrete internal structure, and stress distribution. Chatterji et al. [**15**] and Mirza et al. [**32**] determined that ASR was only probable in moist environments exceeding 85 % relative humidity. That is the reason why, numerous bridges in high relative humidity environments have severely suffered from ASR damaged. Past studies performed by Jones [**38**] and Larive [**43**]demonstrated that temperature also acts as a catalyst of the ASR taking place in concrete. However, it is important to note that when concrete is cured at high temperatures, it experiences a so-called thermal expansion different from the expansion due to ASR. This is another example of reactions happening in parallel in concrete.

The reason why ASR studies have become so popular over the last few years is because it jeopardizes directly the lifetime of concrete structures by affecting concrete mechanical properties. Two types of tests are currently available to evaluate ASR impact on concrete performances: non-destructive (NDT) and destructive testing methods. Non-destructive evaluation has achieved an important role in the quality control of concrete structures with regards to their strength and durability. Kursat et al. [**72**] and Akash et al. [**36**] used the "rebound hammer" and "windsor probe" which are the most widely used NDT methods to evaluate concrete strength. Larive [**43**], Monette et al. [**50**], Multon [**51**], Ben Haha [**11**] and Esposito [**27**] have conducted studies on ASR effects on concrete mechanical properties involving the direct determination of concrete strengths through destructive

testing. The scientific community agree on the idea that ASR affects mechanical properties negatively and hence decreases concrete strength.

This chapter 2 confers the reader with experimental findings of ASR effects on aging concrete mechanical properties evolution. First, the experimental protocols including the mix design and samples preparations are explained. Secondly, the non-destructive evaluations of ASR are presented conferring the reader with qualitative observations of how can ASR gel and damages can be identified. Then, the destructive evaluation of ASR affected concrete samples is presented, providing valuable quantitative observations on compressive and tensile properties as well as long term induced deformations (creep).

2.1.1. Mix Design, Test Setups and Environmental Conditions

Mix design and samples preparation To characterize ASR damages on concrete properties, this paper adopts an experimental approach where mechanical testing is performed to characterize concrete mechanical properties evolution. A total of 436 samples were prepared with the mix design recommended in the ASTM C1293 [**35**] standard relevant to the accelerated concrete prism test given in figure 9. However, two types of aggregate were considered : One reactive (Spratt) and one non-reactive (Lafarge Fox River). The curing of the concrete samples was achieved in curing rooms at 23^{o}C and 100 RH. The second batch corresponding to the non reactive samples or samples of reference were tested in compression to ensure that observed differences in terms of mechanical properties will be due to ASR and not to the aggregate properties. To certify this conformity,

6 samples were prepared and cured for 14 days then tested in compression on day 15. Aggregate choice: Spratt and Lafarge Fox River Spratt is a well known aggregate because of its sensitivity to ASR, this can be explained by the fact that it contains about 9% of silica per unit volume. NR38 and NR50 respectively designate the non-reactive samples (cast with Lafarge Fox River aggregates) cured at 38^oC and 50^oC. Similarly RX38 and RX50 correspond to the reactive samples (cast with Spratt aggregates) cured at 38^oC and 50^oC.

Table 2.1. Sieve Curve for Concrete prism experiments.

Sieve size		
Passing %	Retained %	Mass
19 mm	12.5 mm	33 %
12.5 mm	9.5 mm	33 %
9.5 mm	4.5 mm	33 %

		Reactive Concrete	Non Reactive Concrete
Materials	Extra Information	Quantity [kg/m^3]	Quantity [kg/m^3]]
Portland Cement	Holcim St. Genevieve Type 1	420.04	420.04
Coarse Aggregate	Spratt Coarse	1078.58	-
Coarse Aggregate	Lafarge Fox River	-	1078.58
Sodium Hydroxide	Lab Stock	4.15	4.15
Fine Aggregate	Hanson Plum Run Peebles, OH	718.46	718.46
Water	Potable	176.2	176.2
Water/Cement		0.42	0.42
Superplasticizer	BASF Glenium 7500	3.2	3.2

Table 2.2. Mix design summary (in accordance with ASTM 192).

Companion batch validation Table 4 presents the compressive strength of two concretes casted at the same time and cured for 14 days at 25 Celsius Degrees and a 100

% relative humidity (RH). One was prepared as a reference for the reactive batch using spratt which is known for having high silica content (more than 10% by weight). On the other hand, Lafarge Fox River was used for the companion batch. According to 2.3, the strengths at 14 days are equal (less than 0.4% difference). This observation leads to the conclusion that Lafarge Fox River is a good candidate to cast the batch of reference for the accelerated standard prism tests. Hence, any mechanical characteristic variation and difference between the two batches will not be associated to the type of aggregate. Also various geometries and ages of testing were considered depending on the test and are presented in Table 3.1.

Table 2.3. Companion batch validation table comparing strength of concrete prepared with Lafarge Fox River or Spratt at early ages

	# Samples Tested	Age of Testing [days]	Average f'_c [MPa]
Spratt Batch	3	3/15/28	39.57/55.67/61.32
Lafarge Fox River Batch	3	3/15/28	39.71/54.56/60.89

Table 2.4. Geometries and ages of Testing

	Dimensions [mm^3]	Testing ages [days]
Compression	75x75x75	60/120/365
3-point bending	75x75x250	60/90/120/240/300/365
Brazilian	r=100mm h=200mm	60/120/365
Creep	75x75x75	365
Expansion	75x75x250	400
Shrinkage	75x75x250	365

Environmental conditions After casting, the concrete samples were demolded after 24 hours and kept at 100%RH/23°C for 28 days. At this point, half of the reactive and non reactive samples are moved to the environmental chamber set at 100%RH/38°C while the

other half was placed in the second environmental chamber set at 100%RH/38°C. Saturated conditions and higher curing temperatures are selected to accelerate ASR according to ASTM C1293. In the surrounding of this project funded by the Nuclear Regulatory Commission, considering higher temperature was one way to also replicate concrete environmental conditions in nuclear power plants and provide relevant conclusions.

Experimental tests performed

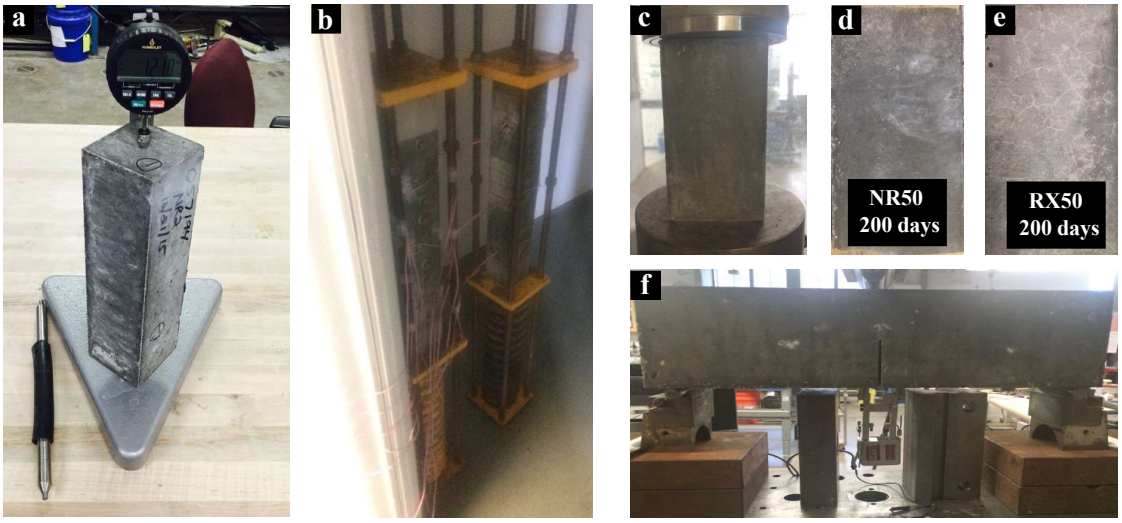

Figure 2.1. Test set ups for a) Longitudinal expansion measurements, b) Creep test, c) Compression test. Damages observed in d) Non-Reactive and e) Reactive concrete samples at age 200 days. f) 3 point bending test set up.

Free expansion measurements were performed 76.2x76.2x285 mm^3 concrete prisms to determine the potential ASR expansion of cement-aggregate combinations over time. According to ASTM C1293 and C490, the free expansion measurements were taken on using a Humboldt length comparator for 400 days as depicted on Figure 2.6a. It is worth mentioning that according to the American standards, an aggregate is considered potentially deleteriously reactive if the measured free expansion in the longitudinal direction exceeds

0.04% after one year. The latter is currently the preferred method of assessment although one its significant drawbacks is the important time duration of the test.

The petrographic and polarized light microscope observations were performed at CTL-group laboratories on 76.2 x 76.2 x 152.4 mm^3 grounded concrete sample cross sections according to ASTMC295. The purpose of this test is to evaluate possible aggregate reactivity through petrographic examinations. Polarized and non polarized light stereo microscopes were used to appreciate visually and microscopically examine the produced ASR gel in the studied concrete samples.

A semi-adiabatic calorimeter was used to characterize the hydration degree of three different concrete samples. Indeed, one important parameter in concrete strength evolution is hydration, a reaction where the cement molecules react with water leading to concrete strengthening. This reaction between water and cement translates in a temperature rise that is measured by placing a thermocouple at the center of the 50.8 mm x 101.6 mm (diameter x length) concrete sample for optimal accuracy in the measurements. The temperature was monitored for 4 days every minute starting from the moment when the water was poured into the dry mix.

It is worth mentioning that the destructive testing of concrete samples was done using MTS load frames with capacities of 90 kN, 1000 kN and 4500 kN. To reduce friction at

the joint between the loading steel plates and the concrete samples, hyaluronic acid is sprayed on the concrete surfaces.

Concrete compressive strength is a fundamental physical property constantly used for design calculations of concrete structures. Performing such test is crucial to estimate concrete strength and ASR impacts on it. The later was performed on 76.2 x 76.2 x 152.4 mm^3 concrete samples at the age of 60, 120 and 360 days. The set up used is presented in Figure 2.6c

Three point bending tests were performed on notched concrete samples at the ages of 60, 90, 120, 240, 300 and 365 days and constitute an important part of this experimental campaign as no data on fracture energy evolution in presence of ASR is currently available in the literature. This experimental campaign aims at understanding how can ASR alter fracture energy properties of concrete. The set up used for the three point bending test in presented in Figure 2.6f.

Concrete tensile strength is one its main weaknesses and typically constitutes 8% to 14% of the compressive strength according to Hanson [**34**]. The tensile strength of the considered material was evaluated through Brazilian tests.

When concrete is loaded, the generated deformations can be categorized into two induced

deformation: The elastic deformation that occurs immediately and the long term deformation which similarly to the elastic deformation occurs as soon as the concrete samples are loaded. However, the later deformation is time dependent and continues at a decreasing rate: Creep. Multiple factors can affect concrete creep behavior starting from the concrete strength, magnitude of the applied stress, the age of loading or even hygral and thermal environmental conditions. The main motivation for performing such a test in addition to the previously presented tests is to study ASR evolution when uniaxially confined. The experimental set up used is shown in Figure 2.6b. In the field, concrete structures are constantly subjected to stresses which can impair ASR progress. Experimentally investigating such an issue is here aimed through creep testing under optimal conditions for ASR development.

2.2. Non Destructive Evaluation

2.2.1. Petrography

Petrographic test method

A total of 8 prims of 76.2 x 76.2 x 152.4 mm^3 were prepared according to the described procedures in ASTM C856-14 Standard [**4**] relevant to Petrographic Examination of Hardened Concrete. This time, only reactive samples (containing Spratt) were considered for this study. CTL Group petrographer Victoria Jennings provided a considerable help in the samples preparation and study. The casting process follows the ASTM C1293 [**14**] relevant to the accelerated concrete prism test.

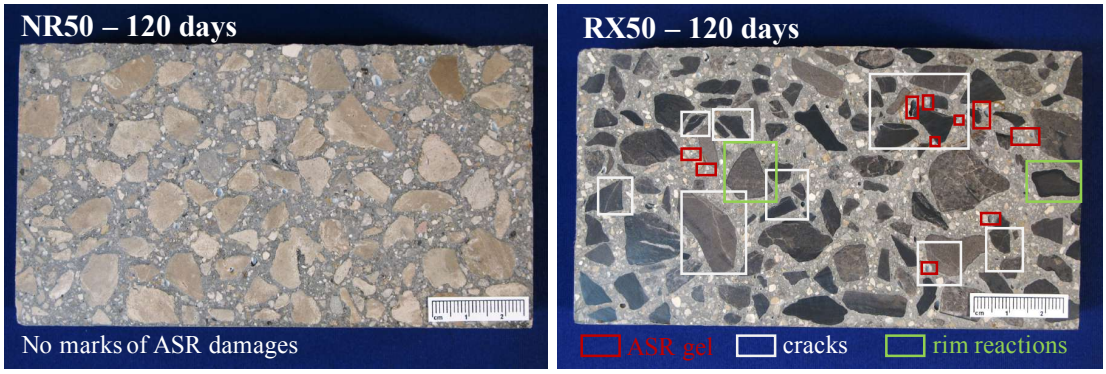

Figure 2.2. NR and RX concrete samples cured for 120 days at 50°C/100%RH cross section observations at the stereomicroscope

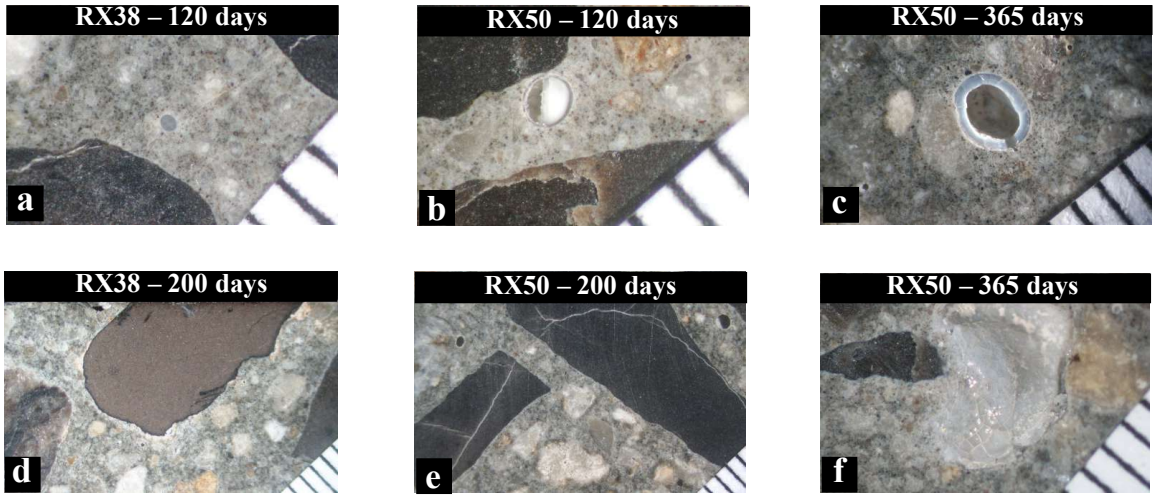

Figure 2.3. Samples in different environmental conditions at 100%RH (a) day 120/38°C; (b)day 210/50°C; (c) day 365/50°C; (d) day 200/38°C; (e) day 200/50°C and day 365/50°C

The samples are cut with the diamond saw along their middle longitudinal axis from side to side in order to allow a better identification of potential ASR gel. After cutting, half of the sample is lapped in three steps on the grinding wheel (Crystal Master Pro 12), whereby one can find three succinct grinding level with the Grid-Abrade diamond

grinding discs: 60 microns, 30 microns and 12 microns. After each step of grinding, to obtain suitable samples alcohol is sprayed on the lapped surface before processing to drying.

Once ready, the samples are examined with the stereo-microscope.

Petrography results and discussion

The results obtained with the stereo-microscope at this stage of the reaction are reported in Figures 2.2 and 2.3 show visual evidences of ASR gel and damages for the studied concrete.

Figure 2.2 shows what can be observed by naked eye for non reactive and reactive samples stored at 50°C/100%RH for 120 days. At day 120, the structure of the non reactive sample remains intact whereas the reactive ones display clear evidence of damages. For the reactive sample presented in the right Figure 2.2, a considerable mapping of cracks is present most likely due to ASR although this assumption will be confirmed further in paper. Potential ASR cracks, gel formation zones and rim reactions are marked on Figure 2.2 and supports the idea that at day 120, the non reactive samples do not display damages from thermal shocks, ASR or other damaging mechanism as their structure remains intact unlike the set of reactive samples. The only difference between the two batches is the type of aggregate used which consolidate the hypothesis that ASR is the sources of the visible damages. These observations are consistent with the results given from the mechanical tests results in the section discussed further in the paper and the non reactive sample show strengthening while the reactive samples present strength loss. As a result, the preliminary conclusion is that presence Spratt does impact the ASR taking place in concrete.

The photographies shown in Figure 2.3 present x40 magnified observations performed with a stereo-microscope on reactive concrete sections , age of 120, 200 and 365 for samples stored at 100%RH 38°C and 50°C. At 120 days, one can notice on Figure 2.3a and 2.3b small ASR pockets of gel forming in the cement paste and the formation of microcracks potentially due to ASR. The presence of microcracks is the signature of stresses release due to high internal pressures. Also, one potential pocket of ASR gel is found in the reactive samples at day 120 as shown in Figure 2.3b. The chemical testing of those pockets filled with amorphous gel was also performed using the Los Alamos to identify the gel nature and will be introduced in Section 2.2.2. At later ages, one can clearly notice the massive presence of ASR gel, especially for the older concrete samples. Starting from 200 days, one can clearly observe rim reactions as depicted on Figure 2.3d for instance where the gel has the wet aspect and texture on the outer surfaces. Rim reactions have been previously identified and studied by Kunpeng Zheng et al. [**83**] in concrete or even by Mladenovic et al. [**49**] in mortar. The gel present in the samples of age 200 and 365 on Figures 2.3c and 2.3f shows a different structure from the gel at 120 days as cracks within the gel itself are visible. Similarly to the samples observed at age 120, the concrete samples at age 200 and 365 present larger cracks which suggest that ASR has been ongoing beyond 120 days and damaging the concrete internal structure even more. Also, these observations as expected are consistent with the idea that ASR was successfully activated in the reactive samples only by using Spratt aggregates instead of Lafarge Fox River. Last but not least, this initial qualitative study confirms and indicates that the presence of ASR leads to a significant alteration of the concrete structure. In the case of accelerated reactive prisms

tests, one can by naked eye appreciate the damages caused by ASR which translate into a crack mapping cutting through the cement paste, aggregates and ASR gel itself.

2.2.2. Petrographic polarized light microscope study of concrete thin sections.

Petrographic polarized light microscope observations test method The experimental protocol followed to prepare the thin sections consists in using concrete lapped surfaces and to set a layer of transparent epoxy on the targeted surface. A transparent epoxy was been selected for its optical properties that are known for not altering light polarization. The polarized light microscope allows for plane or cross polarized light observations. With plane polarized light, after the light beams interacts with the material, its polarization gets altered by birefringence. With cross polarized, the light with perpendicular orientation only is transmitted. The latter phenomena translates in a contrasts increase of the numerous concrete constituents while with plane polarized light contrasts are enhanced which emphasizes the visual aspect of cracks.

For the subsequent discussion, both results will be presented as they will provide complementary information.

Petrographic polarized light microscope results and discussion

As presented in Figure 2.4, the deposits of ASR gel are found either in voids (paste or aggregates) or at the interface between the siliceous aggregates and the cement paste where the presence of silica, alkali and moisture are sufficient for ASR gel to form. Figure 2.4 shows a large air void of approximately 3 mm in concrete lined with ASR gel. In these pictures, the ASR gel can be recognized by its a transparent/translucent texture.

The Figure 2.4b and 2.4f corresponds to a zoom on the lower region of that same void shown in Figures 2.4a and 2.4e. On the cross polarized light picture one can notice small air bubbles in the epoxy used to mount thin-section block that are relics of sample preparation and insignificant. On the plane polarized light picture one can observe that the gel itself is cracked which is the sign that high stresses are present due to ASR but also that the gel was in a solid form prior to failure. This same study on gel in void was conducted on other voids and the comments that were previously made remain valid.

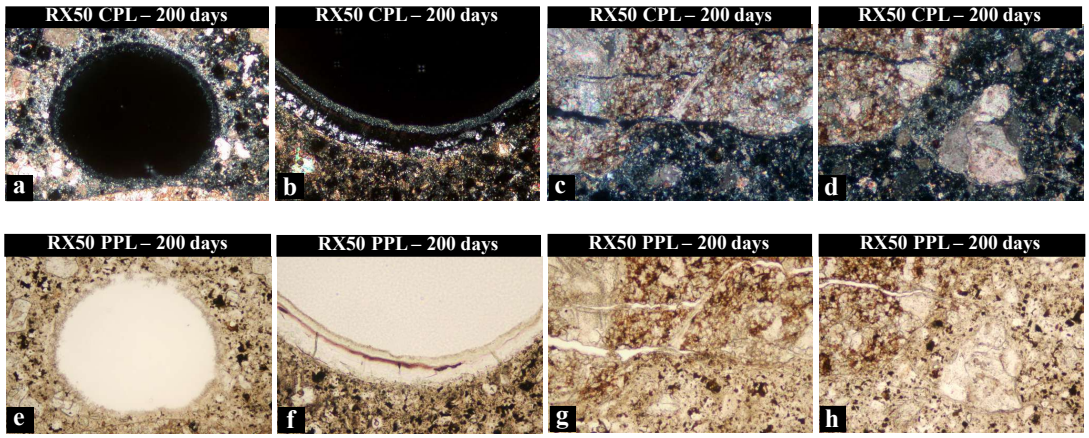

Figure 2.4. Crossed Polarized Light (CPL) observations of a) Air void in concrete lined with ASR gel b) Region of air void in concrete lined with ASR gel c) Microcrack branches along paste-aggregate interface and into paste lined with ASR gel and d) Further along paths of microcrack branches along paste-aggregate interface and into paste lined with ASR gel. Plane Polarized Light (PPL) observations of e) Air void in concrete lined with ASR gel f) Region of air void in concrete lined with ASR gel g) Microcrack branches along paste-aggregate interface and into paste lined with ASR gel and h) Further along paths of microcrack branches along paste-aggregate interface and into paste lined with ASR gel.

Last but not least, the photos display layered deposits of ASR gel, both amorphous (black in plane-polarized light) and locally crystalline (birefringent in cross-polarized light) which reinforces the idea that ASR gel is present in solid form in concrete voids.

The Figures 2.4c, 2.4d, 2.4g and 2.4h show a microcrack extending from aggregate (left) particle into paste (right). These microcrack are lined with ASR gel and splits into three branches within paste. Again, the presence of cracks suggests a history of high stresses most likely caused by ASR damages. Here, the texture of the gel does not suggest that layers have formed successively on top of one another. One can observe one and only clear layer of gel on the contrary of the multiple layers of gel that were found in voids. Furthermore, the gel in the cracks looks intact, only the aggregate and cement paste are cracked.

Figure 2.4c and 2.4g displays microcracks within the aggregate particle (top) with branches extending along the paste-aggregate interface and into paste (bottom). These microcracks are locally lined with ASR gel as well.

The Figure 2.4d and 2.4h shows the continuity further along paths to the right of that microcrack from previous photos shown in the Figure 2.4c and 2.4g. Again the microcracks are locally lined with ASR gel. Overall, ASR gel observed in concrete can be found in different forms and displays different textures. A basic petrographic analysis with the stereomicroscope would not have been enough to identify the different forms of gel created due to ASR in concrete.

Los Alamos test evaluation method As introduced in the introduction, concrete is a cementitious material controlled by complex time dependent chemical reactions. Because of its natural similarity with earth material, geoscientists developed a geochemical method

to identify gel reaction products associated with ASR [**31**].The experimental protocol given by Guthrie et al. [**23**] was meticulously followed for the ASR gel staining test. To confirm the validity of the test, both reactive and non-reactive sample were subjected to the ASR get staining test.

Fresh cylindrical 101 mm x 202 mm (diameter x length) concrete samples were tested in tension with the Brazilian test.to stain the untreated middle cross section. The choice of a freshly fractured sample can be justified by the purpose of applying the staining method on an internal cracked surface that has been subjected to the least amount of chemical change to the ASR gel.

The loose dusts accumulated during the sample fracturing are removed with distilled water (contaminants free). Sodium cobaltrinite is used to saturate a table spoon of water and then applied for 45 seconds on the concrete surface. At this stage, the potassium contained in the ASR gel reacts with the sodium cobaltrinite producing a shiny yellow staining that intensifies as the reaction evolves with time. The open structure of the ASR gel which facilitates cations exchanges with fluid (chemically charged water) is outlined using a chemical technique producing a shiny yellow staining of the ASR gel or more specifically the potassium contained in it. After rinsing the samples with pure water, Rhodamine B is used to saturate a table spoon of water and then applied for 45 seconds on the concrete surface. The dark pink second chemical has the specificity to stain any chemical compound but the potassium contrasting significantly areas where ASR gel is found and non reactive areas. As depicted on Figure 2.5b and 2.5d, some ASR gel appear to be stained in orange which suggests a poor potassium ASR gel where both used chemicals were partly capable of staining the ASR gel.

In this section, 76.2 x 76.2 x152.4 mm^3 taken from the reactive batch that had cured for 100 days at 50°C 100%RH were cut in half prior to being treated. One face was used for casual petrography as depicted on Figures 2.5a and 2.5c while the remaining half was subjected to the Los Alamos test presented in above. The results of the Los Alamos test are presented in Figures 2.5b and 2.5d. The results depicted in Figure 2.5b and 2.5c confirm the presence of ASR gel in the reactive samples. The potassium present in the ASR gel significantly reacts with the sodium cobaltrinite in the reactive samples while in the non reactive samples, potassium presence is too low to even leave the slightest trace of staining. Last but not least, the results show that the heterogeneous character associated with alkali silica chemical reactions can lead to an ASR gel production with different potassium concentrations.

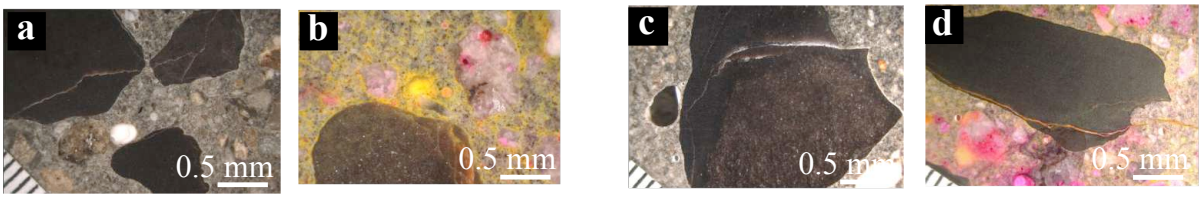

Figure 2.5. Air void in concrete lined with ASR gel.

2.2.3. Expansion ASTMC1293

Expansion test method The longitudinal expansion measurements were taken with a length comparator that has a resolution of 1μm. The comparator was calibrated using an invar reference bar for better accuracy of the periodical measurements. The expansions were picked up against the steel studs embedded during casting at the opposite ends of the concrete prisms. By subtracting the initial expansion reading to the one at a given age,

one can directly obtain the relative expansion. The initial measurement was taken at 28 days immediately after the initial curing process.

Expansion test results and discussion

The results obtained in this accelerated concrete prism tests are reported in Figures 2.6 through 2.7.

Figure 2.6 reports the measured expansions. The gray curve and the red curve are relevant to the non-reactive samples (NR) cured at 38°C and 50°C in the environmental chambers at 100% Relative Humidity (RH). These samples are considered here as reference values for the subsequent discussion as they don't suffer from ASR damages. The evolution of the mechanical properties for non-reactive samples overtime is mainly governed by aging. For these samples no appreciable expansion can be observed over a year. Finally, the black curve and blue curve represent the expansion measured for the reactive samples (RX) stored at 38°C and 50°C. As expected these samples do expand significantly, well beyond the ASTM C1293 [**35**] ASR susceptibility limit set at 0.04 %. The expansions of the reactive samples stored at 50°C pass this threshold wihtin the first 100 days of curing while it takes 150 days for the reactive samples stored at 38°C to go beyond this limit. At 365 days of age, the expansions obtained for the reactive samples at both temperature coincide, although the expansions for the reactive samples stored at 38°C keep increasing while for the reactive samples stored at 50°C the expansion flattens. This observation suggests that at higher temperature, ASR occurs faster but slows down at earlier age afterwards.

No significant evolution of ASR, and consequently no significant expansion and damages are observed for the non-reactive samples as despicted on Figures 2.6. The measured expansion in the case of non reactive samples corresponds principally to the thermal expansion. A preliminary petrographic analysis was performed using a stereomicrospcope to estimate the amount of ASR gel in reactive (RX) and non reactive (NR) concrete samples at the age of 200 days. As expected, the non-reactive samples were found to have no gel at all. On the other hand, the reactive samples showed clear evidences of ASR gel and the observed damages associated with ASR are visually clear. Figure 2.3 and 2.5 show evidences of ASR gel in air voids and cracks found in reactive concrete sample sections using a stereomicroscope. This study allows a qualitative appreciation of damages caused by ASR starting from age 120 days. As expected, more cracks are visible in more aged reactive samples as they have suffered from ASR for a longer period of time .

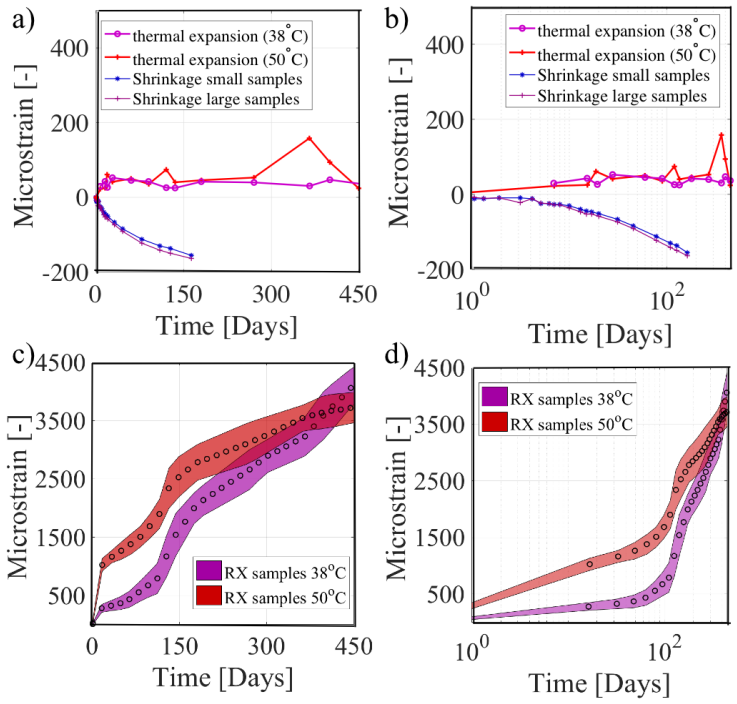

Figure 2.6. Shrinkage and thermal expansion experimental results in terms of microstrain a) Regular and b) Log time. Longitudinal expansion results in terms of microstrain versus c) Regular and d) Log time.

2.3. Destructive ASR affected Concrete Evaluation

2.3.1. Compression Tests

Compression test method The information given by the non reactive samples batch are valuable as for the later, all the usual chemical reactions taking place in concrete are still ongoing, aging is one them for example. The uniaxial confined compression tests were performed on 76.2 x 76.2.6 x 152.4 mm^3 concrete prisms at the ages of 60, 120 and 365 days. The tests were displacement control at a displacement rate of 0.003 mm/sec. To minimize temperature and relative humidity drop effects prior to testing the samples are

tested within the first 20 minutes following the moment at which the samples are taken out of the environmental chambers. The compressive strength is finally obtained by reading the maximum stress level during the test. Compression test results and discussion

The results for this test are introduced in this paper in terms of stress versus strain curves. The measured force was divided by the cross section of the sample to compute the stress level, while the strain was calculated by dividing the relative displacement of the loading plate by the sample length.

Figure 2.7 shows the experimental results of the compression tests performed on reactive concrete samples cured at 38°C and 50°C in terms of stress versus strain. Before even taking a look at the compressive strength one the reactive batch for different ages, one can observe how much ASR affects the young's modulus as depicted on Figures 2.7a and 2.7b. An average decrease of 8.8% of the elastic modulus was measured within the first year of the accelerated test which cannot be ignored when designing concrete structures in environments where there is potentiality of ASR. As far as the compressive strength is concerned, at the ages of 60, 120 and 365 days, the samples cured at lower temperature present respectively a decrease in compressive strength of 12%, 17% and 23%. The losses were calculated based on the strength of the reference batch under the exact same conditions (RH, temperature, age) and provide the reader with the actual loss in strength which also includes the aging component as described for the non-reactive samples. In a word, ASR causes concrete compressive strength to decrease up to 23% after one year at 38°

2.3.2. Three Point Bending Tests

Three Point Bending test method The 76.2 x 76.2 x 285 mm^3 concrete beams were notched by the mean of a diamond saw at the mid span up to 38 mm ($D/2$). The test was performed using a 6 mm travel length extensometer placed on the notched to insure Crack Mouth Opening Displacement (CMOD) control under a 0.003 mm/s displacement rate. The load displacement at mid span curve is used to compute the work of fracture $W_F = \int_0^{\overline{u}} P(u)du$ which is used to calculate fracture energy G_F:

$$G_F = \frac{\int_0^{\overline{u}} P(u)du}{b(D - a_0)} \tag{2.1}$$

where $b(D - a_0)$ represents the initial ligament cross section above the notch, $b = 76.2$ mm and $D = 76.2$ mm are respectively the thickness and width of the specimens. Three Point Bending test results and discussion

On Figures2.7c and 2.7f, one can see the fracture energy of non-reactive samples increasing over time for both temperatures due to aging. As some of the experimental data displayed had the end of the tail (softening part of the load versus CMOD results), the fracture energies were calculated with $\overline{u}$=0.4 mm to allow for a comparison between all the samples. This method is valid as the samples have all the same geometry and are size effect independent. On Figure 2.7c and 2.7f the reactive samples cured at 100% relative humidity, 38°C and 50°C show a significant decrease in terms of fracture energy. This loss is mostly due to ASR counteracting aging as described in previous reports. The reactive samples are subjected to ASR but also aging, however the experimental results show dominance of ASR damages. The effect of ASR damages on the fracture energy of

concrete can be calculated by subtracting the fracture energy of reactive samples to the fracture energy of non-reactive samples at same age and under the same environmental conditions. According to Figure2.7f, the reactive samples stored at 50°C show a slightly more important loss in terms of fracture energy than the reactive samples at 38 °C. The experimental results confirm the hypothesis that temperature accelerates the ASR and subsequently the damages that it causes in concrete.

2.3.3. Brazilian Tests

Brazilian test method . The prepared samples were 101.6 mm x 203.2 mm (diameter x length) cylindrically shaped to easily load per unit length the concrete specimens. The tests were performed at the ages of 60, 120 and 365 under displacement control at a rate of 0.003 mm/s.

Brazilian test results and discussion Figure 2.7 presents the obtained results of tensile splitting strength and compressive strength in terms of stress (MPa) versus age (in days). The differences among the various environmental conditions confirm the analysis discussed above in relation to the fracture energy. However, according to Figures 2.7b and 2.7d, it is important to emphasize that ASR damages are more appreciable when tensile properties are solicited than in compression. This can be explained by the fact that ASR gel has been found in solid form in the petrographic observations which would suggest that it could display some form of stiffness leading to less damages in compression.

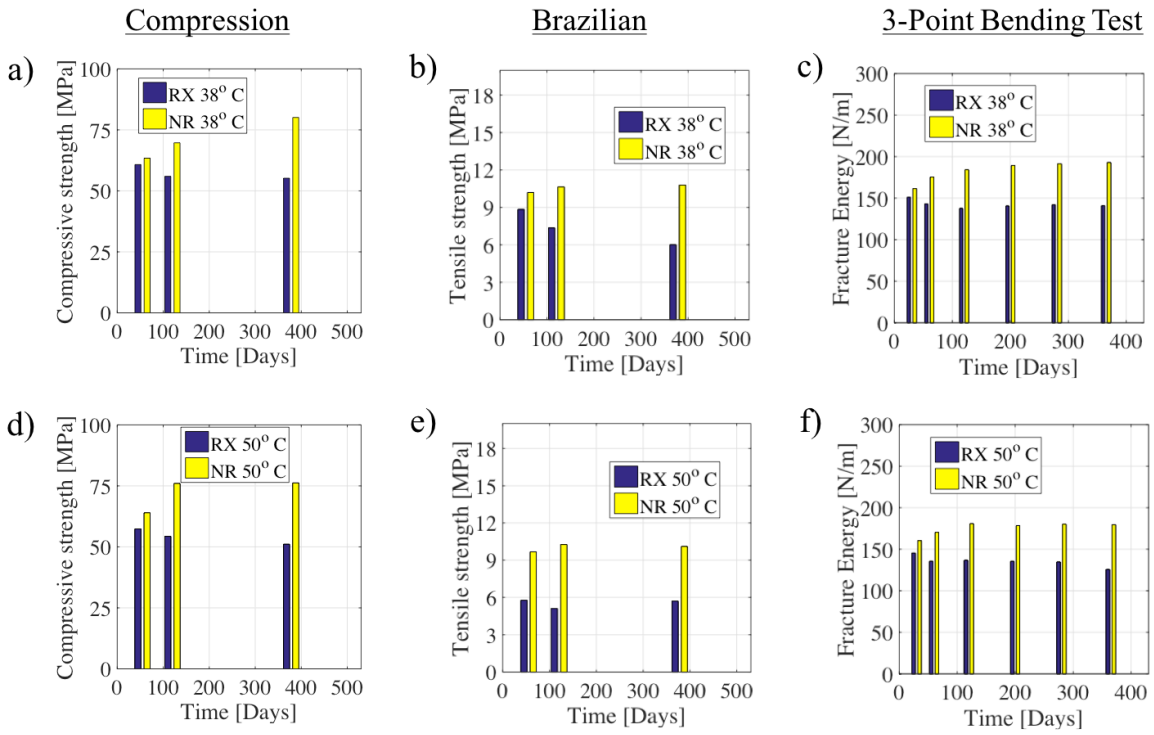

Figure 2.7. Results of uniaxial compression test for a) Non-reactive and d) Reactive samples, Brazilian test for b) Non-reactive and e) Reactive samples, and 3 point bending test in terms of fracture energy for c) Non-reactive and f) Reactive samples.

2.3.4. Creep Tests

Creep test method The creep test measures the load induced time dependent compressive strain under given controlled environment conditions. The creep test that were conducted during this experimental campaign included not only basic and drying creep but also creep at 100% RH, 38°C and 50°C. Creep is known to be proportional to the applied stress as long as the latter does not exceed 40 % of f'_c. The considered samples for this test were 76 mm x 76 mm x 150 mm concrete prisms subjected to $0.4f'_c$ (23.2 MPa). Each creep frame was used to load 3 samples stacked on top of one another. The loading frames have a

capacity to apply and sustain loads 10 times greater than the applied load which appears to be convenient to avoid additional deformations. The frames depicted on Figure 2.6 b consist in high strength square plates mounted in series on steel threaded roads. Nuts are used to constrain the vertical displacement of the plates and sustain the load on the samples while the lower part of the frame is armed of a large spring that serves as a load maintaining element. Spherical heads were placed at the ends between the steel blocks and the plates to insure uniform loading of the specimens and enhance the stiffness of the overall system.

The outer surfaces of each samples were grounded where the pins and strain gages were placed.

The pins were made of steel and attached to the concrete samples in the longitudinal direction to measurement the vertical deformation. High strength and temperature resistance epoxy was used to fix the pins. The distance between each pin was fixed to 101.6 mm by means of an anodized aluminum alloy instrument frame.

The multi-length strain gauge set was used to read the strain measurements of each sample. The ages of measurements were the following 0 and 9 minutes, 1 hour, 1, 7, 14, 28, 60, 100, 150, 200, and 280 days which correspond to the days of loading given by ASTM C512. However, considering the environmental conditions which include higher temperatures and saturated humidity conditions, the applied load had to be checked at least twice between each strain measurements to account for a faster creep due to the higher curing temperatures.

Creep test results and discussion

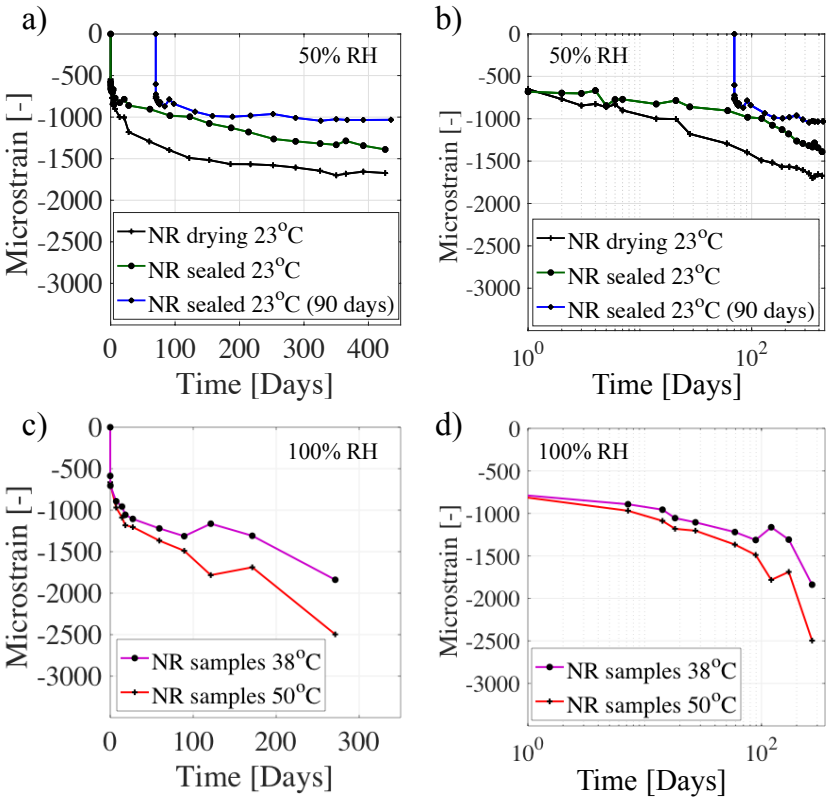

Figure 2.8. Results of uniaxial compression test for a) Non-reactive and b) Reactive samples

Figure 2.8 presents the creep test results in terms of microstrains versus time or log time for non reactive concrete samples under the environmental conditions discussed above. The measured concrete samples deformations for autogeneous creep are smaller than for drying creep as the later includes the effect of drying shrinkage similarly to what Bažant et al. [**86**] have demonstrated (Picket effect). In saturated conditions (100% RH) and higher temperatures, respectively 38°C and 50°C, around 35 and 40% more creep was measured exclusively due to thermal effect. Previous studies conducted by Bažant et al.[**86**] have confirmed that higher temperatures are associated with larger deformations

under load which also explains why the samples stored at 50°C present more creep than the concrete prisms stored at 38°C.

Figure 2.9 presents the creep test results in terms of microstrains versus time or log time for reactive concrete samples. The results suggest that ASR has no noticeable effect on concrete deformation in the direction of loading. It was observed in the case of free expansion that significant longitudinal deformations were measured mostly due cracking. This assumption can be supported by the fact that under load, horizontal cracking cannot occur due to the confinement which counters cracks formation. As a results the longitudinal deformation corresponds to the expansion due to the ASR gel formation added to the usual concrete creep.

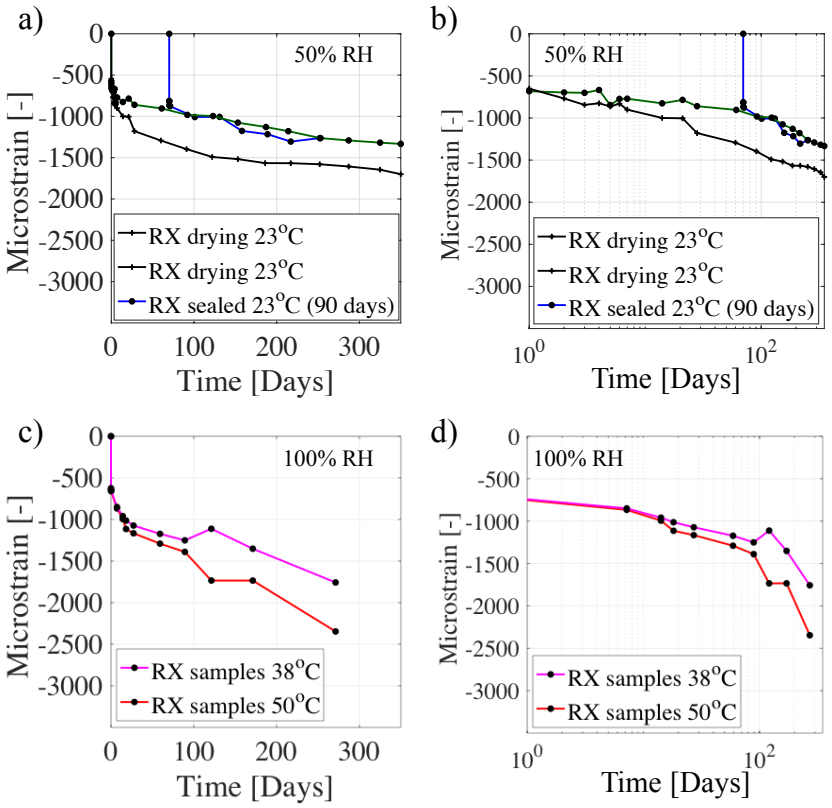

Figure 2.9. Results of uniaxial compression test for a) Non-reactive and b) Reactive samples.

The measured creep for reactive and non reactive samples in all environmental conditions suggest that under confinement, the longitudinal expansion which corresponds to the ASR gel formation is negligible. However, Figure 2.10 presents the measured lateral deformation in terms of microstrains versus time for a) non reactive and b) reactive concrete samples and suggests that concrete samples undergoing ASR expand more laterally. Last but not least this lateral expansion is about 16% more important at 50°C than at 38°C. The later observation comes from the fact that the axial confinement prevents the vertical cracks formation. Also, the measured ASR expansion mainly comes from cracking

and will naturally occur in the stress free direction which in this situation corresponds to the horizontal directions (lateral expansions).

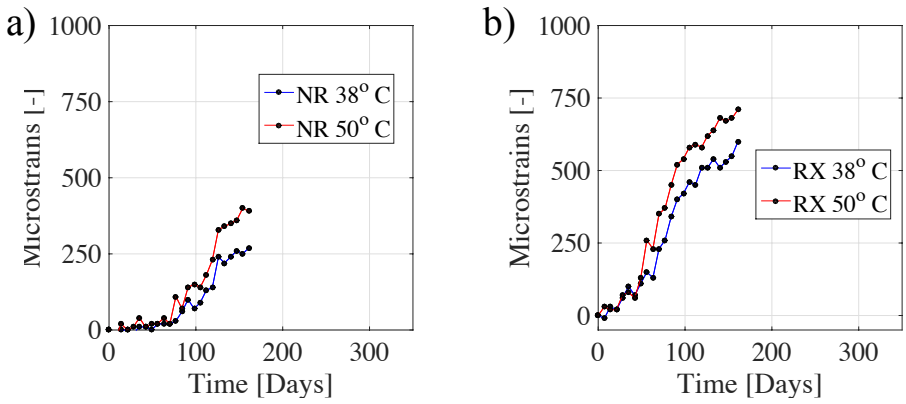

Figure 2.10. Results of creep lateral expansion a) Non-reactive and b) Reactive samples.

2.4. Concluding remarks

One can observe that the samples stored at 50°C present more expansion at early age than the ones stored at 38°C although they reach a lower asymptotic expansion at later ages. For the uniaxial compression test, the losses observed in terms of compressive strength are twice as small as the losses observed in terms of tensile strength which leads to the conclusion that ASR damages affect concrete tensile properties more than its performance in compression. The consideration of a companion batch is essential to fully characterize the strength loss due to ASR. The experimental creep test demonstrated that ASR expansion typically occurs in the stress free directions. The ASR gel formation represents a negligible portion of the measured expansions leading to the conclusion that what researchers have been measuring is mostly damage (cracking) due to ASR induced high internal pressures. From a qualitative perspective, the petrographic observations confirm

that at early age, less ASR gel and cracking can be found in the concrete samples. At later ages, clear cracking is visible and the amount of gel present in the reactive sample increases with time. The polarized light microscope observations lead to the conclusion that ASR gel can be found in the cracks although no clear evidences of gel flow were noticeable. Last but not least, the Los Alamos test confirmed that the gel observed in the concrete samples was actual ASR gel because of its chemical composition that is high in potassium ions (K^+).

CHAPTER 3

Modeling of Alkali-Silica Reaction Effects on Aging Concrete Mechanical Properties

3.1. Introduction

ASR is a slow degradation process that progresses at multiple scales capable of reducing a concrete structure's strength and lifetime over the years. Two principal steps are differentiated during ASR consisting of the ASR gel 1) Formation and 2) Swelling through water absorption. The ASR gel swelling is typically the source of high pressures generated internally which are naturally released through local cracking. The accumulation of damages results in quantifiable concrete macro-scale strength loss which supports the idea that ASR is a multiscale phenomenon. The Lattice Discrete Particle Model (LDPM), recently developed by Cusatis et al. [**20, 19**] is a meso-scale model which simulates concrete at the scale of coarse aggregate pieces. LDPM has successfully captured concrete fracture and failure in multiple types of experiments and has been extended to model ASR effect [**2, 21, 16**], fiber reinforced concrete [**65**], fracture and failure of concrete in a multi-scale framework [**22, 61**], and simulating rock mechanics under different loading conditions [**26**].

Computational models have been developed for years attempting to simulate ASR evolution and associated strength degradation in structures at the macro- and micro-scale levels. Early phenomenological modeling approaches simulated ASR at the macro-scale

level by establishing ASR expansion at the concrete level [**29**] and [**47**]. The first thermo-chemo-mechanical ASR model considering explicitly stress state effects was proposed by Saouma et al. [**64**]. Additional phenomenons such as shrinkage [**33**] and compressive strains have been included in Multon formulation [**52**]. Later on, more advanced and complex damage models including hygral effects coupled with thermo-chemical models were formulated by Pesaento et al. [**55**] and [**28**]. The first mathematical models based on fracture mechanics were introduced by Bažant et al. [**1**] in 2000 simulating ASR within a Representative Volume Element (RVE) at the aggregate level.

Some of the introduced models were capable of modeling ASR expansions and even sometimes the strength degradation associated with it, however, none succeeded in achieving realistic crack distribution and pattern with comparison to what has experimentally been observed. In 2013, Alnaggar et al. [**17**] proposed the ASR-LDPM, a three dimensional model simulating ASR effects at the aggregate level. Unprecedentedly, the later showed superior proficiency in simulating ASR expansion through two sub-mechanisms : the gel swelling and induced cracking. The results were further improved by coupling ASR with shrinkage and creep in [**3**]. Last but not least, Pathirage et al. [**57**] introduced the aging component of concrete coupled with ASR leading to the parallel modeling of concrete strengthening from the hydration products and ASR which deteriorates concrete mechanical properties.

As described above, concrete strength at a given age is the result of coupled deteriorating and strengthening mechanisms such as ASR, aging, creep and shrinkage happening in parallel, naturally contributing to the complexity of the problem. At this point, a comprehensive model is required to achieve a representative and efficient modeling of the

concrete mechanical properties evolution and failure modes over time. This chapter 4 adopts a multi-physics modeling approach of the experimental results introduced in chapter 2 via the direct coupling of ASR with aging, creep and shrinkage within the LDPM framework.

In the current research, LDPM is calibrated and validated with respect to the experimental data recently provided in chapter 2 on several quasi-static experiments performed at Northwestern University. These experiments were carried out on two different types of concrete: Reactive and Non-Reactive concrete which vary in their aggregate selection. LDPM parameters relevant to quasi-static experiments are calibrated by methodically tting the results of the numerical simulations with the provided experimental data. Using the calibrated parameters, the validation procedure is performed by simulating the experiments that that were not used in the calibration process.

3.1.1. The Lattice Discrete Particle Model (LDPM)

Recently,the Lattice Discrete Particle Model (LDPM), a meso-scale discrete model has been developed to simulate the mechanical behavior of concrete. The LDPM is capable of mimicking the mechanical interactions between coarse aggregates ingrained in a cementitious matrix. The material parameters of the model control directly the nature of the interactions between the particles of an assemblage of grains.

Figure 1 illustrates the steps in the generation process of concrete internal structure. As concrete has a granular internal structure, coarse aggregates, modeled by perfect spheres are randomly distributed within a given volume. The application of boundary

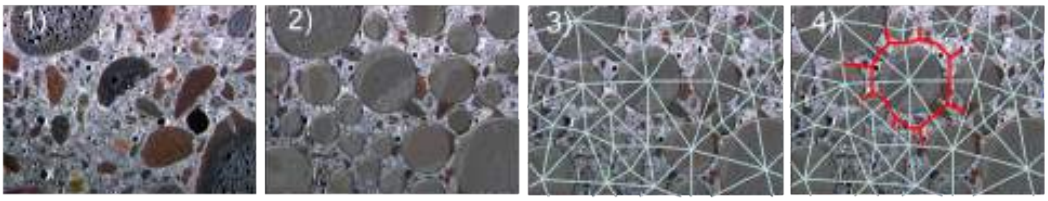

(a) (1) Concrete material modeled. (2) Supporting particles for grain generation. (3) Delaunay tetrahedralization. (4) Laminated structure model.

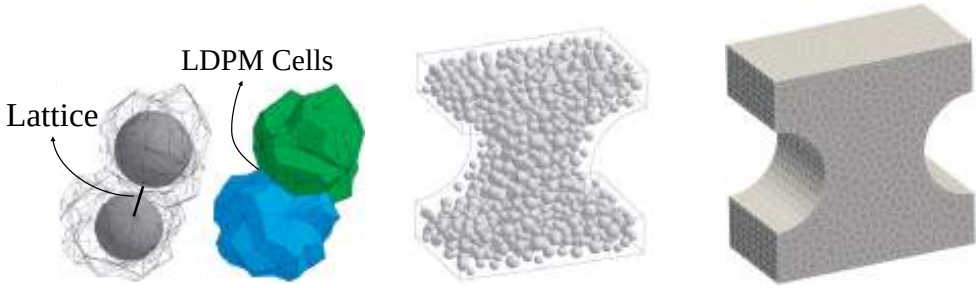

(b) (c) (d)

Figure 3.1. (a)(1) Concrete material modeled. (2) Supporting particles for grain generation. (3) Delaunay tetrahedralization. (4) Laminated structure model. (b) Spherical particle and (c) polyhedral cell representations of a typical dogbone specimen.

conditions is here facilitated by distributing infinitely small aggregates (radius=0) on the external surface.

The topology of the grains is defined through Delaunay tetrahedralization that discretizes a given volume into a 3D mesh of tetrahedras. Then, a 3D domain tessellation integrated to the Delaunay tetrahedralization allows for the creation of a 3D polyhedral-cells system. Within this system, the adjacent polyhedral-cells interact through triangular facets, assumed to be the location of the potential concrete failure. Figure 2 illustrates an aggregate representation in the LDPM, a perfect sphere embedded in a cementitious matrix.

LDPM constructs the geometrical representation of concrete meso-structure through the following steps. 1) The coarse aggregate pieces, whose shapes are assumed to be

spherical, are introduced into the concrete volume by a try-and-reject random procedure. 2) Zero-radius aggregate pieces (nodes) are randomly distributed over the external surfaces to facilitate the application of boundary conditions. 3) A three-dimensional domain tessellation, based on the Delaunay tetrahedralization of the generated aggregate centers, creates a system of polyhedral cells (see Figure 3.1a) interacting through triangular facets and a lattice system composed by the line segments connecting the particle centers. Figures 3.1c and d represent spherical particle and corresponding polyhedral representations of a typical dogbone specimen.

In LDPM, rigid body kinematics is used to describe the deformation of the lattice/particle system and the displacement jump, $[\![\mathbf{u}_C]\!]$, at the centroid of each facet is used to define measures of strain as

$$e_N = \frac{\mathbf{n}^{\mathrm{T}}[\![\mathbf{u}_C]\!]}{\ell}; \quad e_L = \frac{\mathbf{l}^{\mathrm{T}}[\![\mathbf{u}_C]\!]}{\ell}; \quad e_M = \frac{\mathbf{m}^{\mathrm{T}}[\![\mathbf{u}_C]\!]}{\ell} \tag{3.1}$$

where ℓ = interparticle distance; and $\mathbf{n}$, $\mathbf{l}$, and $\mathbf{m}$, are unit vectors defining a local system of reference attached to each facet.

Next, a vectorial constitutive law governing the behavior of the material is imposed at the centroid of each facet. In the elastic regime, the normal and shear stresses are proportional to the corresponding strains: $t_N = E_N e_N^* = E_N(e_N - e_N^0)$; $t_M = E_T e_M^* = E_T(e_M - e_M^0)$; $t_L = E_T e_L^* = E_T(e_L - e_L^0)$, where $E_N = E_0$, $E_T = \alpha E_0$, E_0 = effective normal modulus, and α = shear-normal coupling parameter; and e_N^0, e_M^0, e_L^0 are mesoscale eigenstrains that might arise from a variety of phenomena such as, but not limited to, thermal expansion, shrinkage, and ASR expansion.

For stresses and strains beyond the elastic limit, LDPM mesoscale nonlinear phenomena are characterized by three mechanisms as described below.

Fracture and cohesion due to tension and tension-shear. For tensile loading ($e_N^* > 0$), the fracturing behavior is formulated through an effective strain, $e = \sqrt{e_N^{*2} + \alpha(e_M^{*2} + e_L^{*2})}$, and stress, $t = \sqrt{t_N^2 + (t_M + t_L)^2/\alpha}$, which define the normal and shear stresses as $t_N = e_N^*(t/e)$; $t_M = \alpha e_M^*(t/e)$; $t_L = \alpha e_L^*(t/e)$. The effective stress t is incrementally elastic ($\dot{t} = E_0\dot{e}$) and must satisfy the inequality $0 \leq t \leq \sigma_{bt}(e, \omega)$ where one can define $\sigma_{bt} = \sigma_0(\omega)\exp\left[-H_0(\omega)\langle e - e_0(\omega)\rangle/\sigma_0(\omega)\right]$, $\langle x\rangle = \max\{x, 0\}$, and $\tan(\omega) = e_N^*/\sqrt{\alpha}e_T^* = t_N\sqrt{\alpha}/t_T$, $e_T^* = \sqrt{e_M^{*2} + e_L^{*2}}$, and $e_0(\omega) = \sigma_0(\omega)/E_0$. The post peak softening modulus is defined as $H_0(\omega) = H_t(2\omega/\pi)^{n_t}$, where H_t is the softening modulus in pure tension ($\omega = \pi/2$) expressed as $H_t = 2E_0/\left(l_t/l_e - 1\right)$; $l_t = 2E_0G_t/\sigma_t^2$; l_e is the length of the tetrahedron edge; and G_t is the mesoscale fracture energy. LDPM provides a smooth transition between pure tension and pure shear ($\omega = 0$) with parabolic variation for strength given by $\sigma_0(\omega) = \sigma_t r_{st}^2\Big(-\sin(\omega) + \sqrt{\sin^2(\omega) + 4\alpha\cos^2(\omega)/r_{st}^2}\Big) \;/\; [2\alpha\cos^2(\omega)]$, where $r_{st} = \sigma_s/\sigma_t$ is the ratio of shear strength to tensile strength.

Compaction and pore collapse from compression. Normal stresses for compressive loading ($e_N^* < 0$) are computed through the inequality $-\sigma_{bc}(e_D^*, e_V^*) \leq t_N \leq 0$, where σ_{bc} is a strain-dependent boundary function of the volumetric strain, e_V^*, and the deviatoric strain, $e_D^* = e_N^* - e_V^*$. The volumetric strain is computed by the volume variation of the Delaunay tetrahedra as $e_V^* = \Delta V/3V_0$ and is assumed to be constant for all facets belonging to a given tetrahedron. Beyond the elastic limit, $-\sigma_{bc}$ models pore collapse as a linear evolution of stress for increasing volumetric strain with stiffness H_c for $-e_V^* \leq e_{c1}^* = \kappa_{c0}e_{c0}^*$: $\sigma_{bc} = \sigma_{c0} + \langle -e_V^* - e_{c0}^*\rangle H_c(r_{DV})$; $H_c = (H_{c0} + H_{c1})/(1 + \kappa_{c2}\langle r_{DV} - \kappa_{c1}\rangle) + H_{c1}$ with

$H_{c1} > H_c0$; σ_{c0} is the mesoscale compressive yield stress; $r_{DV} = |e_D|/(e_V^* - e_{r0})$ for $e_V^* \leq 0$ and $r_{DV} = |e_D^*|/e_{V0}$ for $e_V^* > 0$, $e_{VO}^* = k_{c3}e_0$, $k_{c3} = 0.1$ and κ_{c1}, κ_{c2} are material parameters. Compaction and rehardening occur beyond pore collapse ($-e_V^* \geq e_{c1}^*$). In this case one has $\sigma_{bc} = \sigma_{c1}(r_{DV}) \exp\left[(-e_V^* - e_{c1}^*)H_c(r_{DV})/\sigma_{c1}(r_{DV})\right]$ and $\sigma_{c1}(r_{DV}) = \sigma_{c0} + (e_{c1}^* - e_{c0}^*)H_c(r_{DV})$.

Friction due to compression-shear. The incremental shear stresses are computed as $\dot{t}_M = E_T(\dot{e}_M^* - \dot{e}_M^{*p})$ and $\dot{t}_L = E_T(\dot{e}_L^* - \dot{e}_L^{*p})$, where $\dot{e}_M^{*p} = \dot{\lambda}\partial\varphi/\partial t_M$, $\dot{e}_L^{*p} = \dot{\lambda}\partial\varphi/\partial t_L$, and λ is the plastic multiplier with loading-unloading conditions $\varphi\dot{\lambda} \leq 0$ and $\dot{\lambda} \geq 0$. The plastic potential is defined as $\varphi = \sqrt{t_M^2 + t_L^2} - \sigma_{bs}(t_N)$, where the nonlinear frictional law for the shear strength is assumed to be $\sigma_{bs} = \sigma_s + (\mu_0 - \mu_\infty)\sigma_{N0}[1 - \exp(t_N/\sigma_{N0})] - \mu_\infty t_N$; σ_{N0} is the transitional normal stress; μ_0 and μ_∞ are the initial and final internal friction coefficients.

Finally, the governing equations of the LDPM framework are completed through the equilibrium equations of each individual particle.

Rate dependence of LDPM is captured by introducing a rate dependent function into the facet strain dependent boundary function previously described in Section 4.4.1 as $\sigma_{bt} = F(\dot{\omega})\sigma_0(\omega)\exp\left[-H_0(\omega)\langle e - e_0(\omega)\rangle/\sigma_0(\omega)\right]$ where rate dependent function $F(\dot{\omega}) = 1 + c_1 a \sinh(\dot{e}/(c_0/l))$, see [**69**] for details.

Aging model

In the original LDPM publications, the mesoscale parameters E_0, σ_t, r_{st}, l_t, σ_{c0}, σ_{N0}, α, H_{c0}/E_0, H_{c1}/E_0, κ_{c0}, κ_{c1}, κ_{c2}, κ_{c3}, μ_0 and μ_∞ are constant. In this study, however, the interest is the evolution of the mechanical behavior at early age. To account for early age effects, LDPM was recently equipped with an aging model [**76**].

One can write

$$E_0 = E_0^{\infty}\lambda \tag{3.2}$$

$$\sigma_t = \sigma_t^{\infty}\lambda^{n_a},\ \sigma_{c0} = \sigma_{c0}^{\infty}\lambda^{n_a},\ \sigma_{N0} = \sigma_{N0}^{\infty}\lambda^{n_a} \tag{3.3}$$

$$r_{st} = r_{st}^{\infty}\lambda^{m_a} \tag{3.4}$$

$$l_t = l_t^{\infty}(k_a(1-\lambda)+1) \tag{3.5}$$

where λ is the aging degree (fully described in the next paragraph), E_0^{∞}, σ_t^{∞}, σ_{c0}^{∞}, σ_{N0}^{∞}, r_{st}^{∞} and l_t^{∞} are the asymptotic values of the aforementioned parameters, n_a, m_a and k_a are material parameters. The other parameters are assumed to be age-independent. It is worth mentioning that in the work of [**76**], r_{st} was taken as age-independent, i.e. assuming $m_a = 0$.

Cement hydration of mortar that causes the evolution in strength is described through the Hygro-Thermo-Chemical (HTC) model. The model computes at any age the heat transfer and moisture diffusion in concrete and mortar, through coupled diffusion equations involving the variation of temperature T, moisture h, moisture permeability D_h, cement hydration degree α_c, evaporable water w_e and other material properties. The relevant sets of equations, namely Fick's law, moisture permeability equation, unit volume mass balance, sorption/desorption isotherm, Fourier's law and enthalpy balance equation are reported in the Appendix.

The chemical reactions involving the four different cement clinker phases and water are accounted for in average by computing the so-called degree of hydration α_c through the following empirical differential equation [**25**]:

$$\dot{\alpha}_c = A_{c1}\left(\frac{A_{c2}}{\alpha_c^\infty} + \alpha_c\right)\left(\alpha_c^\infty - \alpha_c\right)e^{-\frac{\eta_c \alpha_c}{\alpha_c^\infty}}\beta(h)e^{-\frac{E_{ac}}{RT}} \tag{3.6}$$

where A_{c1}, A_{c2} and η_c are material parameters, α_c^∞ is the asymptotic hydration degree that can be approximately calculated as $\alpha_c^\infty = 1.031(w/c)/(0.194 + (w/c))$ and $\beta(h) = [1 + (5.5 - 5.5h)^4]^{-1}$ is an empirical function that describes the effect of moisture content, E_{ac} is the hydration activation energy.

Once the degree of hydration is computed, one needs to relate it to the mechanical properties of mortar. It is well accepted that the strength evolution depends on the degree at which the chemical reactions occurred but also the curing temperature. One can thus introduce an internal variable λ, the aging degree, that takes into account both effects through the following equation [**46**]:

$$\dot{\lambda} = \dot{\alpha_c}\Big[A_{\lambda 0} + A_\lambda(\alpha_c^\infty + \alpha_0 - 2\alpha_c)\Big]\left(\frac{T_{max} - T}{T_{max} - T_{ref}}\right)^{n_\lambda} \tag{3.7}$$

for $\alpha > \alpha_0$ and $\dot{\lambda} = 0$ for $\alpha \leqslant \alpha_0$, where α_0 is the value of the hydration degree at which mortar starts to get a solid consistency, $A_{\lambda 0} = (\alpha_c^\infty - \alpha_0)^{-1}$, A_λ is a material parameter, T_{max} and T_{ref} are the maximum temperature at which mortar can harden and the room temperature respectively.

In terms of numerical implementation, the hygro-thermo-chemo-mechanical coupling is performed as follows: once the geometry of the specimen is considered, a tetrahedral

Finite Element (FE) mesh is generated. The HTC model equations are solved numerically and the state variables such as temperature, moisture content, degree of hydration and aging degree are computed at the nodes. Then, their values are interpolated to the nearest facet centroids by using the FE shape function associated to each tetrahedron. Each facet now has at any time step the updated value of the aging degree, which allows to update the mesoscale LDPM parameters through the aging equations.

Creep model: The volume fraction of cement gel produced by early age chemical reactions and the cement gel viscoelastic strain rate are respectively defined through $\nu(\alpha_c) = (\alpha_c/\alpha_c^{\infty})_{\alpha}^{n}$ and $\dot{\gamma}$, where n_α is a calibrated model parameter. The non aging portion of the cement gel compliance is expressed through $\Phi(t-t_0)$=$\xi_1 ln[1+(t-t_0)^{0.1}]$ where ξ_1 is a model parameter that is calibrated. The hygral and thermal effects on creep are commonly accepted by the scientific community and Bažant et al. [**9**], have demonstrated that in low relative humidity environments, the creep measured was larger due to shrinkage that was causing a non linear increase of the generated creep strains. Also, the worked performed by Bažant et al. in 1978 in [**84**] has shown that higher temperatures can significantly increase concrete creep. The ladder observations were formulated into one function which includes both hygral and thermal effects and is expressed as follows:

$$\Psi(t) = [0.1 + 0.9h^2] \exp\left[\frac{Q_\nu}{R}\left(\frac{1}{T_0} - \frac{1}{T}\right)\right] \tag{3.8}$$

where h is the relative humidity, T represents the temperature in Kelvins, t the time, R the universal gas constant and Q_ν the activation energy for the cement gel chemical reactions to happen. The viscoelastic strain rate can now be defined as follows:

$$\dot{\mathbf{e}}^{\nu}(t) = \left(\frac{\alpha_c^{\infty}}{\alpha_c}\right)^{n_\alpha} \times \int_0^t \Phi(t_r(t) - t_r(\tau))\mathbf{G}\dot{\sigma}d\tau \tag{3.9}$$

The unrecoverable part of the creep strain corresponds to purely viscous behavior (plastic deformation) of concrete which is also associated with long term creep. Similarly, the hygral and thermal effects on the viscous behavior are defined through :

$$\dot{\mathbf{e}}^{f} = \xi_2\kappa_0\psi(t)S\mathbf{G}\sigma \tag{3.10}$$

where S denotes the microprestress obtained by solving $\dot{S}+\Psi_s(t)\kappa_0 S^2=\kappa_1[\dot{T}ln(h)+\dot{T}\dot{h}/h]$, where κ_0, κ_1 and ξ_2 are parameters of the model to be calibrated. Similarly to the function Ψ presented in the previous section, a function Ψ_s accounts for the viscous behavior change due to hygral and thermal effects. Ψ_s can be expressed as follows:

$$\Psi_s(t) = [0.1 + 0.9h(t)^2] \exp\left[\frac{Q_\nu}{R}\left(\frac{1}{T_0} - \frac{1}{T}\right)\right] \tag{3.11}$$

It is worth mentioning that the free parameters κ_0, κ_1 and ξ_2 are not independent. Indeed the product $\kappa_0\kappa_1$ will only affect the creep behavior under varying environmental conditions (Temperature and relative humidity). However, the ξ_2 parameter will always affect the viscous behavior of concrete whether it is in the case of autogeneous creep or

basic creep.

ASR model: The ASR model describes the gel formation and expansion at the aggregate level. The model distinguishes for each aggregate particle the gel formation and the effect of water imbibition. It is important to point out that smaller length scale processes are averaged and only phenomenologically represented; this includes 1) the actual chemistry of gel formation, 2) the micro-transport phenomena of ions in gel, pores and cracks, 3) the gel transport in pores and cracks. Since the silica present in the aggregate needs to be in contact with the surrounding water and alkali ions present in the cement paste for the ASR gel to be formed, it can be assumed that gel formation is governed by a diffusion process. This approach is based on the observation that the time scale of the alkali-silica reaction is much shorter than the one of diffusion. For very small particles, this assumption might not be accurate [**62**]. However, for computational cost considerations, the model proposed in this study only focuses on the coarser portion of the particle size distribution for which, indeed, the diffusion process is dominant. The effect of the particles not directly resolved is included indirectly in the parameters of the model constitutive equations. The process can be described by the following radial diffusion equation for each spherical particle of diameter D [**85**]:

$$\dot{z} = -\frac{w_e}{z - \frac{2z^2}{D}} \kappa_{z0} e^{\frac{E_{ag}}{RT_0} - \frac{E_{ag}}{RT}} \tag{3.12}$$

where z is the diffusion front position, w_e is the evaporable water defined in the Appendix (see Equations 4.2 and 4.3), k_{z0} is a material parameter, and E_{ag} is the gel diffusion activation energy.

The mass of gel M_g formed surrounding one aggregate is then computed as [**17**]:

$$M_g = \frac{\kappa_a \rho_g \pi}{6}(D^3 - 8z^3) \tag{3.13}$$

where ρ_g is the density of the ASR gel, $\kappa_a = \min(\langle c_a - c_{a0}\rangle/(c_{a1} - c_{a0}), 1)$ where c_a is the macroscopic alkali concentration and c_{a1} is the saturation alkali content for which the reaction is complete. c_{a0} is the threshold alkali content at which no expansion is observed. Although it was found [**70, 42**] that this threshold depends on several factors, including but not limited to calcium concentration, the present study assumes, as a simplification, c_{a0} to be constant.

Once the gel is created, it is assumed to imbibe water. For a fixed temperature, the water imbibition rate $\dot{M}_i$ is characterized as a linear function of the gel mass M_g as follows [**3**]:

$$\dot{M}_i = \frac{C_i}{\delta^2}[M_g \kappa_{i0} e^{\frac{E_{ai}}{RT_0} - \frac{E_{ai}}{RT}} - M_i] \tag{3.14}$$

The bulk diffusivity of imbibed water C_i includes the contribution of the cement paste, as well as the external rim of the aggregate particle: $C_i = C_{i0}\exp(E_{aw}/(RT_0) - E_{aw}/(RT))$. E_{ai} and E_{aw} are the activation energies of respectively the imbibition capacity and the diffusion process. κ_{i0} and C_{i0} are material parameters. δ characterizes the thickness through which water is transported from the cement paste to the surrounding of the aggregate

where the ASR gel lies. Petrographic observations (Figure 2.2b) suggests that such a distance is in the order of a few micrometers (which is confirmed later by calibration results). It is reasonable to assume that the water present in a generic location has approximately the same distance to travel to reach each of the surrounding aggregate particles of the same size. One can thus assume that $\delta = \alpha_M D$ where α_M is a proportionality parameter as introduced by Alnaggar et al.[**3**]. One can then define $\tilde{C}_i = C_i/\alpha_M^2$ in Equation 3.14.

To accommodate the change in volume due to water imbibition, material expansion must occur. In the simple case of two interacting particles, the expansion can be simulated by a change in radius of both particles, which, in turn, generates a so-called imposed strain or LDPM eigenstrain $\mathbf{e}^a$ at the adjacent facet. By assuming negligible the LDPM shear eigenstrains e_M^a and e_L^a, only the contribution of the normal eigenstrain e_N^a is taken in account. By considering δ_c the equivalent thickness of capillary pores surrounding the aggregate and accessible to the gel (assumed constant and independent of D, one can define the amount of imbibed water as $\langle M_i - M_i^0 \rangle$ where $M_i^0 = (4\pi\rho_w/3)((r+\delta_c)^3 - r^3)$. One can then write the increase in radius $r_i = [3\langle M_i - M_i^0\rangle/4\pi\rho_w + r^3]^{1/3}$. Then, by computing the rate of increase $\dot{r}_i = [\dot{M}_i/(4\pi\rho_w)][3\langle M_i - M_i^0\rangle/4\pi\rho_w + r^3]^{-2/3}$. Finally, the imposed normal strain due to ASR can be defined as

$$\dot{\mathbf{e}}_N^a = \frac{\dot{r}_{i1} + \dot{r}_{i2}}{l} \tag{3.15}$$

where r_{i1} and r_{i2} are the increases in radii of the aggregate particles 1 and 2 at a distance l from each other.

The hygral and thermal deformations are respectively assumed to be proportional to the humidity and temperature rate. The corresponding strain rates can be expressed as follow:

$$\dot{\mathbf{e}}^{sh} = \alpha_{sh}\dot{h} \tag{3.16}$$

$$\dot{\mathbf{e}}^{T} = \alpha_{T}\dot{T} \tag{3.17}$$

with α_{sh} and α_T respectively the shrinkage and thermal expansion coefficients of proportionality related to concrete properties. It is worth mentioning that the shrinkage coefficient is taken constant while in Bažant et al. [**10**] a new formulation of this coefficient was proposed which includes the aging of α_{sh}.

As explained by Alnaggar et al. [**17**], the additivity of strains is assumed and leads to the following expression of the strain rate:

$$\dot{\mathbf{e}} = \dot{\mathbf{e}}^{sh} + \dot{\mathbf{e}}^{a} + \dot{\mathbf{e}}^{\star} + \dot{\mathbf{e}}^{sh} + \dot{\mathbf{e}}^{T} + \dot{\mathbf{e}}^{\mu} + \dot{\mathbf{e}}^{f} \tag{3.18}$$

where $\dot{\mathbf{e}}^{\star}$ represents the effect of instantaneous elasticity and damage, $\dot{\mathbf{e}}^{a}$ a represents the ASR induced strain rate; $\dot{\mathbf{e}}^{sh}$ and $\dot{e}^{T}$ are shrinkage and thermal strain rates (respectively); $\dot{\mathbf{e}}^{\nu}$ is the viscoelastic strain rate and $\dot{\mathbf{e}}^{f}$ is the purely viscous strain rate.

3.2. Numerical modeling of experimental results

This section focuses on the modeling of the experimental results relevant to concrete mechanical properties under ASR. Table 3.1 summarizes the geometries of the concrete

samples that were tested throughout the experimental campaign. The experimental results can be subdivides into three categories:

- Material diffusional properties
- Non reactive concrete samples strength characterization
-

Table 3.1. Geometries and ages of Testing

	Dimensions [mm^3]	Testing ages [days]
Compression	75x75x75	60/120/365
3-point bending	75x75x250	60/90/120/240/300/365
Brazilian	r=100mm h=200mm	60/120/365
Creep	75x75x75	365
Expansion	75x75x250	400
Shrinkage	75x75x250	365

3.2.1. Concrete Modeling

The Lattice Discrete Particle Model (LDPM) and the Hygro-Thermo-Chemical (HTC) model are here used to simulate concrete mechanical and diffusional behaviors. A preliminary definition of the material aggregate distribution is however required to achieve accurate particle interactions modeling. In the LDPM, the particles distribution within a given concrete volume is adjusted through the Fuller coefficient defined in Equation 3.19. Table 3.2a presents the experimental aggregate size distribution of the considered concrete. Respectively, the maximum and minimum aggregate sizes are 19 and 4.5 mm. Given the aggregate size distribution, one can plot the Fuller curve based on the following

formula:

$$F(d) = \left(\frac{d}{d_0}\right)^{n_F} \tag{3.19}$$

where n_F=1.1 and respectively d and d_0 represents the actual and maximum aggregate sizes. Figure 3.2b shows the LDPM calibration of the aggregate size distribution in terms of Fuller coefficient versus aggregate diameters. The LDPM results are in excellent agreement with the experimental observations and show that LDPM is largely capable of modeling concrete internal structure at the aggregates level. Figures 3.2c and d respectively present the LDPM mesh and particles distribution in the case of a 3-Point bending test, i.e. 75 mm x 75 mm x 285 mm concrete samples.

a)

Sieve size		
Passing %	Retained %	Mass
19 mm	12.5 mm	33 %
12.5 mm	9.5 mm	33 %
9.5 mm	4.5 mm	33 %

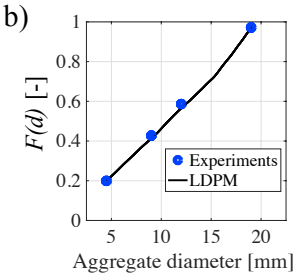

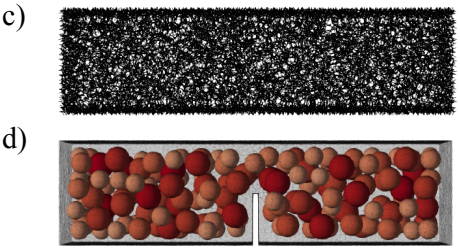

Figure 3.2. a) Concrete aggregate size distribution. b) Fuller/sieve curve LDPM calibration. Concrete sample c) Mesh and d) Particles distribution in LDPM.

3.2.2. Shrinkage test

Concrete is commonly known to expand/shrink when subjected to hygral variations causing the gain/loss of capillary water. In order to identify concrete diffusional properties, shrinkage tests were performed on and are presented here. Measurements of weight loss were performed on 75 mm x 75 mm x 285 mm concrete samples drying at 55% RH and

		Reactive Concrete	Non Reactive Concrete
Materials	Extra Information	Quantity [kg/m^3]	Quantity [kg/m^3]]
Portland Cement	Holcim St. Genevieve Type 1	420.04	420.04
Coarse Aggregate	Spratt Coarse	1078.58	-
Coarse Aggregate	Lafarge Fox River	-	1078.58
Sodium Hydroxide	Lab Stock	4.15	4.15
Fine Aggregate	Hanson Plum Run Peebles, OH	718.46	718.46
Water	Potable	176.2	176.2
Water/Cement		0.42	0.42
Superplasticizer	BASF Glenium 7500	3.2	3.2

Table 3.2. Mix design summary (in accordance with ASTM 192).

23° C. Initially, the samples are saturated and start losing capillary water as they are being exposed to a lower RH environment. Also, the difference of RH between the sample outer surfaces and its heart is the cause of tensile stresses leading to concrete cracking.

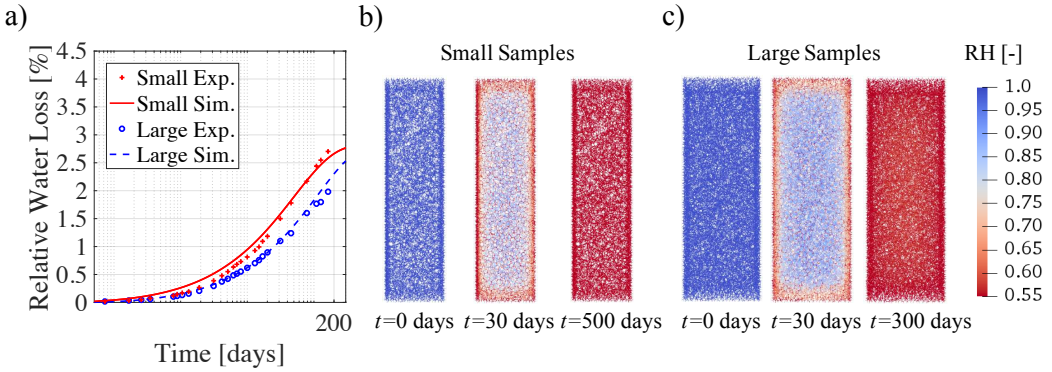

Figure 3.3. a) Shrinkage tests LDPM calibration results in terms of relative water loss versus time. Relative humidity evolution over time in b) Small (75x75x285 mm^3) and c) Large (100x100x285 mm^3).

Figure 3.3a presents the results of the average relative weight loss measurements over-time of six concrete samples, three small (75 mm x 75 mm x 285 mm) and 3 large (100

Table 3.3. HTC parametric identification.

Param.	Param. Defintion	Calibration Method	Value	Units
D_0	Permeability (low RH)	Shrinkage test	4.5×10^{-6}	kg m^{-1} h^{-1}
D_1	Permeability (high RH)	Shrinkage test	1.45×10^{-3}	kg m^{-1} h^{-1}
n	Transition D_0 to D_1	Shrinkage test	2.2	-
A_{c1}	Cement hydration	Calorimetric test	9×10^{7}	h^{-1}
A_{c2}	Cement hydration	Calorimetric test	1×10^{-2}	-
η_c	Cement hydration	Calorimetric test	8	-
ρ	Concrete density	Density	2591	kg m^{-3}
k_{vg}^c	Desorption isotherm for CSH gel water	Long term drying	0.2	-
g_1	Desorption isotherm for capillary water	Long term drying	1.5	-

mm x 100 mm x 285 mm) in total. The HTC model was used to simulate concrete drying by identifying the moisture permeability parameters D_0, D_1 and n. Table 3.3 lists the identified parameters for this simulation along with values of other HTC parameters that had to be assumed based on existing literature. Figure 3.3a shows great agreement between the HTC simulation and experimentally measured water loss results. As the diffusion parameters associated with the tested concrete were identified based on the relative weight loss of small samples only, the results obtained for the large samples constitute a pure prediction. Respectively, Figures 3.2c and 3.3b and c show the HTC mesh used and the simulated RH evolution over time of the modeled concrete samples.

3.2.3. Thermal expansion

Similarly to hygral deformations, concrete can be subjected to thermal deformations that are computed as follows:

$$\dot{\mathbf{e}_{th}} = \alpha_T \dot{T} \tag{3.20}$$

A one way formulation between the HTC and LDPM was established allowing for accurate modeling of concrete thermal deformations.The temperature effect is assumed to be proportional to the temperature rate as described in Equation 2.

Figure 3.4a shows the calibration results of the thermal expansion, which was measured on the non reactive concrete samples that were subjected to a sudden increase in temperature when moved from the fog rooms at 100% RH 23° C to the high temperature curing rooms set at 38° C and 50° C. The results are presented in terms of microstrains versus time (in days) and are in good agreement with the experimental results for α_{sh}=1.45×10^{-3} and α_{th}=5×10^{-6} C^{-1}. Figure 3.4 shows the temperature profile in the modeled LDPM concrete samples. The identified HTC parameters are summarized in Table 3.3.

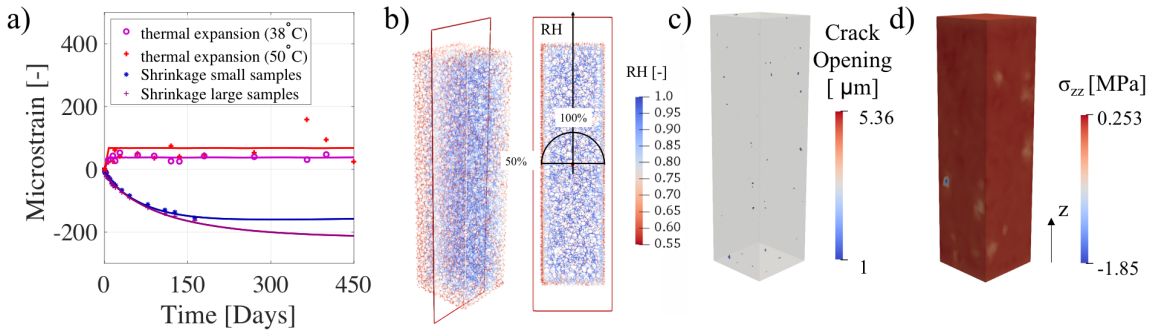

Figure 3.4. a) Thermal expansion and shrinkage results in terms of microstrains versus time in days. Shrinkage concrete samples b) relative humidity profile and c) crack contours d) ZZ-Stress distribution.

3.2.4. Aging results

As previously described, the parameters relevant to cement hydration in the HTC model [**25**] and [**45**] were calibrated using the experimental data of the semi-adiabatic test.

The aging parameters of the HTC model [**46**] and aging model parameters [**77**] were calibrated on the basis of the test results for non-reactive samples: compression and three point bending tests of concrete samples cured at 38°C and 50°C in fog room (100% RH). The effect of temperature on hydration kinetics is taken in account in the calibration as well.

Table 3.4. Aging parametric identification.

Param.	**Param. definition**	**Calibration**	**Value**	**Units**
E_0^{∞}	Asymp. Elastic Modulus	3 point bending tests	115	GPa
$f_t^{'\infty}$	Asymp. Tensile Strength	3 point bending tests	7.5	MPa
l_t^{∞}	Asymp. Characteristic Length	3 point bending tests	200	mm
σ_s/σ_t $^{\infty}$	Asymp. Shear Strength Ratio	Compression tests	3.8	-
n_a	Stress Aging Coeff.	3 point bending tests	2.47	-
m_a	Shear Strength Ratio Aging Coeff.	Compression tests	2	-
k_a	Characteristic Length Aging Coeff.	3 point bending tests	2.45	-
n_λ	Aging Temperature Exponent	Mechanical testing at 38 °C and 50°C	0.8	-
μ_0		Literature [1]	0.2	-
σ_{N0}		Literature [1]	600	MPa
σ_{c0}		Literature [1]	240	MPa
H_{c0}/E_0^{28}		Literature [3]	0.3	-
H_{c1}/E_0^{28}		Literature [3]	0.1	-
κ_{c0}		Literature [3]	4	-
E_d/E_0^{28}		Literature [3]	1	-

Figure 3.5 shows the calibration results of the calorimetric test in terms of temperature versus time. The measured temperature rise can be explained by the well known exothermic reaction of hydration occurring in concrete which governs strengthening. Figure 3.5b

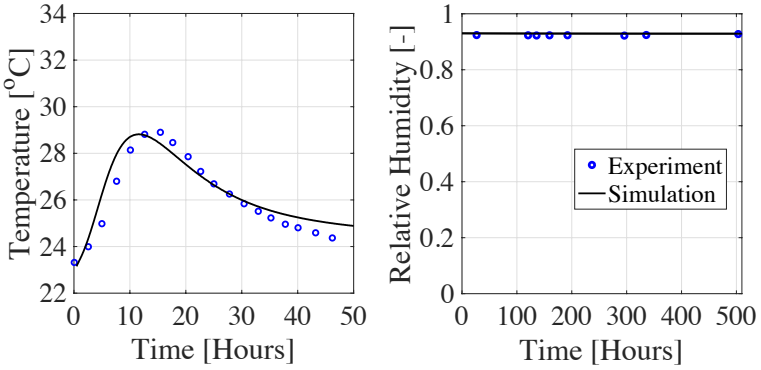

(a) Calorimetric test (b) Self-desiccation test

Figure 3.5. a)Calorimetric test results in terms of temperature (Celsius) versus time. b) Self-desiccation test results in terms of Relative Humidity versus time.

presents the self desiccation results which is here non existent. The identified parameters for these two tests are reported in Table 3.3.

The previously introduced calibration and modeling of the calorimetric experimental results now allows for the calibration of the aging model as hydration parameters are identified. The calibration of the aging model was based on the three point bending and compression test results of the non reactive samples for both temperature 38°C and 50 °C. The three point bending test was used to calibrate three material parameters, the tensile strength σ_t (peak), the elastic modulus E_0 (elastic/inital loading part) and the characteristic length l_t. The compression tests results were used for the calibration of the shear strength ratio σ_s/σ_t parameter. The calibration of concrete elastic properties is more accurate when based on the 3PBT as the test is performed CMOD control and thus more precise. Other LDPM material parameters that could not be identified based on those two tests were assumed from the existing literature and are given in Table 3.4 as well. The aging degree rate $\dot{\lambda}$ is calculated in the HTC model based on the hydration

and governs the evolution of concrete mechanical properties over time under various environmental conditions. As introduced by Wan et al. [**76**], the aging degree formulation includes relative humidity and temperature effects. As the considered samples were cured in saturated conditions, no hygral effect on the aging degree could be calibrated. On the other hand, the thermal effect on aging n_λ was calibrated based on the results obtained for the two curing temperature 38 °C and 50 °C.

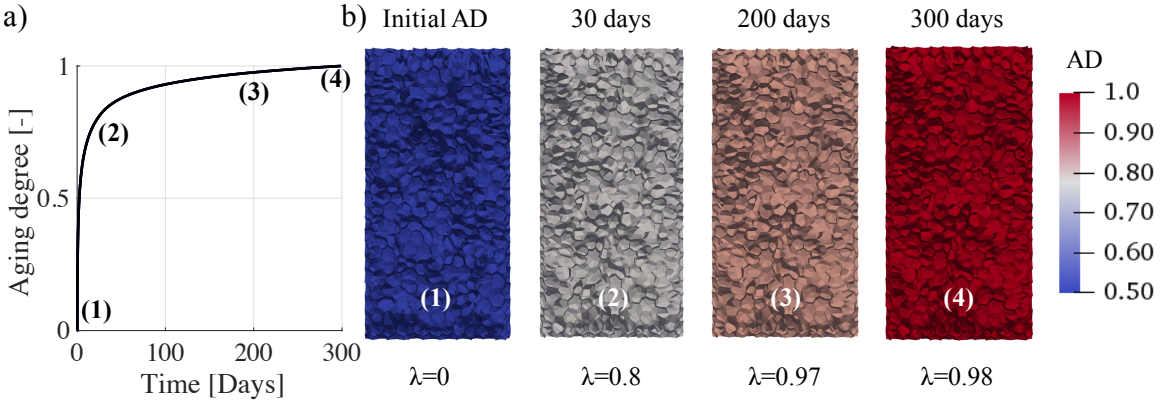

Figure 3.6. a) AD evolution versus time and b) AD LDPM contour in compression samples at different ages

Figure 3.6 shows the aging degree evolution which characterizes in the M-LDPM, concrete strengthening rate. One can notice a zero AD initially corresponding to the casting of concrete followed by an expected rapid gain of strength within the first 30 days. The AD contours in Figure 3.6b) display the AD evolution at different stages of concrete aging presenting naturally an increasing aging degree as the concrete samples age.

Figure 3.7 a b and c show the results of the aging degree calibration for the three point bending and compression tests for age 58, 158 and 393 days at 38°C. The parameter n_s

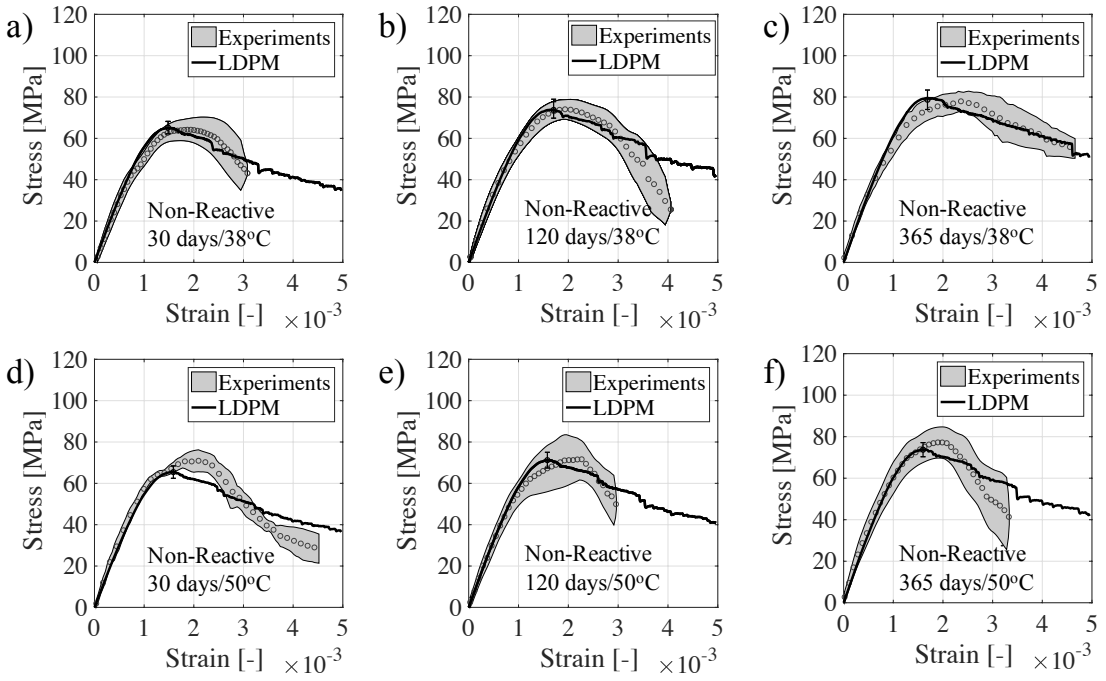

Figure 3.7. Results of uniaxial compression test calibration in terms of stress versus strain for reactive samples at the age of a) 30, b) 120 and c) 365 days at 38°C and d) 30 e) 120 and f) 365 days at 50°C.

given in each plot window represents the number of samples tested. The grey shade represents the experimental scatter and characterizes the upper and lower limit of the experimental results. The comparison of the results is presented in terms of load versus Crack Mouth Opening Displacement (CMOD) and the simulations are in great agreement with the experimental results.

Similarly, Figure 3.8 a b and c show the results of the aging degree calibration for the three point bending and compression tests for age 58, 158 and 393 days at 50°C.

After one year, the concrete samples cured at 38°C and 50°C respectively experience an increase of approximately 21% and 10% of their compressive strengths due to aging. This observation suggests that for higher curing temperatures, concrete samples are subjected

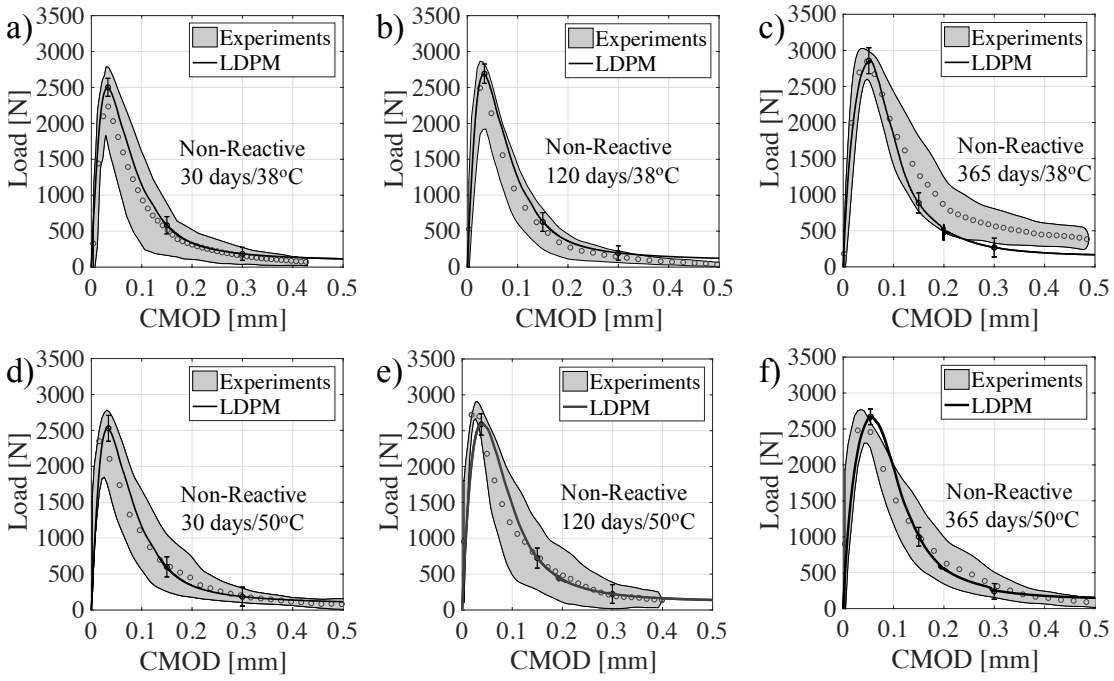

Figure 3.8. Results of 3 point bending test calibration in terms of load versus CMOD for non-reactive samples at the age of a) 30, b) 120 and c) 365 days at 38°C and d) 30 e) 120 and f) 365 days at 50°C.

to less aging and concrete strengthening becomes less important than at lower temperatures (i.e. the results at 38°C). Similarly, the elastic modulus E_0 and tensile strength σ_t increase with time due to aging although less important at higher temperatures. Last but not least, the characteristic length l_t decreases with time, this observation correlates well with the idea that as concrete strengthens, it becomes less ductile and hence the characteristic length decreases which translates in stiffer softening (post peak behavior) for the 3-Point bending test results.

The identified LDPM and aging parameters are summarized in Table 3.4. The typical crack contours obtained with the M-LDPM for non reactive samples is given in Figures 3.9 for a) the compression test and b) 3 point bending test. The crack pattern was

found consistent throughout the whole year of testing in the simulation results similarly to what has been observed in the experiments. In compression, mostly vertical cracks are generated due to the stress application in the vertical direction which prevents the development of horizontal cracks. For the 3 point bending test, a vertical crack initiated from the notch propagates upward which agrees with experimental observations.

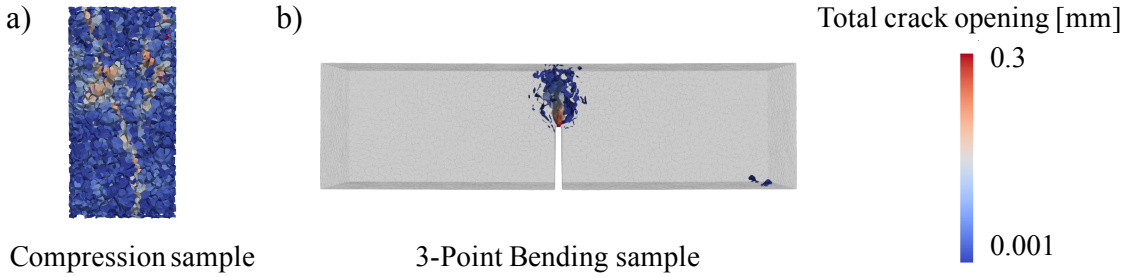

Figure 3.9. Typical crack contour observed in non reactive a) Compression and b) 3-point bending test simulation results

3.2.5. Creep Results

This section discusses the creep theory, calibration and prediction results.

It is worth mentioning that the previously identified material parameters are maintained and that in this section, the creep parameters only were calibrated. In the numerical simulations, the concrete samples are assumed to slide against the loading plates similarly to the experiments. The used friction coefficient is 0.18. To calibrate the creep parameters, 5 types of creep tests were conducted:

- Autogeneous creep on samples loaded at 28 days of age: AC28
- Autogeneous creep on samples loaded at 90 days of age: AC90
- Drying creep at 23°C/50%RH of samples loaded at 28 days of age:DC2350

- Drying creep at 38°C/100%RH of samples loaded at 28 days of age:DC38100
- Drying creep at 50°C/100%RH of samples loaded at 28 days of age:DC50100

The short term visco-elasticity ξ_1 and long term viscosity ξ_2 were calibrated on the AC28 group of experiments. While ξ_1 was mainly used to calibrate the early creep behavior, ξ_2 was the parameter that was fixed based on the long term creep deformation as explained in Section 1.2.3. The aging visco-elasticity parameter n_α affects the aging component of creep and is hence calibrated using the AC90 set of data as the samples were loaded at later age (concrete samples loaded at 90 days) which provides information directly related to the parameter n_α of interest. The thermal and hygral effect which are related to κ_0, κ_1 and ξ_3 were calibrated using the experimental data where the concrete samples were subjected to creep under different environmental conditions. The set of data relevant to drying creep at 23°C/50%RH, 23°C/38%RH and 50°C/100%RH. This calibration allows a full use of the experimental results as it exploits all different test conditions, from the age of loading to the effect of temperature and relative humidity on creep.

By following the procedure described above, one can identify the creep parameters ξ_1=2x10^{-12}N^{-1}m^2, ξ_2=20x10^{-12}N^{-1}m^2, n_α=-4, κ_0=6.0x10^{-15}N^{-2}m^{4}s^{-1}, κ_1=5x10^{7}N^{-1}m^{2}degK^{-1} and ξ_3=10^{-13}N^{-1}m^2.

3.2.6. Expansion Calibration

It is worth mentioning that during the ASR parameters calibration, all calibrated models (i.e. shrinkage, creep and aging) are used with no further adjustments to the parameters. The thermal expansion was directly subtracted to the expansion experimental results to

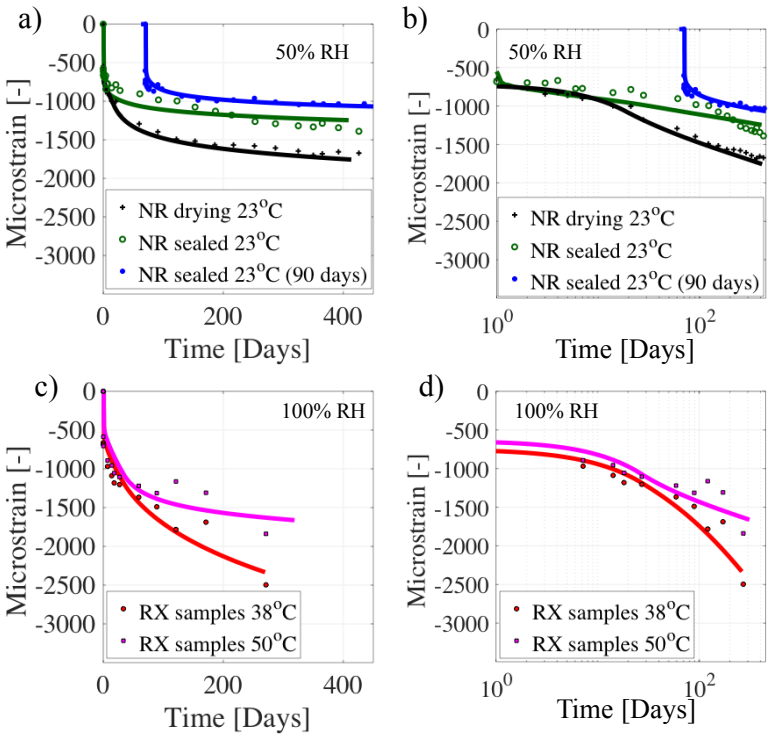

Figure 3.10. Concrete creep test results calibration in terms of microstrain versus a) time and b) log-time for drying samples at C50% RH/23°C and sealed loaded samples at 28 and 90 days of age. Concrete creep test results calibration in terms of microstrain versus c) time and d) log-time for samples subjected to 38°C/100% and 50°C/100% environmental conditions.

reduce the computational cost in the surrounding of this study. The M-LDPM which consists in the LDPM itself and its models aims at predicting ASR damages on concrete mechanical properties based on an ASR parameters identification performed on concrete expansions only. The samples experimental environmental conditions consisting in curing concrete at 100% RH 38°C and 50°C are replicated in the set of results presented in Figure 3.11. The M-LDPM is here used to model the ASR expansion at both temperatures 38°C and 50°C. As introduced in Section 1.2.4, ASR is modeled through two distinct processes which are the gel formation and water absorption. As the tests are performed

at constant temperature, κ_1 was the only parameter calibrated to account for full reaction time. Also, the experimental results display a lower asymptotical longitudinal expansion at higher temperature 50°C than at 38°C . The parameter δ_c represents the equivalent porosity thickness and governs in the simulation the initial portion of the longitudinal expansion as it characterizes the diffusion process of alkali ions through the porosity thickness. The amplitude of the longitudinal expansion, on the other hand, is mainly governed by C_i^0. In the experiments, sodium hydroxide was added to increase the kinetics of ASR and included in the simulations by setting c_a=5.125kg/m^3. Parameters such as the gel composition and silica content could not be inferred directly from the experiments and were assumed based on previous work [**2**]. The activation energies E_{ai}, E_{aw} and E_{ad} relevant to thermal effect on ASR were calibrated on the experimental results considering both experimental temperatures.

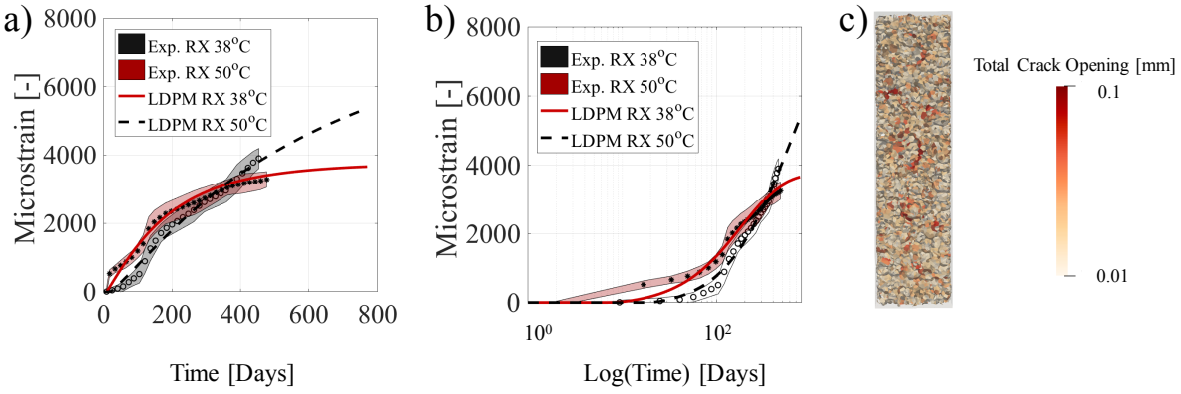

Figure 3.11. Free expansion calibration results in terms microstrains versus a) time and b) log of time. c) LDPM crack contours obtained for modeled concrete under free expansion due to ASR.

Last but not least, one could note in the experimental creep test results, no significant difference in terms of creep between the non reactive and reactive set of samples. This

observation suggests that the ASR gel formation has a negligible contribution to the longitudinal expansion, otherwise, one would notice a significant difference in terms of creep between the two batches. The preceding comment hence suggests that most of the deformation observed in free expansion is likely due to cracking and not the ASR gel expansion which remains minimal as observed by Alnaggar et Al [**17**] .

3.3. Prediction Results and Discussion

Figure 3.12 displays the results of uniaxial compression test calibration in terms of stress versus strain for reactive samples tested at the ages of 30, 120 and 365 days at 38°C/100%RH and 30, 120 and 365 days at 50°C/100%RH. Similarly to the experimental results, the predicted compressive strength evolution of the reactive samples does not evolve much when analyzed separately which would suggest little ASR effect without considerations of reference batch (non reactive samples). ASR damages on concrete mechanical properties are not directly measurable through a loss of strength but rather through an inhibition of strength gain (aging) at both temperatures. The M-LDPM correctly predicts for the reactive batch a compressive strength evolution nearly constant throughout one year by coupling aging that contributes to concrete strength build up and ASR damages which leads to "strength loss". As expected, at higher temperature 50°C more damages are observed on the long term although the asymptotic expansion is smaller which suggests that ASR damage rate plays an important role in concrete strength evolution.

Figure 3.13 presents the results of 3 point bending test calibration in terms of load versus CMOD for reactive samples at the age of 30, 120 and 365 days at 38°C and 30,

120 and 365 days at 50°C. The analysis proposed for the compressive strengh evolution under ASR remain valid for the 3 point bending test results but in this specific type of test, further explanations are needed.

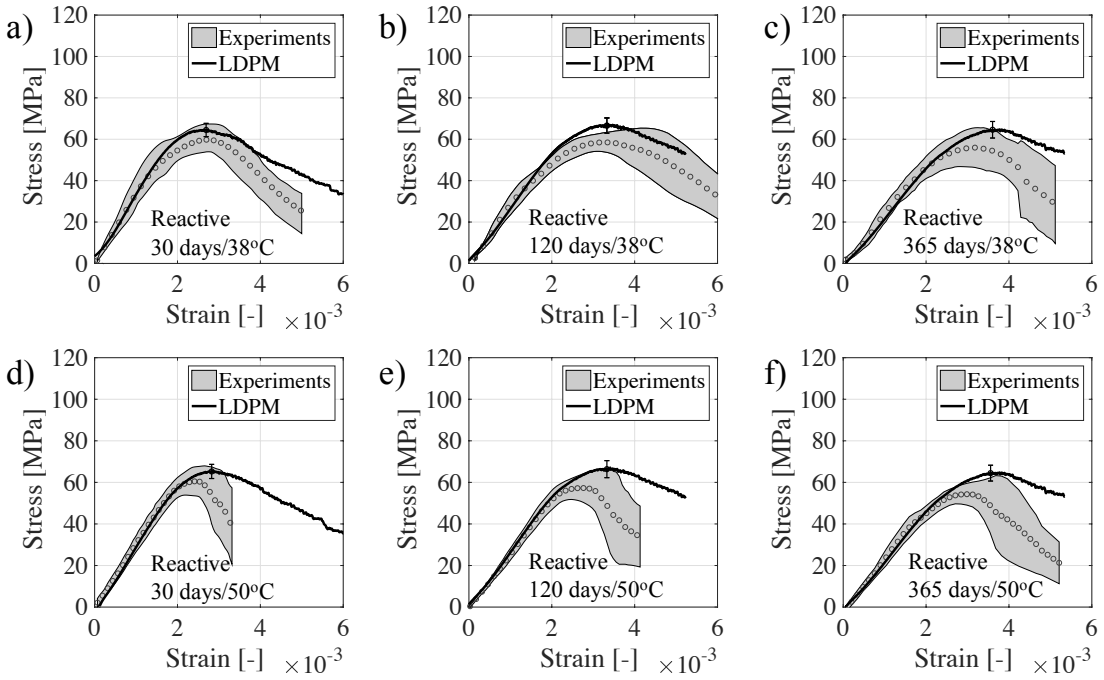

Figure 3.12. Results of uniaxial compression test calibration in terms of stress versus strain for reactive samples at the age of a) 30, b) 120 and c) 365 days at 38°C and d) 30 e) 120 and f) 365 days at 50°C.

Bažant et al. [**8**] as well as [**2**] have demonstrated that creep could mitigate ASR damages which led to an era of new model capable of realistically predict ASR effects on concrete strength as shown in Figures 3.13 and 3.12. Figure 3.14 presents the crack distributions obtained for a compression and 3 point bending test reactive concrete samples prior to loading with and without creep. The purpose of this annex analysis is to understand how can creep qualitatively mitigate ASR damages thanks to the M-LDPM which fully couples the main phyisical phenomenons at stake. Through Figure 3.14, the

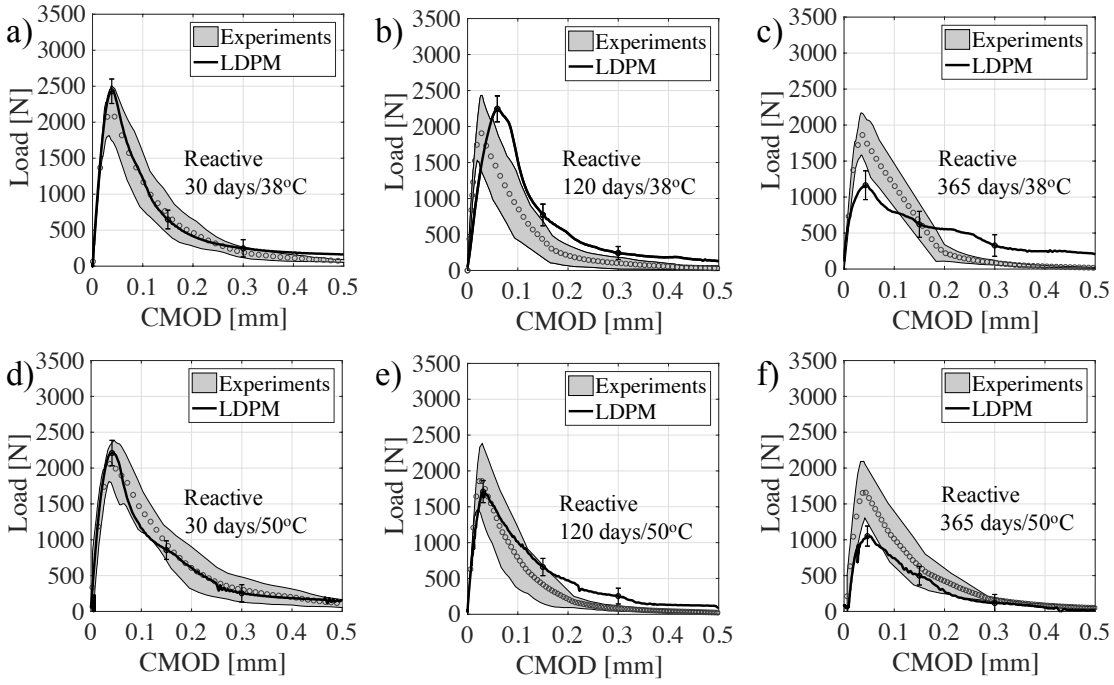

Figure 3.13. Results of 3 point bending test calibration in terms of load versus CMOD for reactive samples at the age of a) 30, b) 120 and c) 365 days at 38°C and d) 30 e) 120 and f) 365 days at 50°C.

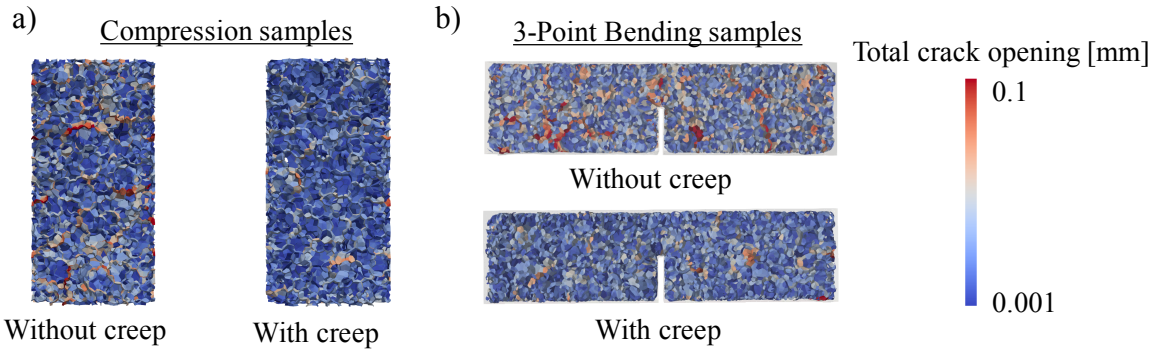

Figure 3.14. Crack contour comparison for a) Compression and b) 3 point bending test samples at 120 days 50°C with and without creep.

model shows that creep contributes to the redistribution of ASR damages leading to less distributed cracks and smaller maximal crack openings.

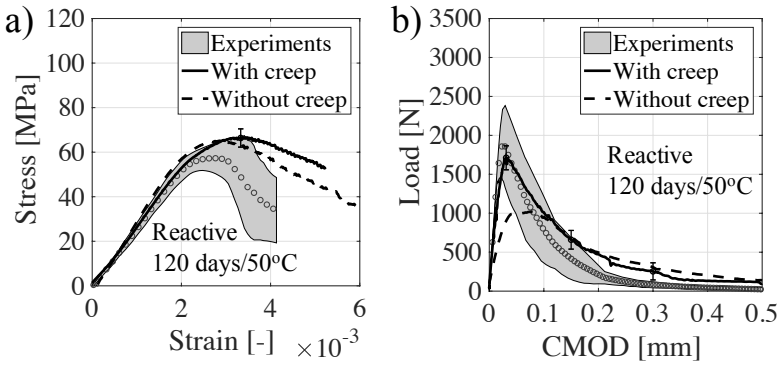

Figure 3.15. Comparison of a) Compression and b) 3 point bending test results at 120 days 50°C with and without creep.

Figure 3.15 presents the quantitative results of compression and 3 point bending test on ASR affected samples at the age of 120 days at 100% RH, 50°C respectively in terms of stress versus strain and load versus CMOD. The 3 point bending test results given on Figure 3.15b, show that the coupling of creep and ASR is necessary to accurately predict the experimental results and achieve realistic modeling. Also, as explained above, the crack contour results display more damages in the concrete samples when creep is not activated leading to a weaker material and a peak load 20% lower in the case of the 3 point bending test. It is worth mentioning that in compression, the crack distribution prior to concrete loading does not affect the results much as most of these cracks are being closed during the loading phase of the compression test. In tension (i.e. 3 point bending test), where tensile properties are more solicited, the crack distribution prior to loading matters more as crack localization is more susceptible to take place. In the 3 point bending test, as opposed to the compression test, the supports providing the reaction force are not facing the loading zone, hence, the cracks will not close during the loading phase this means that any initiated crack located above the notch constitute an opportunity for damage

localization which results in a much lower strength. The presented results demonstrate the superior capability of the model to not only predict accurately the strength loss due to ASR by mean of a realistic coupling between the ASR and creep model. The M-LDPM successfully capture ASR mitigation through creep in addition to providing its user with realistic crack patterns demonstrating how can creep help reduce ASR damages.

3.4. Concluding remarks

The M-LDPM successfully models concrete strength build up due to aging which translate into an increase of the mechanical properties (ie. compressive strength, tensile strength, fracture energy). Also higher temperature is associated with a higher aging rate and lower asymptotic strength. The numerical model captures also temperature effects on the longitudinal expansion due to both thermal and ASR expansions very well. Higher temperature led to a higher initial expansion rate in the presence of ASR but to a lower asymptotic expansion. As far as ASR impact on concrete mechanical properties, the experimental results suggested that ASR has more impact in tension which is simulated accurately with the LDPM (ie. 3 point bending and Brazilian tests). Significant damages are still observable in compression although they remains smaller than in tension.

Last but not least, M-LDPM ASR damages predictions are excellent when the creep and ASR models are coupled. Creep inhibits the cracks formation due to ASR and reduces damage localization. The mitigation of ASR damages is essential to properly simulate concrete tensile properties and their evolution in time under ASR. With the combination of the aging, creep and ASR models, the M-LDPM can capture concrete

aging (strengthening) as well as ASR impact on concrete strength degradation. Indeed, to estimate damages caused by ASR at a given age, one should look at the difference in strengths between two samples of the same age with one non reactive (subjected to aging only) and the other one reactive (subjected to aging and ASR). Failing to do so, one would underestimate by much ASR damages on concrete strength evolution. The proper combination of the different models in the M-LDPM are specifically what allows for superior modeling and predictive capabilities of concrete mechanical properties and their evolution.

CHAPTER 4

Full Coupling Between Diffusion and Mechanical Analysis in a Discrete Model

4.1. Introduction

Many concrete structures suffer from high relative humidity environments which are the source of multiple deterioration mechanisms such as corrosion, chloride and sulfate attacks, Alkali-Silica reaction and freeze/thaw cycles. For materials such as concrete, moisture is a double edged sword. Water plays a major role when it comes to concrete cement hydration [**13, 44, 37**]. This vital mechanism to concrete early age strengthening [**57, 58, 82**] also participate to cracks prevention in reinforced concrete structures [**67**]. However, failure of concrete leads to the presentation of fractures. Well known in the field of structural engineering and infrastructure materials, fractures behave like hydraulic conductors which increase significantly permeability and happen to be easy pathways for water reach and corrode [**53**] the reinforcements. As corrosion progresses, the integrity of reinforced concrete structures becomes debatable and developing coupled models that can characterize fracture-flow behavior in cementitious materials is essential to accurately assess the durability of such structures [**59, 71, 75**].

Friedrich-Karl Benra et al. [**12**] and A. Villani [**74**] developed continuous models that simulate the interactions between fluid and structure based on the classical Navier-stokes equation for the fluid flow modeling. Based on a continuous approach, these models

simulate material deformations but cannot model crack initiation nor propagation. Such models are not suitable for fracture-flow analyses in concrete structures as crack effect needs to be a feature of the model for better accuracy of the analysis.

Peter Grassl [**30**] proposed a hybrid discrete continuum modeling of fracture-flow in concrete. The present work describes recent developments of a discrete model for coupled fracture- flow analyses of cementitious materials. The Lattice Discrete Particle Model (LDPM) mesostructure is used to construct the edges (the elements of the ow lattice) which are along the triangular facets of the mesostructure, where the polyhedral cells are in contact. This creates a dual lattice model, fracture analyses are performed on the structural lattice, whereas flow analyses are performed on the flow lattice. In order to couple the fracture and flow analyses, the amount of crack opening of each structural element which exhibiting fracture, is used to evaluate the permeability increase of the surrounding flow lattice elements, in accordance with theory or experimental observations. The capabilities of this model are demonstrated by simulating experimental data relevant to water diffusion in cracked concrete. For example, the Lattice Discrete Particle Model (LDPM), a three-dimensional meso-scale discrete model, was developed by Dr. Cusatis et al. to simulate the mechanical behavior of concrete at the mesostructural level. LDPM is capable of characterizing strain localization, distributed cracking in tension and compression, and to reproduce well post-peak softening behavior. However, in classical complex engineering cases, one-way approaches can be limiting to accurately describe phenomena such as the interaction between fluid and structure, which actually plays a major role when it comes to durability. One alternative to successfully characterize and model the mechanics and moisture diffusion is to adopt the two-way coupling. This approach shows

great potential for multi-physics applications where mechanical and diffusion equations cannot be solved independently. For example, in concrete constructions, crack formation is a common occurrence, which allows for water ingress and transport of multiple aggressive chemical compounds. This greatly affects the strength of reinforced concrete structures as water, carbon dioxide and other chemicals penetrate to reach and corrode the steel reinforcement. Due to the flexibility of extended LDPM framework, two way-coupling analysis between diffusion and mechanics can successfully be performed. The two-way coupling requires edge elements in the diffusion problem. In the diffusion domain, each edge element can access information from its adjacent LDPM facets, such as crack opening. The solution process of the two-way coupling is similar to the one-way coupling. The only difference is that, whenever diffusion is being solved, first update the diffusion problem using the information from the mechanical process, which is done at the element level.

4.2. Experimental Protocol

The purpose of the experiment is to explore the effect of cracking and the self-healing agent Penetron on concrete permeability under a controlled drying environment. The adopted approach in this section for the experimental set up was inspired by the presented work in Ëffect of Cracking on Drying Permeability and Diffusivity of Concrete ẅhere reinforced C-shaped beams specimens are deformed by a tie rod on the tensile face to produce evenly distributed cracks. In this study, the effects of cracks and the self healing agents are first analyzed separately and then together. The experimental results will provide the reader with an appreciation of cracking effects on concrete permeability as well as Penetron self healing capacity to counter act cracking effects.

4.2.1. Self-Healing admixture: Penetron

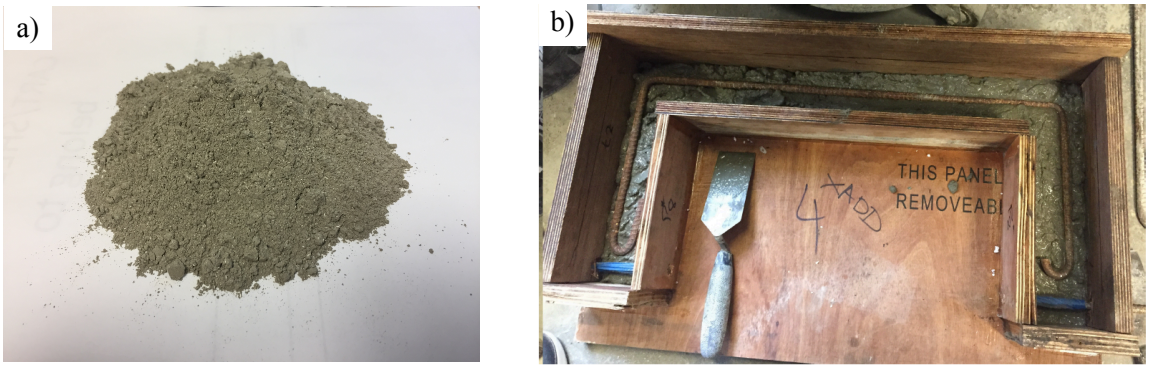

Figure 4.1. a) Penetron admixture b) Reinforcement placement in C-shaped samples

Studies such as [**60**] have recently explored the possible advantages associated with a self healing admixture added into concrete mixes. Their advantage lays in the fact that

reinforced concrete can directly be damage by water ingress that is capable of corroding and to significantly reduce the strength of of the internal steel skeleton. Although the reinforcements strength loss can be assumed to be a function of the level of oxidation, concrete structures have seen their durability reduced of 40 years due to natural corrosion only [**73**]. This concern has motivated scientists to develop new methods including self healing concrete development to avoid structures failure due to deterioration mechanisms (i.e. corrosion or even Alkali-Silica Reaction (ASR)). Penetron integral concrete capillary waterproofing system has been used for more than 30 years to waterproof worldwide concrete structures.

Penetron admix is a non toxic cementitious admixture and is largely used in projects involving potable water. This chemical has the particularity to assist in the hydration process acting as a catalyst to unhydrated cement particles. 1% OF Penetron Admix is used by weight of cement at the time of batching. The activating chemical reacts with water, calcium hydroxide and aluminum naturally present to build a web of insoluble crystals. The ladder fills the capillarities acting as a sealing. The sealant crystals have the capacity to seal to fill up voids up to 0.4 mm and prevent any water to penetrate where Penetron Admix has reacted. The advantages associated with Penetron Admix are numerous:

1) Concrete strengthening in compression and tension

2) No internal stresses due to vapor pressure as air is still allowed to pass through the crystalline formations

3) Waterproofing feature

4) Permanent benefits

Initial research findings on Penetron have demonstrated that the crystal production is related to the amount of moisture available for Penetron admix to react. The self healing features of Penetron are convenient for concrete protection as moisture can actually harm reinforcements' strength of concrete structures. However, in presence of Penetron this moisture can actually be used to improve the material density.

4.2.2. Samples preparation

A total of twelve C-shaped beams samples were prepared for testing. Additionally, six 75 mm x 150 mm (radius x diameter) cylinders and 75 mm x 75 mm x 280 mm notched beams specimens were prepared to characterize the mechanical properties of the casted concrete. Table 4.1 summarizes the samples repartition for this experimental campaign.

Table 4.1. Sample batches description

	# Samples	**Rebars**	**Load**	**Self-Healing**
Batch A	3	No	No	No
Batch B	3	No	No	Yes
Batch C	3	Yes	Yes	No
Batch D	3	Yes	Yes	Yes

Concrete is known to be strong in compression but relatively weak in tension. Indeed, concrete tensile capacity can reach less than a tenth of its compressive strength. One way to contain cracks generated due to tension and to avoid damage localization is to reinforce concrete with steel in the tension area. This method was here used to obtain uniformly distributed cracks on the lower face of the C-shaped samples. Naturally, the

samples that were meant to be cracked only were reinforced. For this purpose, two sizes of rebars were here used to prepare the reinforced samples: No 3 (6.4 mm diameter) with a yielding strength of 500 GPa covered in 12.7 mm of concrete. An ordinary rebar bender was used to achieve the reinforcement design presented in Figure 4.1. Stirrups were also introduced into the side arms or each C-Shaped beam to strengthen the loaded zone and avoid any unwanted failure.

To ensure that the components of concrete are combined into a homogeneous mixture, the dry elements are first mixed together in the electric concrete mixer which is covered with a plastic film to avoid cement particles loss due to the circular motion. Then the water is poured to bind the homogeneous dry mix. The followed mix design is presented in Table 4.2.

Table 4.2. Concrete mix design

Material	**Cement**	**Water**	**Aggregates**			**Sand**
			4.75-9 mm	9-12.5 mm	12.5-19 mm	
Proportions	1	0.5	1	0.5	0.5	2

In preparation of the loading phase, plastic tubes were casted inside the concrete arms to allow for the threaded bar to go through and set up the loading system. The freshly casted concrete samples were disposed with wet burlaps on top for 24 hours prior to de-molding. Once removed from the molds, the C-shaped beams are cured for 28 days at 100% RH 23°.

The loading system consisted in a high strength tie rod of 11 mm diameter. Hollowed steel disks of 30 mm diameters were placed on both end of the tie rod to distribute the

load on the external faces of the lateral arms. The load was applied by generating an inward displacement of the lateral arms of the C-shaped beam by screwing nuts on the ends. A multi gage length comparator was used to control the tie rod elongation, in other words the horizontal force applied on the sample arms. The samples were loaded up to 15 kN which on the long term led to the tie rod deformation due to creep. To prevent this phenomena from altering the applied force and hence the crack opening, the tie rod was replaced periodically. The later was replaced at age 1 month, 2 months and 4 months. As the sample was sustaining the load for a longer time, its plastic deformation was leading to less force in the tie rod, as a result, after 4 months, the load applied was checked every month and adjusted when necessary to maintain the crack opening constant.

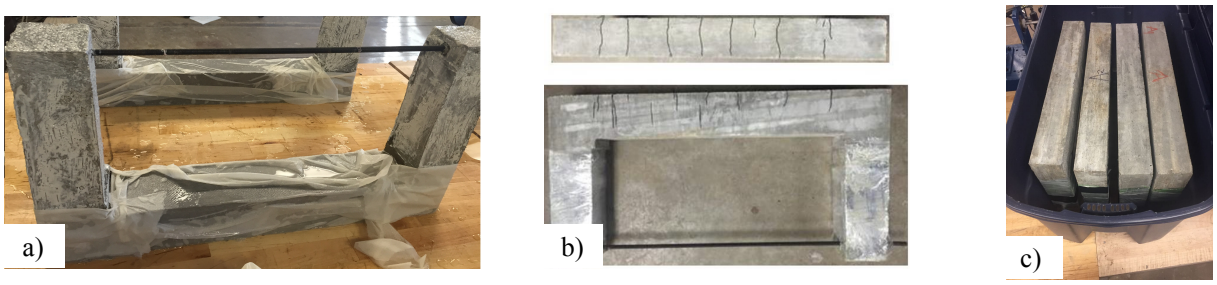

Figure 4.2. Results comparison in terms of Relative weight loss versus Time for the a) Intact and cracked beams, b) Intact beams with and without Penetron Admix and c) Cracked beams with and without Penetron Admix. Results comparison in terms of Relative weight loss versus logarithm of the time for the d) Intact and cracked beams, e) Intact beams with and without Penetron Admix and f) Cracked beams with and without Penetron Admix.

The surface of the sample in tension is relatively small in comparison to the other undamaged surfaces. One solution to overcome this problem is to seal the lateral arms, this way, the moisture loss happens principally through that cracked face which enhances

the observation of crack effects. The sealant used was a mix of high strength epoxy to additionally reinforce the lateral arms with paraffin oil, known to be a great sealant. The beams were sealed loaded and sealed at day 26 of curing to allow for the sample to resaturate due to potential early drying during the loading process.

After 28 days, the C-shaped samples are placed in a controlled drying environment at 23°C and 55% RH. The control of the RH is achieved by using saturated salt solutions. Plastic boxes with a capacity of hosting 3 C-shaped beams each are filled up to 5 mm with water after what the magnesium nitrate is added in excess to maintain the relative humidity equilibrium at 55%. RH and temperature Sensirion sensors were used to get direct readings of the ambient conditions of the samples.
As the saturated concrete samples (100% RH) are placed in the box set at a lower RH (100% vs 50%), the C-shaped beams start losing water by evaporation on from the middle section of the samples. The rate of water evaporation is linked to the permeability of the material and can be estimated by measuring the relative weight loss over time. The ladder corresponds to the mass of water lost over time due to drying.

4.3. Results and Discussion

As shown on Figure 4.2 b the loaded samples display evenly distributed cracks as expected. The crack openings were measured thanks to a crack opening ruler by visual estimation. The results relevant to the C-shaped beams weight loss are presented in 4.3. Each curve is the average of the results of 3 specimens.

Figure 4.3 a) and d) respectively show the results of the relative water loss versus time and logarithm of time for the intact and cracked samples. One can observe that at early stages of drying, a noticeable difference in terms of water loss is seen. Naturally, the cracked C-shaped samples show a faster drying which translates into a more important water loss. The samples with cracks display and increase of 66% of their moisture loss in comparison to the intact samples.

Figure 4.3 b) and e) respectively show the results of the relative water loss versus time and logarithm of time for the self healing and non self healing samples. In this particular case, the results suggest that the self healing additive allows a slight recovery/improvement of the permeability of less than 7% in terms of relative weight loss. Such a small recovery can be justified by the fact that at this stage the intact samples are subjected to shrinkage and as a results display micro-cracks that can slightly affect the measured relative weight loss. This observation also emphasizes on the efficiency of Penetron admix to reduce shrinkage damages by either strengthening of the material or actual self healing of the generated micro-cracks. Further investigation on Penetron Admix would allow to determine whether this recovery in terms of water loss is due to concrete strengthening thanks to Penetron or whether shrinkage damages occur and are afterwards healed by self healing mechanism.

Figure 4.3 c) and f) respectively show the results of the relative water loss versus time and logarithm of time for the self healing and non self healing cracked samples. In the presence of cracks, one can appreciate the significant contribution of the self-healing additive. Its capacity to reduce drying by counteracting cracks effects on permeability takes place within the first 100 hours as suggested by the results. Indeed, initially (time=0),

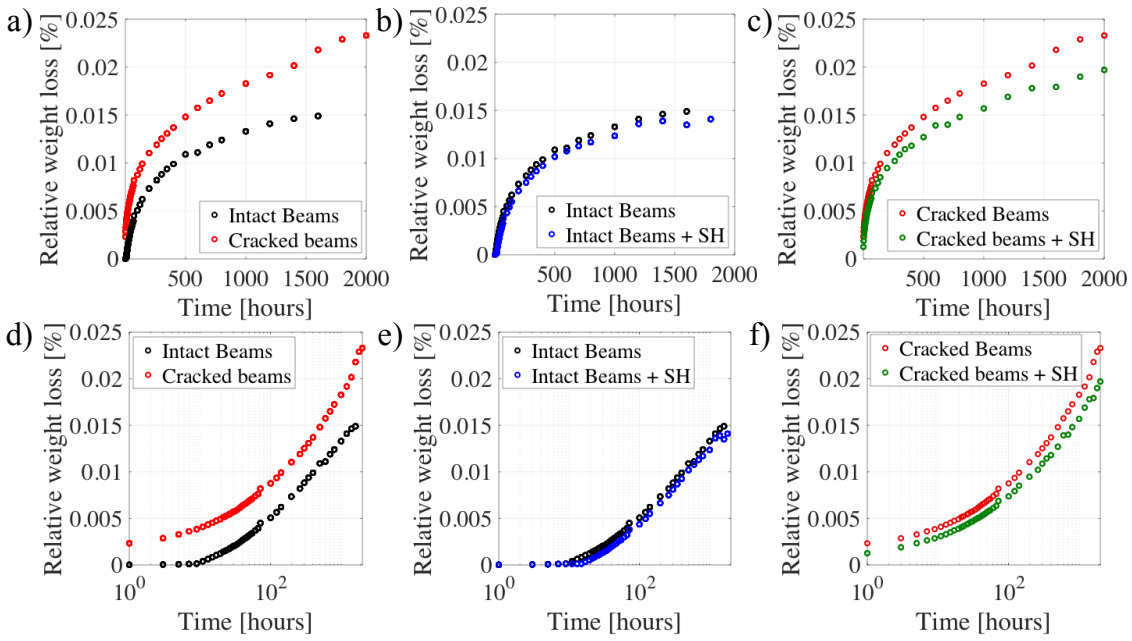

Figure 4.3. Results comparison in terms of Relative weight loss versus Time for the a) Intact and cracked beams, b) Intact beams with and without Penetron Admix and c) Cracked beams with and without Penetron Admix. Results comparison in terms of Relative weight loss versus logarithm of the time for the d) Intact and cracked beams, e) Intact beams with and without Penetron Admix and f) Cracked beams with and without Penetron Admix.

the C-shaped samples are in saturated conditions (100%RH) and the excess of water available reacts with the self healing admixture and increase the crystals productions in the empty pores of concrete. This chemical reaction as explained in [], results in water proofing features that decreases the moisture evaporation rate. Penetron admix allowed for a recovery of approximately 33% in terms of relative water loss. The comparison of the results in Figure 4.3 a), c), d) and f) suggest that Penetron admix reduces by half cracks effects on concrete permeability in the surroundings of this experimental program.

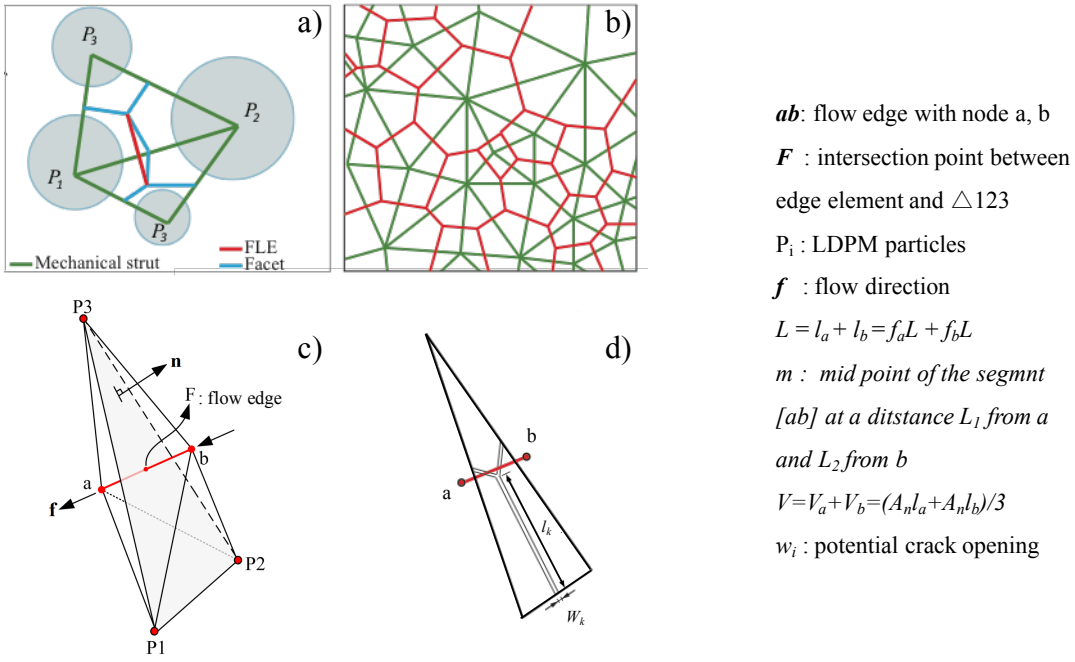

Figure 4.4. (a) Generation of a Flow Lattice Element (FLE) connect the tetpoints belonging to two adjacent tetrahedra in 2D domain. (b) 2D representation of a FLE network for simulating ow along the material domain and the dual lattice system. (c) Generation of a Flow Lattice Element (FLE) connect the tetpoints 3D domain. (d) the cracked triangle face and the illustration of normal crack opening

4.4. Two way coupling model formulation

4.4.1. Two Way Coupling Topology

Concrete is known to have a granular structure because its main component are aggregates. As finer elements such as cement, sand and water are mixed together with the larger aggregates, a cementitious matrix forms and binds the agglomerated aggregates to build concrete. From a modeling perspective, this granular structure can be accurately replicated and used as a foundation for the subsequent modeling of any physical phenomena. Typically, concrete aggregates size vary from 2 to 20 mm diameter. LDPM is

capable of replicating the aggregate size heterogeneity in concrete through a discretization of the material volume into a granular lattice system of randomly distributed aggregates represented as polyhedral cells. For finer material, coarse graining approximation have given excellent results [**18**], but in this thesis the LDPM is used model concrete internal granular structure by explicitly modeling aggregates and their relative interactions.

To build a 3D diffusion network in concrete, 1D transport lattices initially generated by the LDPM are here used as direction vectors for the fluid flow. The LDPM cell system provides a geometrical characterization of the concrete solid portion and is used for the description of the mechanical behavior at mesoscopic scale. Based on this internal modeled structure, a 3D diffusion network is build to model fluid flow at the mesoscopic scale as well.

Figure 4.4 presents a tetrahedron generated in the Delaunay tetrahedralization based on the mesh generation described in the and shown in Figure 4.5a. Figure 4.4 provides a 2d representation of the ladder. The 1D flow lattice elements establish the direct connection between points inside two adjacent tetrahedra also vertices of the corresponding polyhedral cells. Figures 4.4 provides a 2D and 3D representation of the flow lattice elements. Each tetrahedron communicates with four other tetrahedrons creating a total of 5 interconnected tetrahedrons with transport lattices where the fluid flow occurs. It should be underlined that this moisture flow lattice system gives a realistic flow of moisture as the ladder mostly occurs where concrete cracks, in other words at the aggregate interface. Similarly, the fluid transport occurs between tetrahedra across the entire modeled concrete volume. Figure 4.5a illustrates the external cells of the mechanical lattice and

the transport network associated with it. Last but not least, the isothermal mass transfer from a drying porous surface across a constant air has been extensively and modeled through a boundary layer that includes the effect of advection and diffusion. The ladder allows for a modeling of the diffusional behavior that is realistic with comparison to the actual happening diffusion phenomena. The boundarry layer is modeled through a thin layer of elements orthogonal to the concrete external surface where the boundary conditions are applied.

By interacting with the mechanical lattice, the transport lattice can be used to simulate a coupled fluid flow associated with a certain deformation and cracking. The described model has shown superior capability in simulating similar mechanical and diffusional (moisture and heat) behaviors for material with similar internal structures such as rocks, mortar or limestones.

4.4.2. Fluid flow through uncracked material

On the one hand, the fluid flow across the uncracked portion of the material is modeled with the Hygro-Thermo Chemical model. As the uncracked material represents more than 95 percent of the tet face area, precise and reliable modeling of the fluid and temperature transport and distribution within the material internal structure becomes essential. As needed, the model is capable of accurately provide the fields of Temperature T, relative humidity h and cement hydration degree α_c spatially and temporally based on material paramters and simulation boundary conditions.

Based on a Fick's law, the moisture transport under isothermal conditions can be written as $\mathbf{J} = -D_h(h,T)\boldsymbol{\nabla} h$ where $\mathbf{J}$ is the flux of water mass per unit time and the

moisture permeability has the following functional form $D_h(h,T) = D_1[1 + (D_1/D_0 - 1)(1-h)^n]^{-1} \exp(E_{ad}/(RT_0) - E_{ad}/(RT))$. D_0, D_1 and n are material parameters, whereas T_0 is the reference room temperature, E_{ad} is the diffusivity activation energy and R is the universal gas constant. By writing the mass balance per unit volume of mortar, i.e. equating the rate of water content w to the divergence of the flux of water mass per unit time $\mathbf{J}$, and considering that the water content is divided in evaporable w_e and non-evaporable w_n water: $w = w_e + w_n$, on can obtain:

$$\boldsymbol{\nabla}\cdot(D_h \boldsymbol{\nabla} h) - \frac{\partial w_e}{\partial h}\frac{\partial h}{\partial t} - \frac{\partial w_e}{\partial \alpha_c}\dot{\alpha}_c - \dot{w}_n = 0 \tag{4.1}$$

The sorption/desorption isotherm defining the evaporable water as a function of relative humidity is introduced by distinguishing the evaporable water present in the C-S-H gel w_e^{gel} and in the capillary pores w_e^{cap}: $w_e = w_e^{gel} + w_e^{cap}$ through the following functional forms:

$$w_e^{gel} = k_{vg}^c \alpha_c c[1 - e^{-10(g_1 \alpha_c^\infty - \alpha_c)h}] \tag{4.2}$$

$$w_e^{cap} = \frac{w_0 - 0.188\alpha_c c - k_{vg}^c \alpha_c c[1 - e^{-10(g_1\alpha_c^\infty - \alpha_c)}]}{[e^{10(g_1\alpha_c^\infty - \alpha_c)} - 1][e^{10(g_1\alpha_c^\infty - \alpha_c)h} - 1]^{-1}} \tag{4.3}$$

where c is the cement content, w_0 is the initial water content, k_{vg}^c and g_1 are material parameters. One can note that at saturation, $h = 1$, thus $w_e = w_0 - 0.188\alpha_c c$. This expression is further used when the ASR model will be introduced.

Concerning energy conservation law, a Fourier's law is considered for the heat conduction $\mathbf{q} = -\lambda_T \boldsymbol{\nabla} T$ where $\mathbf{q}$ is the heat flux, and λ_T is the heat conductivity (defined for

$T < 100°\text{C}$). By considering the rate of heat of hydration reaction generated per unit volume $\dot{Q}_c$ as a linear function of the rate of the degree of hydration $\dot{\alpha_c}$, one can write the enthalpy balance equation as:

$$\boldsymbol{\nabla}\cdot(\lambda_T \boldsymbol{\nabla} T) - \rho c_T \frac{\partial T}{\partial t} + \dot{\alpha_c} c \tilde{Q}_c^{\infty} = 0 \tag{4.4}$$

where $\tilde{Q}_c^{\infty}$ is the latent heat of hydration reaction per unit of hydrated mass, assumed constant for a given mortar, ρ and c_T are respectively the density and the isobaric heat capacity of mortar.

For concrete mixes, the reaction of free water with unhydrated cement particles causes an early age chemical reaction of cement hydration. The hydrating particle generate Calcium-Silicate-Hydrates (CSH) which contribute significantly in strengthening and improving the stiffness of concrete. The hydration degree α_c is what characterizes cement hydration and represents the fraction of cement fully reacted with water. Its evolution over time can be described as follows:

$$\dot{\alpha_c} = \frac{A_{c1} e^{-\eta_c \alpha_c / \alpha_c^{\infty}} e^{-E/R(T-T_0)}}{1 + (55 - 5.5h)^4} \left(\frac{A_{c2}}{\alpha_c^{\infty}} + \alpha_c \right) (\alpha_c^{\infty} - \alpha_c) \tag{4.5}$$

where η_c, A_{c1} and A_{c2} are material parameters.
The validity of the equations described above is revocable for temperatures exceeding $90^o C$.

By considering two adjacent tetrahedra $p_a p_b p_c p_d$ and $p_a p_b p_c p_e$ and the triangle $p_a p_b p_c$ shared by both of them, one can notice that the connection between the tet-points T_a and T_b of each of those tetrahedra constitutes the flow lattice element that crosses the triangle $p_a p_b p_c$. The pyramidal sub-domains $p_a p_b p_c T_a$ and $p_a p_b p_c T_b$ are associated with the edge

element e_{ab}.V_a and V_b are respectively the volumes associated with the pyramids $p_a p_b p_c T_a$ and $p_a p_b p_c T_b$ and are computed as follows:

$$V_a = \frac{A_n f L_a}{3} \tag{4.6}$$

and

$$V_b = \frac{A_n f L_a}{3} \tag{4.7}$$

where A_n=$n^T f A$ is the projection of the original area A of face $p_a p_b p_c$ on the plan orthogonal to the flow lattice element. Also, n is the normal vector to the face $p_a p_b p_c$, $f_{a/b}$ is the fraction distance of L (distance between T_a and T_b such as L_a=$f_a L$ and L_b=$f_b L$. One can naturally define, L=$L_a + L_b$ and $f_a + f_b$=1. This same approach leads to similar equations in terms of volumes V_a=$f_a V$ and V_b=$f_b V$ where V represents the total volume of both pyramids $p_a p_b p_c T_a$ and $p_a p_b p_c T_b$, in other words V=$V_a + V_b$. For the subsequent discussion and derivation, the mass balance is considered for V_a and V_b.

A discrete approach was here followed for the governing equation formulation of the fluid flow to insure consistency between the mechanical and moisture transport formulations. By considering the volume V_a, M^a_{unc}, the fluid mass contained in the uncracked volume of V_a and Q^a_{unc} the fluid flux through the face $p_a p_b p_c$, one can write the mass balance as follows:

$$\dot{M}^a_{unc} = Q^a_{unc} \tag{4.8}$$

$\dot{M}^a_{unc}$ denotes the fluid mass rate in the volume V_a and includes the effect of the internal source term and can be expressed:

$$\dot{M}^a_{unc} = \dot{M}^b_{unc} = \frac{A_n L}{3}\left(\frac{\partial w_e}{\partial h}\frac{\partial h}{\partial t} - F_h\right) \tag{4.9}$$

where $-F_h$ is the water consumption [2].

The fluid flux through the a given volume V_a has been formulated, calibrated and validated in [**45**], where the Darcy's law is used to describe moisture diffusion. Hence, one can write:

$$Q^a_{unc} = A_n D^a_{unc}\frac{h_F - h_a}{L} \tag{4.10}$$

where D_h represents the local material permeability, h_F and h_a respectively the relative humidities at nodes F and a. Because of the element size, it is correct to approximate the relative humidity gradient by the finite difference of the ladder taken at the two nodes F and a. The same approach is adopted to obtain the flux Q^b_{unc} for the uncracked volume V_b:

$$Q^b_{unc} = A_n D^b_{unc}\frac{h_F - h_b}{L} \tag{4.11}$$

where similarly, h_b represents the relative humidity at the node b. By definition of the flux, the flux through V_a is equal to the flux coming out of the volume V_b. More generally

one can write:

$$Q^{ab}_{unc} = Q^{a}_{unc} = -Q^{b}_{unc} = A_n D_{eq} \frac{h_b - h_a}{L} \tag{4.12}$$

where

$$D_{eq} = \frac{f_a}{D^a_{unc}} + \frac{f_b}{D^b_{unc}} \tag{4.13}$$

The final governing equation can be written :

$$A_n D^a_{unc} \frac{h_F - h_a}{L} = \frac{A_n L}{3} \left(\frac{\partial w^a_e}{\partial h} \frac{\partial h_a}{\partial t} - F^a_h \right) \tag{4.14}$$

$$A_n D^b_{unc} \frac{h_F - h_b}{L} = \frac{A_n L}{3} \left(\frac{\partial w^b_e}{\partial h} \frac{\partial h_b}{\partial t} - F^b_h \right) \tag{4.15}$$

4.4.3. Fluid flow through cracked material

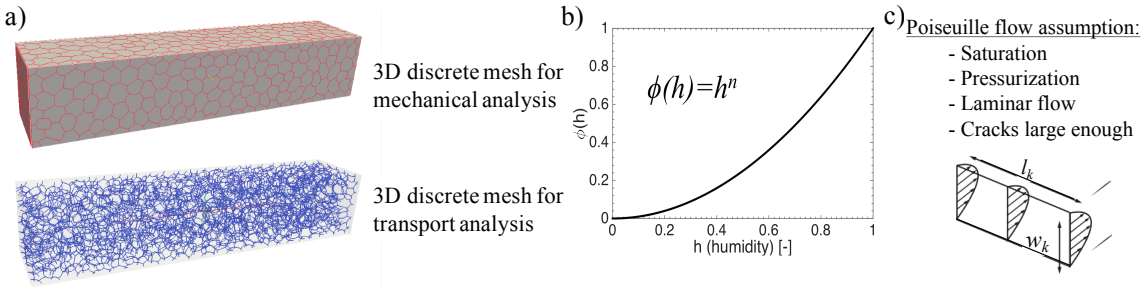

Figure 4.5. (a) 3D discrete meshes for mechanical and transport analysis (b) Power law representation of fluid estimation in crack versus relative humidity and (c) Poiseuille flow along the cracked surfaces.

Mass of water in the cracks. To include the effect of crack on the material permeability, the fluid mass contained in the cracks and its flux through the cracked surfaces are

introduced in the two way coupling mass balance equation formulation. By considering the edge elements E^{ab} and the six facets associated with it A^a_{f1}, A^a_{f2} , A^a_{f3}, A^b_{f1}, A^b_{f2} and A^b_{f3}. Respectively, the crack openings w^a_{N1}, w^a_{N2} and w^a_{N3} are associated with aperture of the facets A^a_{f1}, A^a_{f2} , A^a_{f3}. Similarly, the crack openings w^b_{N1}, w^b_{N2} and w^b_{N3} are associated with aperture of the facets A^b_{f1}, A^b_{f2} , A^b_{f3}. The fluid mass stored in the cracks can be written $M^a_{fc} = \rho_f V_c$, where the cracked volume can be expressed as follows: $v^a_c = \sum_{i=1}^{3} = A_{fi} w_{Ni}$. The direct coupling between the mechanical model and moisture transport model lays in the information of the local crack opening w_{Ni} of the i^th facet which is updated by the mechanical model. The total mass of fluid M_f stored in the volume V_a is computed by adding the one contained in the cracked material to the one contained in the crack material. Hence, it is correct to write:

$$M^a_f = M^a_{unc} + M^a_{crck} \tag{4.16}$$

One can write the derivative of total mass of fluid rate as follows:

$$\dot{M}^a_{cracked} = \frac{A_n L}{3}\left(\frac{\partial w_e}{\partial h}\frac{\partial h}{\partial t} + \frac{V^a_c}{V^a}\rho\frac{\partial \phi(h)}{\partial h}\frac{\partial h}{\partial t} + \rho\phi(h)\frac{\dot{V_c}^a}{V^a}\right) \tag{4.17}$$

Similarly for the volume V_b:

$$\dot{M}^b_{cracked} = \frac{A_n L}{3}\left(\frac{\partial w_e}{\partial h}\frac{\partial h}{\partial t} + \frac{V^b_c}{V^b}\frac{\partial \phi(h)}{\partial h}\frac{\partial h}{\partial t} + \rho\phi(h)\frac{\dot{V_c}^b}{V^b}\right) \tag{4.18}$$

The fluid flow through the cracked material is modeled using Poiseuille flow as depicted on Figure 4.5c. To establish the fluid mass balance in the crack per unit time (Q_c), a pressure p and crack of width w are considered. In this chapter, the single phase flow and full saturation conditions are assumed. As far as the fluid, the classical assumptions of laminar flow at any point and Newtonian fluid slightly compressible are supposed valid. More generally, the mass flux is a measurement of the amount of mass passing in or out of a control volume. The fluid flow rate through a control volume is then calculated by integrating the velocity field over the crossed surface S and expressed as follows:

(4.19)
$$\frac{A_n L}{3}\left(\frac{\partial w_e}{\partial h}\frac{\partial h}{\partial t}+\frac{V_c^a}{V^a}\rho\frac{\partial \phi(h)}{\partial h}\frac{\partial h}{\partial t}\right)=\frac{A_n}{L}D_{cracked}(h_m-h_a)-\frac{A_n L}{3}\left(F_h+\rho\phi(h)\frac{\dot{V_c}^a}{V^a}\right)$$

Similarly for the volume V_b:

(4.20)
$$\frac{A_n L}{3}\left(\frac{\partial w_e}{\partial h}\frac{\partial h}{\partial t}+\frac{V_c^b}{V^b}\rho\frac{\partial \phi(h)}{\partial h}\frac{\partial h}{\partial t}\right)=-\frac{A_n}{L}D_{cracked}(h_m-h_b)-\frac{A_n L}{3}\left(F_h+\rho\phi(h)\frac{\dot{V_c}^b}{V^b}\right)$$

where $I_c^a \sum_{k=1}^{3} l_k^a w_k^3$ and $I_c^b = \sum_{k=1}^{3} l_k^b w_k^3$.

By considering the mass balance, one can express the equivalent permeability D_h and D_T.

(4.21)
$$D_H\frac{(h_b-h_a)}{L}=-D_H^b\frac{(h_b-h_m)}{L_b}$$

(4.22)
$$D_T\frac{(T_b-T_a)}{L}=D_T^a\frac{(T_m-T_a)}{L_a}$$

where $D^{a/b}_{Hcracked} = D_h + \frac{\rho P_{sat} I_c^{a/b}}{12\mu}$ $D^{a/b}_{Tcracked} = \frac{\rho h_{a/b} I_c^{a/b}}{12\mu} \frac{P_{sat}}{dT}$.

Implementation

The new mass conservation law is coupled with the energy conservation law Equation 4.4 and can be written as follows:

$$M^* \frac{A_n L}{3} \mathbf{B}_f \dot{\mathbf{h}} + D_h^* \frac{A_n}{L} \mathbf{B}\mathbf{h} + D_T^* \frac{A_n}{L} \mathbf{B}\mathbf{T} = S^* \frac{A_n L}{3} \mathbf{f} \tag{4.23}$$

Where, the mass matrix is:

$$M^* = 2\frac{\partial w_e}{\partial h} + \rho \frac{\partial \phi(h)}{\partial h} \left(\frac{V_c^a}{V^b} + \frac{V_c^b}{V^b} \right) \tag{4.24}$$

the source matrix is defined by:

$$S^* = -2F_h - \rho\phi(h) \left(\frac{\dot{V_c}^a}{V^a} + \frac{\dot{V_c}^b}{V^b} \right) \tag{4.25}$$

The humidity permeability matrix is given by:

$$D_h^* = \frac{1}{\frac{f_a}{D_h + \frac{\rho P_{sat} I_c^a}{12\mu}} + \frac{f_b}{D_h + \frac{\rho P_{sat} I_c^b}{12\mu}}} \tag{4.26}$$

Similarly the thermal permeability matrix is defined as follows:

$$D_T^* = \frac{1}{\frac{f_a}{\frac{\rho h_a I_c^a}{12\mu} \frac{P_{sat}}{dT}} + \frac{f_b}{\frac{\rho h_b I_c^b}{12\mu} \frac{P_{sat}}{dT}}} \tag{4.27}$$

The humidity vector

$$\mathbf{h} = \begin{bmatrix} h_a \\ \\ h_b \end{bmatrix} \tag{4.28}$$

The humidity rate vector

$$\dot{\mathbf{h}} = \begin{bmatrix} \dot{h_a} \\ \dot{h_b} \end{bmatrix} \tag{4.29}$$

The Temperature vector

$$\mathbf{T} = \begin{bmatrix} T_a \\ T_b \end{bmatrix} \tag{4.30}$$

The fraction vector

$$\mathbf{f} = \begin{bmatrix} f_a \\ f_b \end{bmatrix} \tag{4.31}$$

The $\mathbf{B}$ matrix

$$\mathbf{B} = \begin{bmatrix} 1 & -1 \\ -1 & 1 \end{bmatrix} \tag{4.32}$$

The $\mathbf{B}_f$ matrix

$$\mathbf{B}_f = \begin{bmatrix} f_a & 0 \\ 0 & f_b \end{bmatrix} \tag{4.33}$$

The source terms are averaged over the volumes V_a and V_b for the purpose of simplifying the implementation. Crank-Nicolson algorithm method is here used to obtain the numerical solution of fluid flow governing equations. The mass balance at the edge element scale

is reiterated for each edge element of the entire mesh constituting a representative global response to the given flow problem.

Depending on the aperture of the crack, fluids can be found there under three different states: solid, liquid or gas. Estimating accurately the portion of each water state in a crack is challenging as few resources are available on the topic. In this paper, the mass of water is calculated through a power law function of the relative humidity as follows:

$$m_c = k_\rho \rho_w A_c h^n \tag{4.34}$$

$m_c = \rho\phi(h)V_c$ and $h = \frac{p}{p_{sat}}$

where A_c is the edge area of cracked material; ρ_w represents the fluid density; k_ρ and n are parameters to calibrate. Figure 4.5b displays a plot of power law function ($n = 2$) versus the relative humidity h. As expected, if the relative humidity is equal to zero, the mass of water available in the crack will be equal to zero as well. While, if the relative humidity is equal to one, the mass of water in the crack will be maximum as well. The relative humidity is implemented a function of the pressure p as follows:

$$h = \frac{p}{p_{sat}(T)} \tag{4.35}$$

$$p_{sat}(T) = \exp\left(20.438 - \frac{5044}{T + 273.15}\right) \tag{4.36}$$

where p_{sat} represents the pressure at saturation and T is the temperature in Kelvins.

4.4.4. Model verification

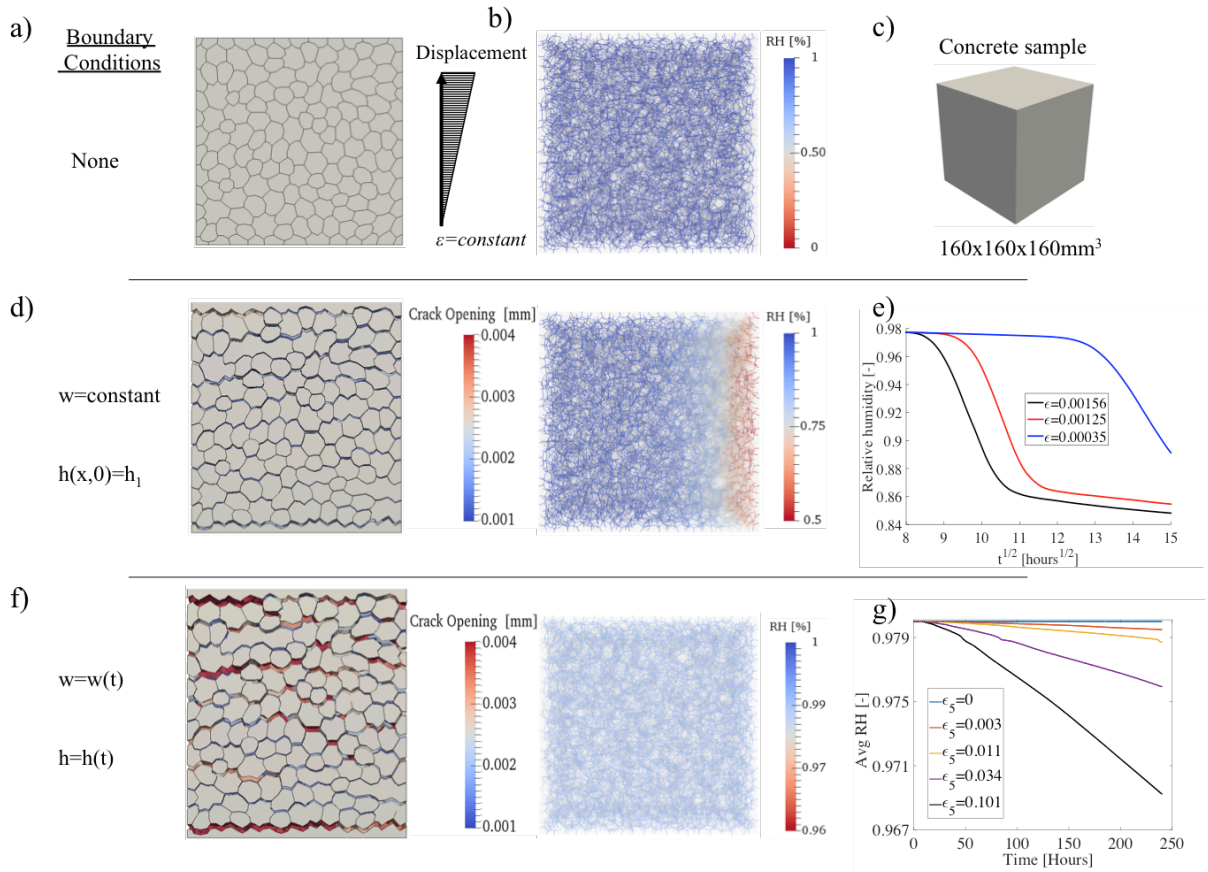

Figure 4.6. a) LDPM mesh. b) Transport lattice mesh. c) Sample geometry. d) Velocity and relative humidity profile for cracked concrete samples drying on one face. e) Plot of relative humidity versus the square root of time for 3 samples submitted to 3 constant strains and drying on one face at 50 percent relative humidity. d) Velocity and relative humidity profile for sealed cracked concrete samples. f) Plot of relative humidity versus the square root of time for 3 samples submitted to 5 constant strains under sealed conditions.

Verification 1 : Crack effect on permeability.

Some preliminary results reported in Figure 4.6 demonstrate the capability of the two way coupling to capture efficiently the effect of cracks on humidity and temperature

diffusion. The performed work consists of the simulation of a 160x160x160 mm^3 cube specimen where the diffusion parameter D_h used in equation 3 is set to zero to isolate the effect of cracks on drying. As far as boundary conditions, one lateral surface of the cube was exposed to a 50% relative humidity and the other sides were sealed to generate a uniaxial moisture diffusion. To generate horizontal cracks, the specimens were submitted to a constant vertical strain prior to drying. Three cases were considered involving the application of three different vertical strains on the specimen. As shown on Figure 4.6 after cracking, the moisture permeability increases significantly. The results show that for smaller strains (smaller cracks) the drying process is slower than for larger strains which is consistent with what was expected. The sensitivity study on the parameters that are to be calibrated is still ongoing and further results will be presented in the next progress report.

Verification 2 : Volume change effect on relative humidity. The third verification consisted in qualitatively evaluating the relative humidity evolution in a sealed concrete sample subjected to different levels of cracking. Generating cracks in the sample was achieve by applying a linear displacement (constant strain) on one face of the cubic sample. The relative humidity profile and plot of of relative humidity versus $t^{1/2}$ suggest that cracking induces a drop of the average relative humidity in the sample. This result is expected as by increasing the volume, the pressure within this given volume decreases automatically in sealed conditions. Also, equation 8 expresses the linear relationship between the relative humidity and pressure which explains how the model captures the relative humidity sensitivity to volume change (cracking).

Table 4.3. Mortar mix design.

Cement (kg/m^3)	Sand (kg/m^3)	Water (kg/m^3)	W/C
500	1650	300	0.6

4.4.5. Model Validation

The two way coupling framework is validated through experimental results demonstrating of crack effects on concrete permeability. Zhang et Al [**81**] used neutron imaging to successfully study the process of water penetration into cracked steel reinforced concrete. Neutron radiography is an effective method to qualitatively appreciate the process of water penetration into cracked and uncracked concrete. The 100 x 100 x 300 mm^3 mortar samples were prepared according to Table 4.4.5 and reinforced with 8 mm diameter stirrups. The cracked samples were prepared by 3 point bending loading to generate a single crack. The samples are cured for 14 days prior to the 4 days in the oven drying phase. Once the samples are completely dried, the lateral surfaces are sealed with silicon to impose 1D (vertical) moisture diffusion. Once ready, the samples are placed in an aluminum tray filled with water in contact with the lower face of the concrete sample. The top face is exposed to air as depicted on Figures 4.7b 4.8b at 50% RH. At this point the water travels through the crack and diffuses upward.

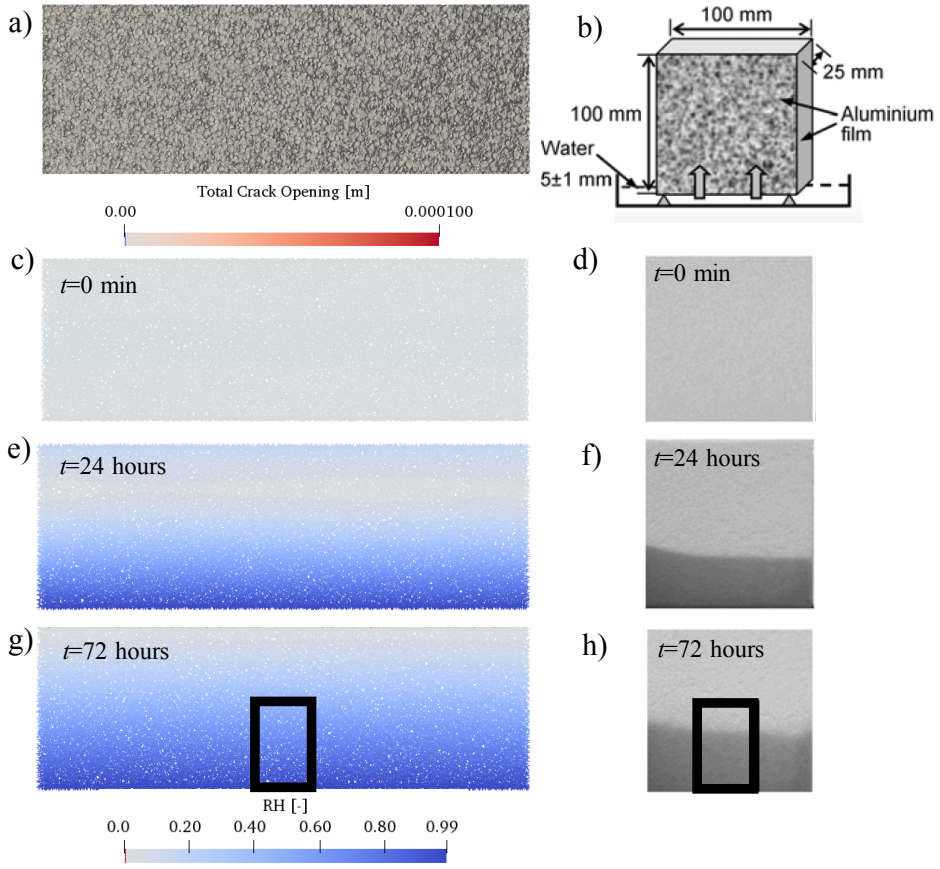

Figure 4.7. a) Uncracked concrete sample mechanical modeling. b) Uncracked concrete samples saturation experimental conditions. Modeled and Experimental observed relative humidity profiles in uncracked concrete samples at c) t_{LDPM}=0 hours d) t_{exp}=0 hours e) t_{LDPM}=24 hours f) t_{exp}=24 hours g) t_{LDPM}=72 hours and h) t_{exp}=72 hours.

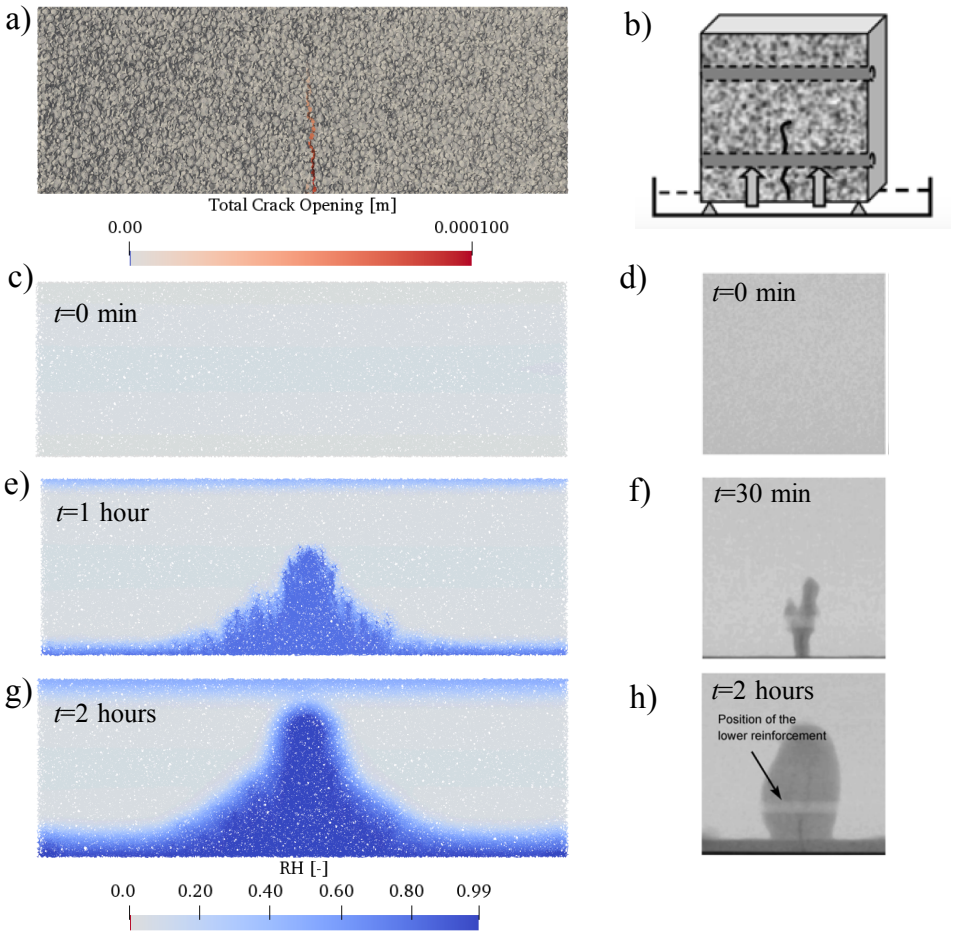

Figure 4.8. a) Cracked concrete sample mechanical modeling. b) Cracked concrete samples saturation experimental conditions. Modeled and Experimental observed relative humidity profiles in cracked concrete samples at c) t_{LDPM}=0 hours d) t_{exp}=0 hours e) t_{LDPM}=24 hours f) t_{exp}=24 hours g) t_{LDPM}=72 hours and h) t_{exp}=72 hours.

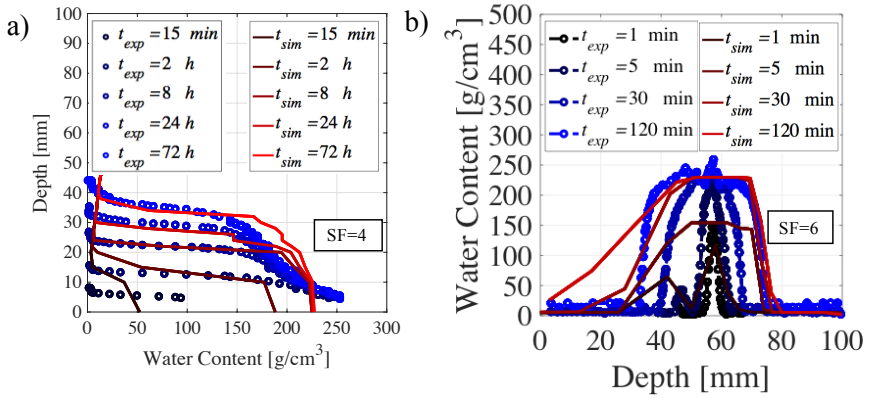

Figure 4.9. Numerical calibrations results of the resaturation process in the case of a) Uncracked and a) Cracked concrete samples respectively in terms of depth versus water content and water content versus depth.

Figure 4.7 presents the experimental set up for water sorption as well as a qualitative comparison of the LDPM and experimental results. As expected at 0 hours the samples are completely dry as shown on Figure 4.7 c) and d). With time, water penetrates upward which increases locally the water as depicted on Figures 4.7 e) and f) at 24 hours and g) and h) at 72 hours. Quantitatively, the water content evolution in the uncracked concrete sample is presented in Figure 4.9 a). To simulate the water content, the quantity w_e of the HTC model was considered as it describes the evaporable water present in the sample.The model calibration was performed by fixing the permeability parameters D_0, D_1 and n. The LDPM results are in good agreement with the experimental results and show the model superior capability in modeling water penetration of dried concrete samples. The rate of water absorbtion is indeed directly related to the cited parameters as they govern concrete.

Figure 4.8 presents the experimental set up for water sorption as well as a qualitative comparison of the LDPM and experimental results. As expected at 0 hours the samples

are completely dry as shown on Figure 4.8 c) and d). With time, water penetrates upward which increases locally the water as depicted on Figures 4.8 e) and f) at 15 minutes and g) and h) at 2 hours. Quantitatively, the water content evolution in the cracked concrete sample is presented in Figure 4.8 b). To simulate the water content, the same quantity w_e of the HTC model was considered in addition to the water found in the cracked described in equation 3.14.The model calibration was performed by maintaining the previously identified permeability parameters D_0, D_1 and n and fixing the crack effect through k_C. The LDPM results are in good agreement with the experimental results and show the model superior capability in modeling water penetration of dried concrete samples. The rate of water absorbtion is indeed directly related to the cited parameters as they govern concrete.

It is worth mentioning that the LDPM is capable of modeling the effect of crack and crack size on permeablitiy. As presented in the results of Figure 4.8 b, the presence of a crack increases locally the permeability which can be identified by a faster moisture saturation process. As the crack is larger at the very bottom of the sample, the local permeability field increases similarly to the experimental results. Indeed, one can observe at t=5 min that the bottom of the crack shows complete saturation. As water penetrates upward, the aperture of the crack opening decreases leading to a slower saturation process (saturation visible only at t= 2 hours). Last but not least, for both cases, uncracked and cracked sample, the LDPM simulates remarquably well the relative humidity profile in the concrete sample which matches well the experimental moisture distribution at different steps of the saturation process.

4.5. Concluding remarks

Evenly distributed cracks were achieved on the C-shaped beams specimen to study their effect on concrete permeability. A s expected, the presence of cracks increases significantly the material permeability which in a drying situation as presented translates in a more important water loss over time. Penetron admix allows for a 33% recovery in terms of water loss. The introduced two way coupling formulation is developed and adopted to model permeability behavior in both intact and fractured concrete. The dual lattice formulation allows for an accurate analysis of damaged construction materials and captures the local variations of permeability through the full coupling of mechanical and transport behavior. The M-LDPM is capable of modeling the mechanical behavior of any granular material (i.e. concrete, mortar...) as well as the local changes in permeability potentially engendered due to fracturing of concrete.The accuracy of the model in capturing local variations in terms of crack opening and fluid mass transport are achieved through modeling at the granular scale and as a result of the material heterogeneity. As expected, in the presence of cracks, the model realistically predicts the local increase in permeability which also correlates with the aperture. As expected for larger cracks, the process occurs faster than in the case of smaller cracks as observed in the experiments. This study does not include any viscosity study, however It is worth mentioning that the parameter μ governs the transported fluid viscosity. An increase in viscosity would theoretically translate in a slower fluid transport as for a decreasing μ, $D_h^\star$ Equation 4.26 decreases as well. last but not least, the obtained results confirm that the model captures well the short and long term evolutions of moisture transport.

CHAPTER 5

Fiber effect modeling in UHPC

5.1. Introduction

This investigation focuses on modeling the effect of various steel fibers types on the mechanical response of an ultra-high-performance concrete (UHPC). The Lattice Discrete Particle Model (LDPM) is a meso scale model capable of simulating concrete mechanical behavior and will be introduced further in this paper. The set of fibers considered includes, ZP305, Nycon type V, OL 10 mm and OL 6 mm fibers. Fiber shape and size had little impact on quasi-static properties in compression but had a significant impact on quasi-static tensile properties and dynamic penetration resistance in the LDPM-F prediction and experimental results. The benefits offered by the smaller fibers occurred prior to reaching the ultimate load carrying capacity. Once the ultimate strength was reached, larger fibers were more effective at bridging larger cracks. Smaller fibers provided improved penetration resistance.

Concrete is the most widely used material in the construction of civil engineering structures such as bridges, offshore, and high rise structures. Ultra-high Performance Concrete (UHPC) belongs to this new generation of concretes characterized by superior strengths. UHPC is composed of high cementitious materials content, fine aggregates, superplasticizer, a low water to cement ratio and sometimes fibers. The use of fibers has shown a moderate increase of compressive strength and significant increase of compressive

post peak load carrying capacity. Regarding tensile behavior, tremendous increase in ductility has been reported by Wille et al.[**78**]. The final UHPC composition optimized formula considering both performance and cost has not been proposed yet but promising studies are being conducted by Zemei et al.[**79**] particularly and other research groups.

Numerous factors can significantly affect UHPC mechanical properties as shown in the work of [**56, 39**]. Among these factors, we list the fiber content, distribution, size and shape, as well as sample size and shape [**40**]. [**5**] focused on the effects of casting methods on flexural strength by pouring the fiber reinforced UHPC mixture in three different ways. The results showed that higher strength could be achieved for panels casted by pouring the cementitious mixture at the center of the molds resulting in fibers oriented in the plane normal to the loading direction. Last but not least, a new promising concept studied by Kim et al.[**41**], commonly known under the name of "fiber blending" was developed and consists in combining macro and micro fiber effects. As explained further in this paper, fiber size matters as smaller fibers will enhance strength performance while longer fibers will improve the ductility.

The objective of the present study is to characterize the effect of steel fiber size and shape in Ultra-High Performance Concrete (UHPC), a class of concrete defined by its exceptionally high strength (170 to 250 MPa compressive strength) and durability. Four different fiber types are considered in the experimental program performed at ERDC: the Bekaert ZP-305, Nycon Type V, Bekaert OL.2/10mm and Bekaert OL .16/6mm [**24**]. The main objective of the work performed at Northwestern University is to simulate several mechanical quasi-static and dynamic tests performed on UHPC using the four fiber types [**24**]. The Lattice Discrete Particle Model (LDPM) was calibrated and validated by fully

identifying the parameters of the fiber bond law. The Direct Tension Test (DTT) was performed on UHPC dog bone samples with randomly distributed fiber and samples with oriented fibers. Fiber orientation is one of LDPM-F features and is explained further in the discussion.

Penetration and perforation tests have always been challenging to model. Continuum approaches are very limiting to simulate a fracture based test where capturing the stable transition between continuum and discrete reveals itself to be challenging. Also, modeling the heterogeneity of concrete with a continuum model requires additional work, often contributing to the high increase of computational cost. Discrete approaches are in this situation more natural and provide results that are in good agreement with the available experimental results. The LDPM-F showed great capability in predicting accurately the damage and kinetic energy absorbed in square cross section (304.8x304.8 mm^2) UHPC fiber reinforced slabs during the penetration and perforation tests. The slabs were cast with four different thicknesses : 25.4 mm, 50.8 mm, 63.5 mm and 76.2 mm. Each panel was impacted with a Fragment Simulating Projectile (FSP) that had an impact velocity of 1067 m/s. The purpose of this experimental campaign was to investigate the limit between perforation and penetration for a given initial velocity (1067 m/s here) by varying the thickness of the slabs from 25.5 mm to 76.2 mm. Another way to look at the campaign consists in considering that the dynamic tests aimed at finding which panel thickness has a ballistic limit of 1067m/s.

5.2. Discrete numerical modeling

5.2.1. Matrix definition

This section presents the numerical modeling of quasi-static experimental UHPC mechanical testing, performed by the United States Army Engineer Research and Development Center (ERDC). The simulated experimental results involve compression tests, 4 point bending tests and Direct Tension Tests (DTT) for dog bone samples cast in molds and water jetted from UHPC slabs. The interest in considering two casting methods comes from the fact that when UHPC is poured in molds, fibers tend to orient in the direction of loading. This orientation provides additional resistance reflected in higher tensile strengths. One common alternative consists in casting larger volumes of UHPC to minimize fibers orientations and extract dog bone samples from it. The modeling of the experimental tests in Figure 5.4 presents the UHPC sample geometries and applied boundary conditions.

Table 1 summarizes the compositions of plain UHPC (no fibers) and UHPC-Fiber reinforced that are then used in LDPM-F to generate a representative mesh. The model mesostructure considers one type of aggregate that includes silica, flour, and sand. To approximate the internal structure of UHPC, a coarse-grained approximation technique is used to reduce the computational cost. Typically, in UHPC, the maximum aggregate size varies around 0.6 mm, however the LDPM-F simulations consider respectively a minimum and maximum aggregate size of 2 mm and 4 mm (coarse graining approximation introduced by Smith et al. [**66**]). [**24**] presents the different fiber types that have been used in the experiments and that were simulated with the LDPM-F. The geometrical

Table 5.1. CTB mixture proportion.

Material	Proportion by Weight
Cement	1.00
Silica Fume	0.389
Silica Flour	0.277
Silica Sand	0.967
HRWRA	0.0171
Water	0.208
Steel Fibers	0.310

Table 5.2. Fibers description and paramters in LDPM-F.

Fiber Type	ZP305	Nycon	OL 6 mm	OL 10 mm
Length [mm]	20	29	6	10
Cross section	Circular	Rectangular	Circular	Circular
Diameter [mm]	0.5	-	0.16	0.2
Volume fraction [%]	3.15	8.9	3.15	3.15
τ_0 [MPa]	11.5	3.5	10	10
G_d [N/m]	100	0	50	30
β	-0.05	-0.3	-0.02	-0.04

and mechanical features summarized in Table are then given to the model to realistically simulate the contribution of each fiber.

5.2.2. Modeling of fibers

LDPM-F approximates the geometry of each fiber by generating a straight cylindrical fiber that is characterized by its radius r and length l. The fiber shape effect on the mechanical properties of UHPC is implicitly included in the fiber-matrix interaction law definition and will be discussed further in the paper. For the ZP306, OL0.2/10mm, and OL0.16/6mm, the LDPM-F and actual fibers geometries are identical and the actual fiber geometry can explicitly be modeled using the LDPM-F. However, the Nycon type V has a rectangular cross-section that cannot be modeled using straight cylindrical fibers.

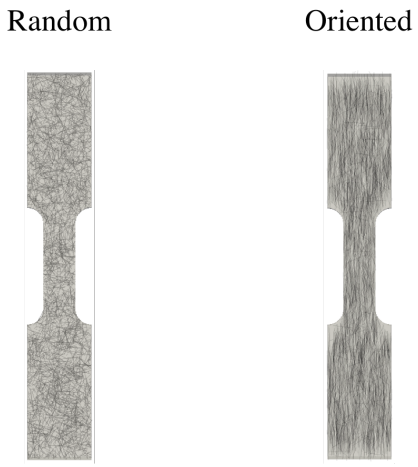

Figure 5.1. LDPM-F a) Random and b) Oriented fibers distribution.

Originally, the LDPM-F simulates fiber effects by modeling the concrete-fiber surface of contact ruled by the calibrated fiber-matrix interaction law. As far as the modeling of the Nycon type V, the radius of the LDPM-F fiber was calculated so that the LDPM-F fiber outer surface equals the actual fiber outer surface. Considering all of the above, a new volume of fibers $v_{f'}$ had to be computed to account for the volume difference between the actual and modeled fibers. By using the new volume of fibers $v_{f'}$ for the simulations, the experimental and modeled samples contained the same number of fibers.

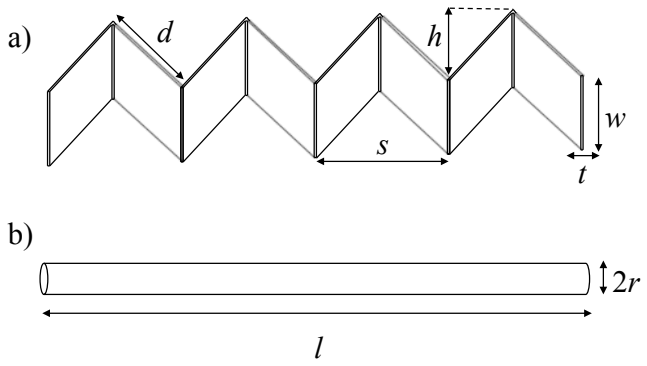

Figure 5.2. a) Nycon type V actual and b) Modeled LDPM-F fibers geometries.

$$v_{f'} = v_f \frac{\pi s r^2}{2twd} \tag{5.1}$$

where $v_{f'}$ is the LDPM-F equivalent volume fraction of fibers, v_f designates the experimental volume fraction (3.15%). t, w and s represent respectively the thickness, width and shortest spacing between two peaks of actual Nycon type V fibers. Also, $d = \sqrt{s^2/4 + h^2}$ where h is the vertical distance between an upper and lower peak.

Table 3 displays the information given as inputs to LDPM-F for each fiber type. Nycon type V reinforced UHPC samples generated in LDPM had a volume fraction that is 2.76 times larger than the actual fiber volume fraction.

5.3. LDPM calibration and validation

5.3.1. Calibration

[**66**] calibrated the UHPC matrix based on the results of quasi-static mechanical tests conducted on plain UHPC by Scott et al. [**24**] in 2013.

Figure 5.3 presents the comparison between the experimental and LDPM-F simulation results of the uniaxial unconfined compression test on ZP305 reinforced UHPC.

Two sets of simulations were carried out to compare the strengths of the old (used in 2013 for parametric identification by Smith et al. [**66**]) and latest UHPC (2016). The results were used to evaluate whether the material parameters associated with the latest UHPC needed to be adjusted or not. In the set of experiments conducted by Smith et al.[**66**], plain UHPC showed a higher compressive strength than the UHPC ZP305 reinforced presented in the latest report by Scott et al. [**24**]. This observation remains

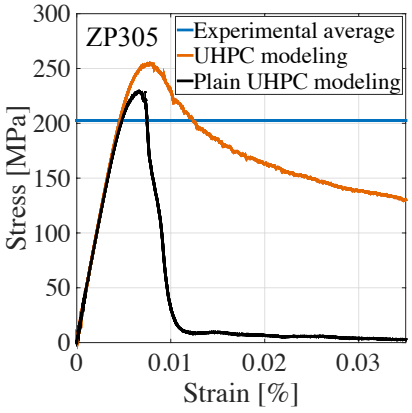

Figure 5.3. Compression test comparison between experiments and LDPM-F modeling results based on the 2013 parametric identification.

valid for the four point bending tests. As expected, the experimental observations are confirmed by the LDPM-F results. This preliminary work led to the conclusions that the UHPC matrix parameters needed to be calibrated based on the experimental work modeled in this paper. The only material parameter that was calibrated was the facet tensile strength σ_t which will be taken equal to 3 MPa (versus 4 MPa in [**66**]) for the set of LDPM-F simulations presented in this paper.

Calibrating LDPM-F parameters consisted in identifying the model parameters governing the fiber-matrix law interaction for each fiber type. The three main governing parameters are G_d, τ_0 and β, which respectively correspond to the bond fracture energy between the fiber and the matrix, the bond frictional stress of the embedded segment of the fiber and the slip hardening-softening parameter.

Generally, as a fiber is being pulled out of concrete, its initial friction resistance is a function the debonding fracture energy G_d and frictional resistance (β and τ_0). However, once a fiber has debonded, its resistance depends on its frictional resistance only.

Table 5.3. LDPM parameters for simulations.

LDPM parameter	Value
Compressive yielding stress	500 MPa
Initial hardening modulus ratio	0.36
Densification ratio	2.5
Transitional strain ratio	2
Shear strength ratio	17
Initial friction	0.5
Softening exponent	0.2
Deviatoric strain threshold ratio	2
Deviatoric damage parameter	1
Asymptotic friction	0
Transitional stress	300 MPa
Tensile strength	3 MPa
Tensile characteristic length	150 mm
Maximum aggregate size	4 mm

Ideally, the fiber-matrix interaction law is calibrated on the single fiber pullout test. This experimental campaign did not involve any single pull out test, hence, the fiber-matrix interaction law parameters are identified on the Direct Tension Test (DTT) experimental results using data of samples cast in molds (Oriented fibers).

The direct tension tests were modeled as dogbone-shaped specimens with a middle gauge length of 80 mm and a constant rectangular cross section of 30x30mm^2. Two rigid steel plates are defined at the top and bottom ends of the sample to apply boundary conditions. The plates are modeled with hexahedron solid elements, having triangular mesh surfaces, and tied to the LDPM surface nodes through master and slave constraints. All translational (ux; uy; uz) and rotational (rx; ry; rz) degrees of freedom are restrained excluding the vertical translation (uy) at the top of the specimen where a uniform constant displacement of 5 mm/s is imposed as shown on Figure 5.4. In the LDPM-F, a preferential orientation scale factor Sy is used to control how strong the orientation of the fibers is.

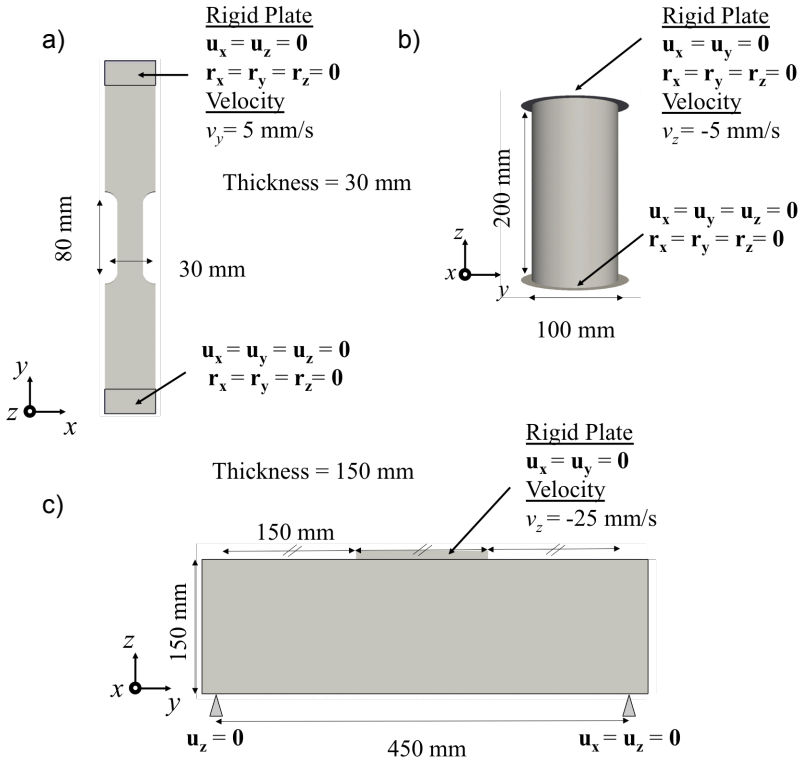

Figure 5.4. Boundary conditions and surface nodes for the a) Dog Bone Test b) Uniaxial compression and c) 4-point bending test.

For Sy=1 there is no preferential direction while for $S_y = 22$, a fiber is 22 times more likely to be oriented in the given direction than to a direction orthogonal to it.

The bond strength and debonding fracture energy parameters are selected to match the tensile strengths given in the experiments, while the pull out hardening parameter is calibrated using the post-peak response of the stress vs strain curves. Figure 5.5 displays the results of the experimental and calibration of the DTT for each fiber type in terms of stress versus strain.

In the previous set of identified parameters by Smith et al. [**66**], the debonding fracture energy G_d was taken equal to 0 Nm $^{-1}$ for the ZP305 fibers. The impact on the mechanical

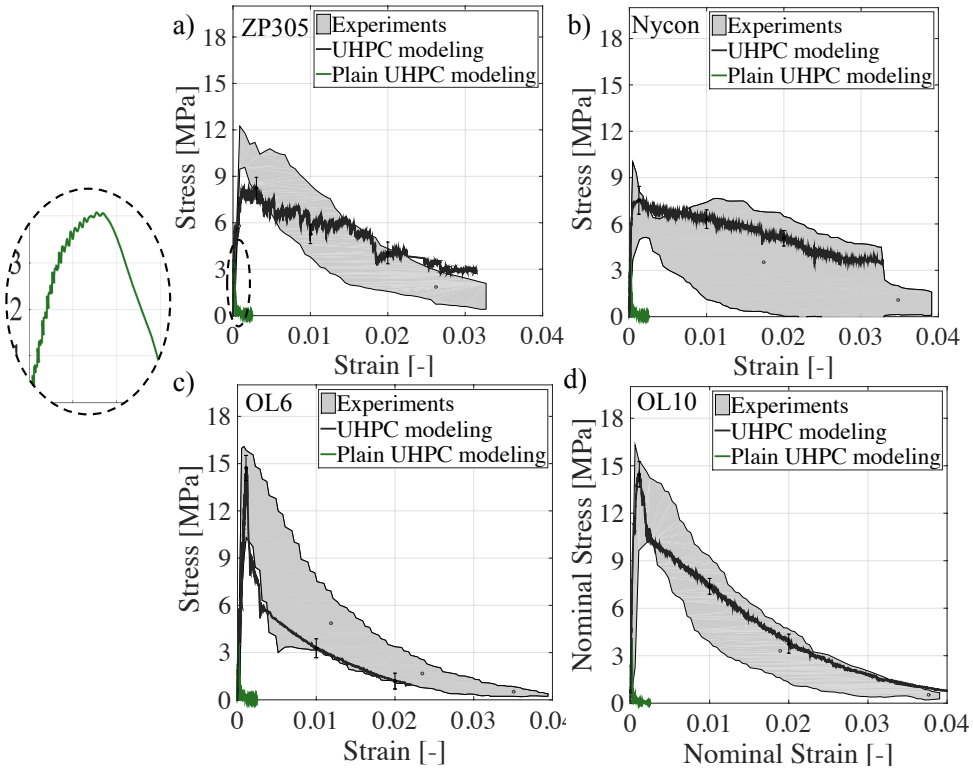

Figure 5.5. Stress versus strain curves of Direct Tension Test on dog bone samples cast in molds calibration with the LDPM-F for a) ZP305 b) Nycon c) OL6 and d) OL10 type of fibers.

properties associated with the debonding fracture energy can only be appreciated when very small strains (small crack openings) intervene. As one can see on Figure 5.7, the characteristic size of the crack opening depends on the test design as the stress distribution will also vary. The order of magnitude of crack openings in the direct tension and 4 point bending tests are respectively 0.1 mm and 0.4 mm. Hence, a four point bending test will show less sensitivity to G_d than a DTT performed on a dog bone sample will. The calibration of the DTT explains why non-zero fracture energies were needed to achieve proper calibration of the model.

LDPM-F has successfully been calibrated on the DTT for oriented fiber reinforced UHPC specimens. Table 5 summarizes the calibrated parameters for each fiber type for the LDPM-F simulations.

5.3.2. LPDM-F validation

This section introduces how the LDPM-F is validated and demonstrates a superior capability in accurately predicting the mechanical responses of UHPC-Fiber reinforced for the four fiber types. All model predictions were performed without further change to the previously calibrated LDPM-F parameters, and their results compared to experimental data were not utilized during the parametric identification.

Fracture Test. Figure 5.6 shows the results comparison of 4 point bending test experiments and simulations in terms of load versus mid-span deflection. The UHPC samples are 150x150x450mm^3 prisms, each one reinforced with one type of fiber. In the 〃 impact of steel fiber size and shape on the mechanical properties of UHPC〃 report by Scott et al. [**24**], no information was given concerning fiber orientation. Hence, for the modeling, both fiber orientations were considered providing a representative range of responses limited by the lower limit modeled with randomly distributed fibers and upper limit where the fibers are oriented. Simulations with randomly distributed fibers show, as expected, lower strengths than the experimental results for the 4 types of fibers. On the contrary, the predictions with preferential fiber orientation match very well the experimental data for all fiber types suggesting a possible fiber alignments in UHPC beams. Last but not least, the model not only predicts well the peaks and softening regimes of the four point bending tests, but it also captures well the UHPC stiffness (loading phase).

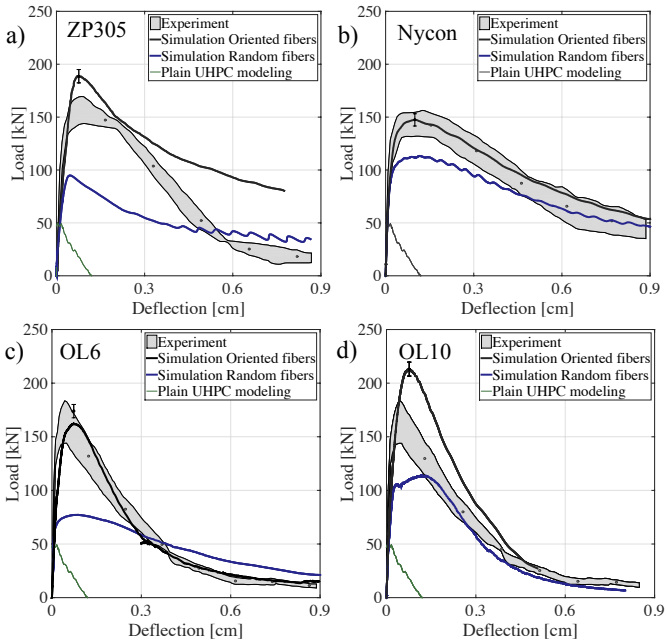

Figure 5.6. Force versus middle-span deflection of 4-point bending test results prediction and validation with the LDPM-F for a) ZP305 b) Nycon c) OL6 and d) OL10 type of fibers.

Direct tension Test.

This section presents a comparison of the results of the direct tension test on dog bone samples watter jetted from a 127x127x533mm^3 UHPC slabs. The predictions obtained from the LDPM-F and the UHPC experimental results reinforced with randomly distributed fibers (water jetted samples) are displayed in Figure 5.8. LDPM-F successfully captures the peak strengths for the four fiber types. As one can see on Figure 5.5 , the DTT performed on OL6 reinforced UHPC dog bone samples experimentally and numerically show a tensile strength of 16MPa with oriented fibers. In the case of randomly distributed fibers, the experimental data also display the same tensile strength (16MPa). As described by Scott et al. [**24**], for the OL6 fiber, although the dog bone samples have

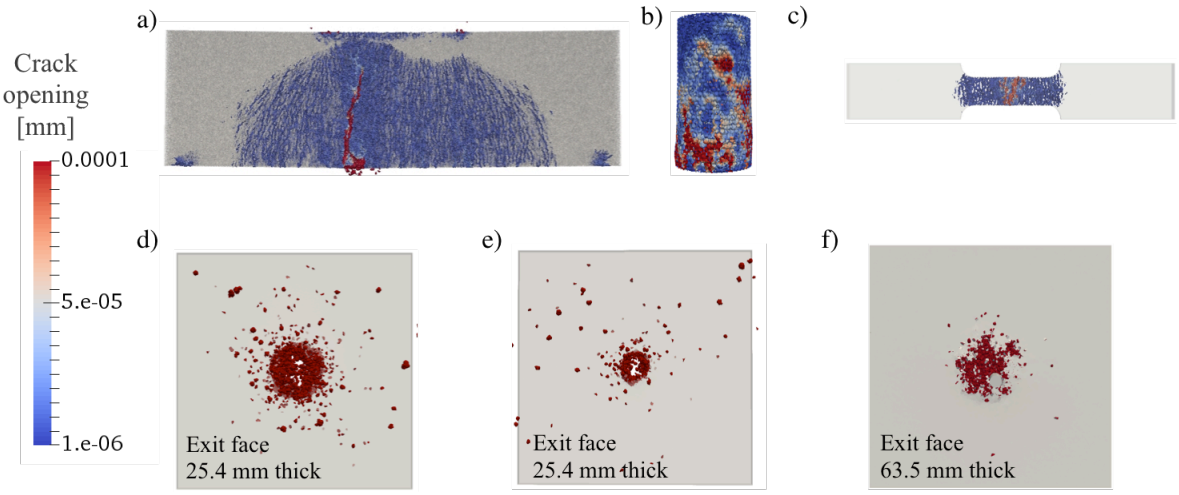

Figure 5.7. LDPM-F crack contours results for the a) Four point bending b) Compression c) Direct tension and d) Perforation test of a plain UHPC e) Perforation test of fiber reinforced UHPC and f) Crater generated by the penetration test of fiber reinforced UHPC.

been extracted from larger UHPC slabs, some fiber orientation in the direction of loading has been noticed by the experimentalist team explaining why the tensile strength in the experiments is higher than what the model predicts. This unexpected experimental fiber alignment is the precise reason why an accurate model needs to be developed. Indeed, when accurate models are combined with experimental work, they can be used to underline unexpected experimental results or even extrapolate additional results by modeling different tests.

Compression test.

This part discusses a comparison between the experimental (compressive strengths) and numerical results for uniaxial compression tests performed on 100x200 mm^2 cylinders of UHPC-Fiber reinforced. The simulation results are plotted in terms of stress versus strain in Figure 5.9. As expected, the fibers have very little effect on the compressive

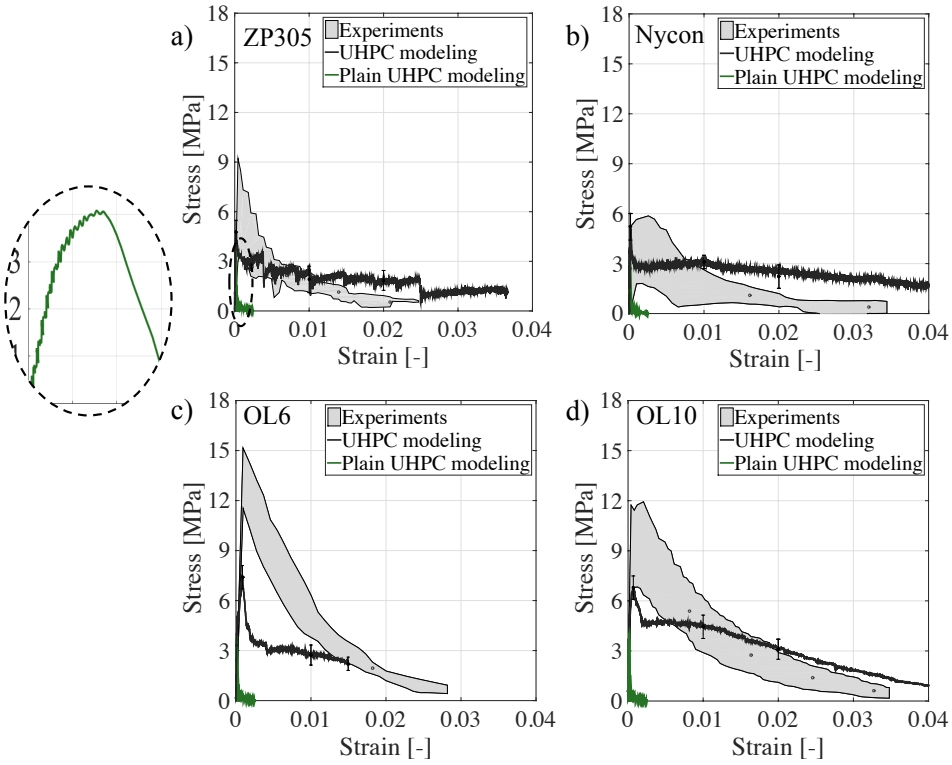

Figure 5.8. Stress versus strain curves of Direct Tension Test on water jetted dog bone samples prediction and validation with the LDPM-F for a) ZP305 b) Nycon c) OL6 and d) OL10.

strength of UHPC. The matrix mechanical properties are however influential on the compressive response. LDPM-F predicts the strength increase associated with the use of Nycon, OL6 and OL10 fibers very well. As expected, the softening from the LDPM-F simulations show a more ductile behavior due to the contribution of fibers.

Additional observations. Figure 5.7 displays the experimental failure modes observed for the uniaxial compression and dog bone test. In addition to capturing the fibers effect on mechanical properties of UHPC, the LDPM-F shows in Figure 5.7 superior capability in mimicking the failure modes for both tests. In the case of uniaxial compression, one can observe vertical and diagonal cracks, which conform to what one can observe in typical

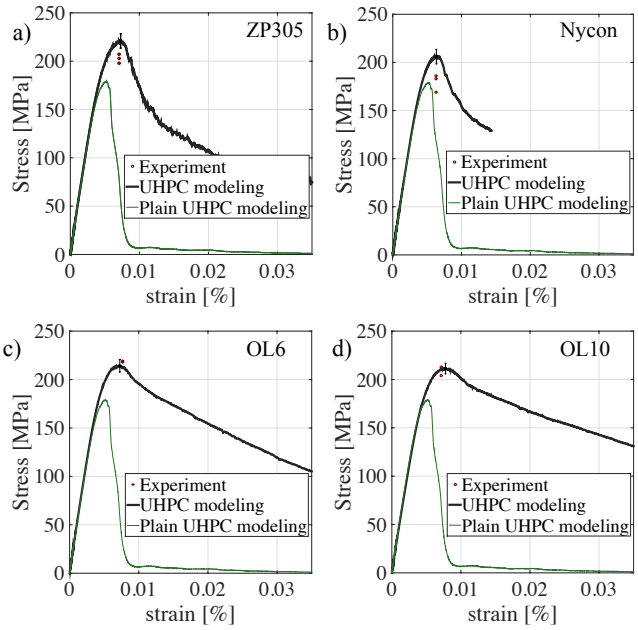

Figure 5.9. Stress versus strain curves of compression test results prediction and validation with the LDPM-F for a) ZP305 b) Nycon c) OL6 and d) OL10.

compression test. In the case of the dog bone test, one can see in the simulations the development of cracks in the plane orthogonal to the direction of loading. This observation is consistent with the observed experimental mode of failure as well.

5.4. Dynamic simulations : Penetration and perforation tests

5.4.1. Dynamic simulations modeling

The projectile mesh was created using the LDPM mesh as shown on Figure 5.10. The projectile was simulated using high strength steel with an elastic modulus of 200 GPa. In the LDPM modeling, the bullet has no displacement constraints and is only subjected to an initial velocity v_0 of 1067 m/s. Concerning the panel, all edge nodes are fixed with no possibility of translation nor rotation as explained by Smith et al. [**66**].

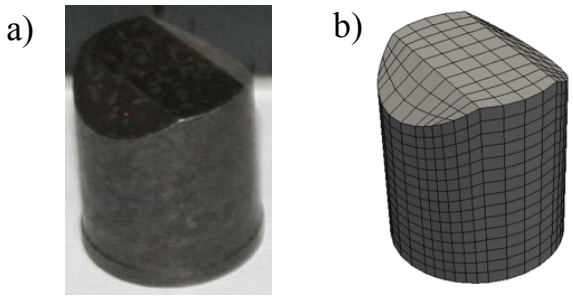

Figure 5.10. Fragment Simulating Penetration (FSP) a) Photography and b) LDPM mesh.

5.4.2. Dynamic testing results and discussion

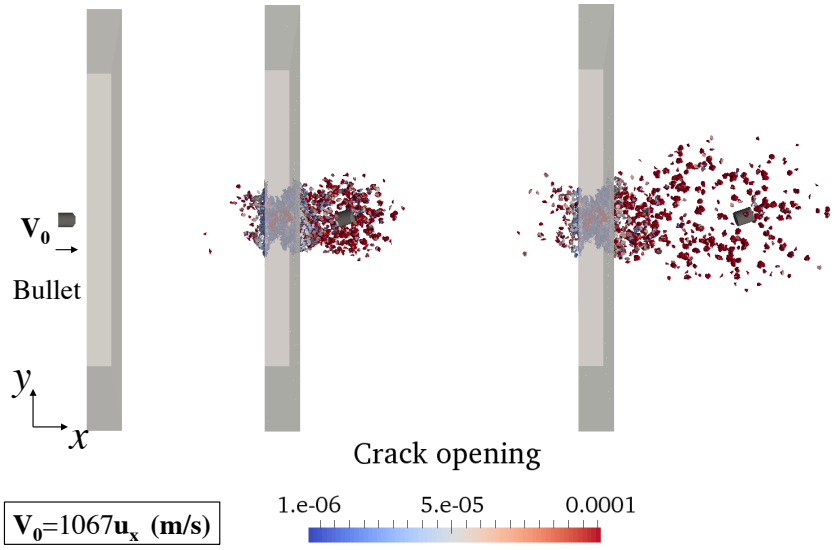

Figure 5.11. Dynamic test design.

The numerical results are in good agreement with the experimental results as the damage states and responses of the panels were consistent for the four fiber types. Figure 5.11 shows the the comparison of the bullet average residual velocity between experimental result and LDPM simulations. The LDPM-F was used to extrapolate the intial part of the curve tail by simulating the perforation of a 12.7 mm thick panel and considering

that for a panel of 0 mm thickness the exit velocity equals the initial velocity v_0. For each fiber type, five different thicknesses were considered for the panels. Similarly to the experimental observations, the numerical results show less than three percent (versus five percent in experiment) difference. The LDPM-F can accurately capture the quasi-static and dynamic behaviors with one single set of calibrated parameters only. Considering the four fiber types and thicknesses, the LDPM-F simulations predict the experimental residual velocities with a maximum error of eight percent for the OL 10 fibers and minimum error of six percent for the OL 6 fibers.

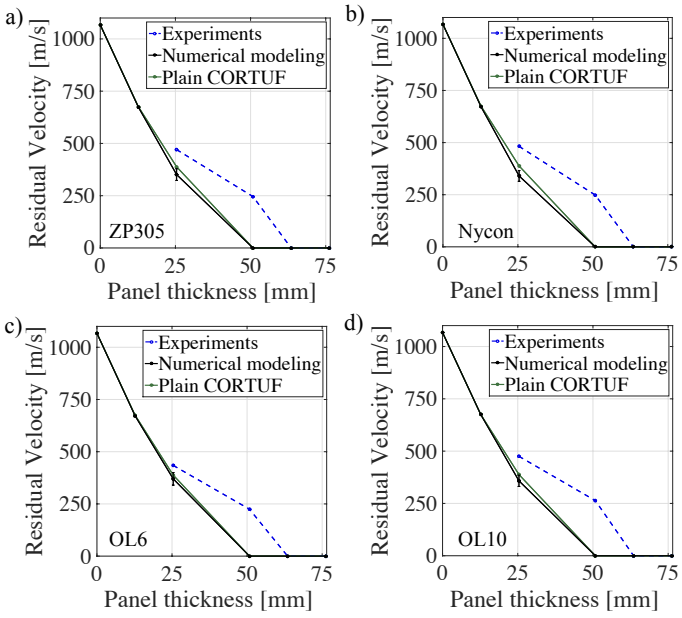

Figure 5.12. Residual velocity vs slab thickness results prediction and validation with the LDPM-F for a) ZP305 b) Nycon c) OL6 and d) OL10.

Loss weight due to the damage ranged from 0.75 to 5.5 percent in the experiments and from 0.8 to 4.9 percent in LDPM-F modeling. The model predicts the experimental relative weight losses with a maximum average error on the four thicknesses of 1.75 percent for the OL 10 fibers and minimum average error of 1.4 percent for the Nycon fibers. The

LDPM consistently predicts lower weight losses for the slabs reinforced with OL 6, which actually is the smallest fiber among all four. This observation is also consistent with what was observed experimentally. The model is able to capture that, for a higher fiber density, less material fractures or spalls. The overall conclusion that can be drawn from the consistency of the observations is that the OL 6 fibers are the most efficient among all four fiber types as they display the lowest residual velocities and weight losses. The OL 6 fibers combine two key advantages, the first is to efficiently absorb the kinetic energy of the impacting bullet (lower exit velocity) and the second is to localize the damage (lower weight loss). Also the OL6 provided the highest strength in compression and tension during the quasi-static experimental campaign. The latter confirms that the performance of the OL6 is the best among the 4 presented fiber types.

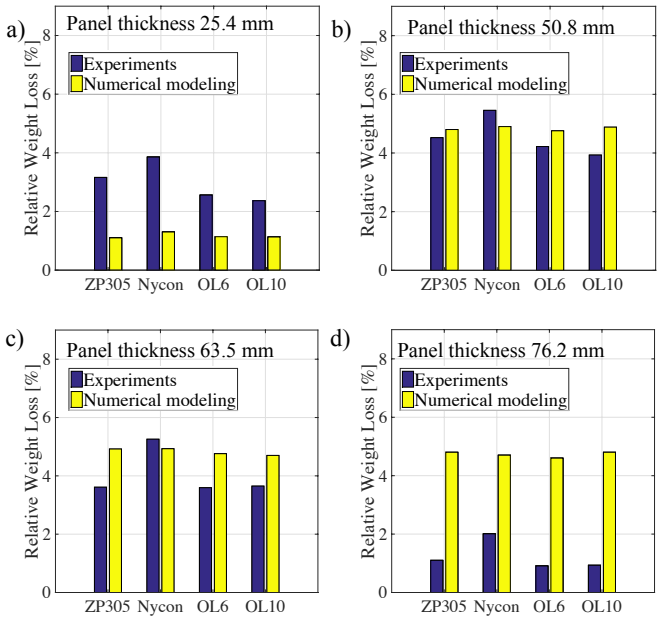

Figure 5.13. Relative weight loss vs fiber types results prediction and validation with LDPM-F for a) 25.4 mm b) 50.8 mm c) 63.5 mm and d) 76.2 mm thick slab.

5.4.3. Qualitative appreciations

Additional simulations considering the modeling of perforation and penetration tests on plain UHPC slabs were also performed. As expected, the damage distribution is more important when fibers are used while on the contrary plain UHPC displays localized damages significantly as depicted in Figure 5.7d and e. The LDPM-F even mimics the damage distribution that were observed experimentally as presented in Figure 5.7d. As far as the 50.8 mm thick panels perforation, the damage distribution observed in the experiments and simulations is identical, however the FSP perforates the panel in the experiments while it only penetrates in the LDPM simulations. Recent findings demonstrated that when concrete is subjected to large strain, shear resistance is negatively impacted. In his experimental work, [**80**] tested reinforced concrete beams, designed an anti-symmetric loading system to generate and measure shear stresses and strains. The concrete beams subjected to larger strains were additionally reinforced in shear to eventually prevent premature failure of the sample. However, although the concrete beams were over reinforced, their shear strengths were equivalent to one observed in less reinforced in shear samples. The single difference between these two samples is the imposed strain which is larger for the more reinforced samples. This observation confirms that for larger strains concrete is weaker in shear. By definition, dynamic testing involves large strain rates and strains which explains why the model slightly overestimates the shear resistance of fiber reinforced UHPC slabs. To numerically capture this shear reduction effect, researchers have developed numerical approaches based on a parametric identification and calibration of an introduced shear reduction parametric function as presented in the study performed by Mihaylov et al. [**48**]. As the work related to shear reduction factor in LDPM is still

ongoing, results without the shear reduction factor are presented in this paper. For all the other panel thicknesses, the LDPM-F predictions and experimental results are in good agreement. Last but not least, the experimental 63.5 mm thick panels displayed a crater on the exit face due to the FSP penetration generating a damage wave propagation towards the exit face. The LDPM captures this phenomenon well as depicted on Figure 5.7f.

5.5. Concluding remarks

The LDPM-F is capable of simulating the impacts of steel fiber size and shape on the mechanical properties of Fiber Reinforced Ultra-High Performance Concrete (FRUHPC) by first calibrating the parameters of the fiber-matrix law on quasi-statics Direct Tension Test experiments (cast in molds). Since, the compressive strength of this batch is lower than the previous one [**66**], the uniaxial compression test performed on ZP305 reinforced UHPC specimen is necessary to recalibrate the new matrix mechanical properties. LDPM-F has demonstrated a superior capability in predicting the experimental mechanical responses in the cases of 4-point bending test, uniaxial compression, DTT (water jetted samples), perforation and penetration tests for all fiber types. Also, LDPM-F successfully simulates the effect of fiber orientations (DTT and 4-point bending test). Last but not least, the LDPM-F captures and predicts accurately the crack pattern observed on experimental UHPC samples.

APPENDIX A

The Lattice Discrete Particle Model-Fibers formulation

Fiber reinforcing is always used in UHPC to increase toughness (energy absorption capability) and ductility. Within LDPM, fibers are explicitly modeled by generating spatial distributions mimicking the ones found in real specimens. From a geometric point of view the physical fibers can be described using few parameters, in the case of straight fibers: volume fraction, V_f, length, L_f, and equivalent diameter, d_f. Each fiber is modeled using a sequence of one or more segments linked together. Single segments are sufficient for generating straight fibers. Multiple segments are necessary for generating tortuous fibers. These geometric parameters are used for generating random fibers inside a control volume. For cast fiber-reinforced concrete specimens, the control volume is assumed to be equal to the volume of the concrete part. In this case, fiber location and orientation are affected in the vicinity of the boundary.On the contrary, formachined or cored specimens, the control volume is assumed to be larger than the actual specimen so that fibers intersecting the external surface of the specimens are treated as cut. The portion of a cut fiber inside the specimen is shorter than the length of original fiber, and this affects themechanical characteristics of the fibereconcrete interaction near the specimen boundaries. The following algorithm is used for generating random fibers whose number inside a given control volume V can be computed as $N = 4V_f V/(L_f \pi d_f^2)$. The first scenario details the case of uniformly distributed fibers. For each fiber, a random point with uniform probability in space inside the control volume is selected as the initial point of the fiber. An initial random direction

is then computed by (1) generating, in a unit cubic volume, a series of additional random points with a uniform probability in space, (2) rejecting all points outside a unit sphere, and (3) accepting the first point occurring inside the unit sphere. The vector connecting the fiber origin to this point inside the unit sphere identifies an unbiased spatial direction. The computed direction is used to initialize the fiber. If the fiber consists of multiple segments to simulate fiber tortuosity, then the direction of each additional segment is modified using the following logic. A random direction, $\mathbf{w}$ is computed as done previously, followed by the normal n to the current fiber direction $\mathbf{u}_1$ as $boldn = m/[m]$, where $m = w - (w.u_1)u_1$. A proportional component is then added to the tortuosity factor t by $\mathbf{v_2}$=$\mathbf{u_1} + t\mathbf{n}$, and the new fiber direction $\mathbf{u}_2$ is normalized using $\mathbf{u}_2$= $v_2/[v_2]$. For t= 0, the fiber continues straight in the initial direction. If the fiber exits from the control volume V, the fiber is discarded. In some cases, fiber orientation is not random but has a bias towards a preferential direction. This bias is obtained by a scaling factor, s, for a stated preferential direction. For $s = 1$, there is no preferential alignment, while a generic value of s makes alignment s times more likely for the preferential fiber orientation. The most appropriate scaling factor must be chosen through comparisons between numerical and experimental specimens. The random fiber generation algorithm is adjusted to include preferentially oriented fibers after the spatially random direction is computed. The dot product $c = n\dot{d}$ of random n and preferential orientation d is computed. The random direction is then extended along the preferential direction and normalized to compute the random fiber direction by $\mathbf{v} = \mathbf{n} + (s-1)cd$ and $n = v = |v|$. Figs. 4a and c show generated fiber distributions without and with preferential orientation. In the spirit of the discrete multi-scale physical character of LDPM, the occurrences of fiber-facet intersections are

determined by actually computing the locations where fibers cross inter-cell facets. This computation can require significant resources for large models in terms of both time and memory. For this reason, an efficient bin-sorting algorithm was developed for computing these intersections. For each intersection, the lengths of the fiber on both sides of the facet and the angle at which the fiber intersects the facet are also computed. These parameters are saved in the facet data structure and used during the simulation for computing the fiber effect. The modeling of fiber reinforcement in CORTUF is then completed with the simulation of fibereconcrete interaction, which requires the formulation of a local force versus slippage constitutive equation simulating fine-scale failure phenomena occurring at the interface between fibers and embedding concrete matrix. The LDPM-F formulation [88,89] of such a law, adopted in this study and summarized in Appendix A2, includes the description of the following failure mechanisms, (1) fiber/matrix debonding, (2) fiber frictional pull-out, (3) local matrix failure due to stress concentration at the point of exit of fibers from the matrix (micro-spalling), (4) pull-out strength increase due to additional frictional effects caused by change of direction of fiber during cracking (snubbing), (5) fiber rupture, (6) fiber strength reduction due to localized plastic deformations, and (7) fiber yielding due to local fiber bending. In addition to these failure mechanisms, there is evidence for CORTUF concrete that splitting failure, i.e., a sudden and dynamic propagation of a crack in a plane containing the fiber axis, might contribute significantly to the overall tensile resistance in tension of the material. Let us consider a straight segment of a fiber subject to tension. At the interface between the fiber and the surrounding concrete, shear stresses develop, which in turn lead to inclined principal stress directions. When the maximum principal stress exceeds the tensile strength, radial cracks initiate,

and the concrete matrix surrounding the fiber is forced to transfer load through an inclined compression field, see Fig. 1c. The component of this inclined field acting to the axis of the fiber results in an expansive pressure on the surrounding concrete of magnitude $p = P_f \tan\alpha/(\pi d_f L_e)$. The angle α depends on both the geometric characteristics of the fiber and the remote stress state. From this pressure, the maximum circumferential tensile stress acting at the fiber/matrix interface (see Fig. 1c) can be computed approximately as

$$\sigma_\theta^{max} = p\frac{Fc_f^2/d_f^2 + 1}{4c_f^2/d_f^2 - 1} \tag{A.1}$$

where cf is the distance between the fiber axis and the closest external surface of the specimen. By introducing the expression for p into Eq. (5), setting the failure condition, $\sigma_\theta^{max} = \sigma_t^\star$, and solving for the fiber force, one can calculate the splitting force for c_f/d_f ¿¿1

$$P_f^{split} = \left(\frac{\pi d_f L_e \sigma_t^\star}{\tan\alpha}\right)\frac{Fc_f^2/d_f^2 + 1}{4c_f^2/d_f^2 - 1} \approx \frac{\pi d_f L_e \sigma_t^\star}{\tan\alpha} \tag{A.2}$$

where $\sigma_t^\star$ can be assumed to coincide with the tensile strength of the matrix or the composite, depending on fiber concentration and level of fiber interaction. At this point, a few observations are in order. (1) The splitting mechanism highlighted below is typically observed in reinforced concrete members [102] when concrete rebars are not provided with proper confinement through either enough concrete cover or transverse reinforcement. It is worth pointing out that, in regular concrete, rebars have diameter sizes of the same

order of the aggregate particles; the same situation arises in CORTUF concrete where fiber diameters have similar characteristic sizes of material heterogeneities. Based on this analogy, it seems logical to observe in CORTUF failure mechanisms that are similar to the ones of reinforced concrete and that are not observed in standard fiber-reinforced concrete. (2) Splitting failure is expected to be negligible in the case of fiber reinforcement with low stiffness and high Poisson's ratio compared to the one of concrete (e.g., for Polyvinyl Alcohol, PVA, fibers), because such properties prevent the build-up of a significant expansive pressure. (3) If bond resistance is limited, bond failure occurs before the inclined cracks can develop. As such, straight fibers are less prone to induce splitting failure than hooked and bent fibers.

Bibliography

[1] Bažant Z.P. & Steffens A. Mathematical model for kinetics of alkali-silica reaction in concrete. *Cement and Concrete Research*, 30(3):419–428, 2000.

[2] M. Alnaggar, G. Cusatis, and G. Di Luzio. Lattice discrete particle modeling (LDPM) of alkali silica reaction (ASR) deterioration of concrete structures. *Cement and Concrete Composites*, 41:45 – 59, 2013.

[3] M. Alnaggar, G. Di Luzio, and G. Cusatis. Modeling time-dependent behavior of concrete affected by alkali silica reaction in variable environmental conditions. *Materials*, 10(5), 1 2017.

[4] ASTM. Standard practice for petrographic examination of hardened concrete,. 2018.

[5] S. J. Barnett, J-F Lataste, T. Parry, S. G. Millard, and M. N. Soutsos. Assessment of fibre orientation in ultra high performance fibre reinforced concrete and its effect on flexural strength. *Materials and Structures*, 43(7):1009–1023, Aug 2010.

[6] Z.P. Bažant, Siddik S., and Jin K. K. Effect of cracking on drying permeability and diffusivity of concrete. *ACI Materials Journal*, 84(5):351–357, 9 1987.

[7] O. Bayrak. ASR/DEF-damaged bent caps: shear tests and field implications. 01 2009.

[8] Z. P. Bažant and S. Rahimi-Aghdam. Diffusion-controlled and creep-mitigated asr damage via microplane model. i: Mass concrete. *Journal of Engineering Mechanics - ASCE*, 143(2), 2 2017.

[9] Z.P. Bažant. Prediction of concrete creep and shrinkage: past, present and future. *Nuclear Engineering and Design*, 203(1):27 – 38, 2001.

[10] Z.P. Bažant and S. Rahimi-Aghdam. Century-long durability of concrete structures: Expansiveness of hydration and chemo-mechanics of autogenous shrinkage and swelling. *Journal of Engineering Mechanics - ASCE*, 2018.

[11] M. Ben Haha. Mechanical effects of alkali reaction in concrete studied by sem-image analysis. 01 2006.

[12] F.-K. Benra, Hans Josef D., Ji Pei, S. Schuster, and B. Wan. A comparison of one-way and two-way coupling methods for numerical analysis of fluid-structure interactions. 2011, 11 2011.

[13] H. Beushausen, M. Alexander, and Y. Ballim. Early-age properties, strength development and heat of hydration of concrete containing various south african slags at different replacement ratios. *Construction and Building Materials*, 29:533 – 540, 2012. Arc furnaces;Fresh and hardened properties;Ground granulated blast furnace slag;Heat of hydration;High water;Hydration heat;Hydraulic activity;Long-term strength;Physical characterisation;Replacement level;Replacement ratio;Setting time;Slag concrete;Strength development;Strength values;Water/binder ratios;Workability;.

[14] ASTM C1250-07. Standard test method for determination of length change of mortar due to alkali-silica reaction. 04.02, 2009.

[15] S. Chatterji, A.D. Jensen, N. Thaulow, and P. Christensen. Studies of alkali-silica reaction. part 3. mechanisms by which nacl and ca(oh)2 affect the reaction. *Cement and Concrete Research*, 16(2):246 – 254, 1986.

[16] G. Cusatis, M. Alnaggar, and R. Rezakhani. Multiscale modeling of alkali silica reaction degradation of concrete. 10 2014.

[17] G. Cusatis, M. Alnaggar, and R. Rezakhani. Multiscale modeling of alkali silica reaction degradation of concrete. 10 2014.

[18] G. Cusatis, A. Mencarelli, D. Pelessone, and J. Baylot. Lattice discrete particle model (LDPM) for failure behavior of concrete. ii: Calibration and validation. *Cement and Concrete Composites*, 33:891–905, 2011.

[19] G. Cusatis, Andrea Mencarelli F., D. Pelessone, and J. Baylot. Lattice discrete particle model (ldpm) for failure behavior of concrete. ii: Calibration and validation. *Cement and Concrete Composites*, 33(9):891 – 905, 2011.

[20] G. Cusatis, D. Pelessone, and A. Mencarelli Figini. Lattice discrete particle model (LDPM) for failure behavior of concrete. i: Theory. 33:881–890, 10 2011.

[21] G. Cusatis, R. Rezakhani, M. Alnaggar, X. Zhou, and D Pelessone. Multiscale computational models for the simulation of concrete materials and structures. 1, 03 2014.

[22] G. Cusatis, R. Rezakhani, M. Alnaggar, X. Zhou, and D Pelessone. Multiscale computational models for the simulation of concrete materials and structures. 1, 03 2014.

[23] G D. Jr. Guthrie and Bill C. Detection of alkali-silica reaction swelling in concrete by staining. 01 1998.

[24] Scott D. A Wendy R. Long R. D Moser Brian H Green J. L O Daniel and Brett A W. Impact of steel fiber size and shape on the mechanical properties of ultra-high performance concrete. *No. ERDC/GSL-TR-15-22*, 1:2450–2457, 05 2011.

[25] G. Di Luzio and G. Cusatis. Hygro-thermo-chemical modeling of high performance concrete. i: Theory. *Cement and Concrete Composites*, 31(5):301–308, 5 2009.

[26] S. Esna Ashari, G. Buscarnera, and G. Cusatis. Micro-scale modeling of the inelastic response of a granular sandstone. 06 2015.

[27] R. Esposito. The deteriorating impact of alkali-silica reaction on concrete: Expansion and mechanical properties. 2016.

[28] Bangert F Kuhl D & Meschke G. Chemo-hygro-mechanical modelling and numerical simulation of concrete deterioration caused by alkali-silica reaction. 28:689–714, 06 2004.

[29] R. G.Charlwood. A review of alkali aggregate in hydro-electric plants and dams hydropower dams. *Hydropower Dams*, 05:31–62, 1994.

[30] P. Grassl. A lattice approach to model flow in cracked concrete. *Cement and Concrete Composites*, September 2008.

[31] G. D. Guthrie and J.W. Carey. A simple environmentally friendly, and chemically specific method for the identification and evaluation of the alkali-silica reaction. *Cement and Concrete Research*, 27(9):1407 – 1417, 1997.

[32] W. H. Mirza, S. I. Al-Noury, and W. H. Al-Bedawi. Temperature effect on strength of mortars and concrete containing blended cements. 13:197–202, 12 1991.

[33] W. K Hall. Notes on the effect of time element in loading reinforce dconcrete beams. 1:421–433, 1907.

[34] J. A. Hanson. Effects of curing and drying enviroments. 65, 01 1968.

[35] ASTM International. Standard test method for determination of length change of concrete due to alkali-silica reaction. 04.02, 2009.

[36] Akash J., Ankit K., Adarsh K., Yogesh V., and Krishna M. Combined use of non-destructive tests for assessment of strength of concrete in structure. *Procedia Engineering*, 54:241 – 251, 2013. The 2nd International Conference on Rehabilitation and Maintenance in Civil Engineering (ICRMCE).

[37] Ara A. Jeknavorian and Thomas D. Hayden. Troubleshooting retarded concrete. understanding the role of cement and admixtures through an interdisciplinary approach. *Cement, Concrete and Aggregates*, 13(2):103 – 108, 1991. Concrete Retardation;Extended Set Times;Hydration Reaction Retardation;.

[38] T. Jones. New interpretation of alkali-silica reaction and expansion mechanisms in concrete. pages 40–44, 01 1988.

[39] Su-Tae K., Yun L., Yon-Dong P., and Jin-Keun K. Tensile fracture properties of an ultra high performance fiber reinforced concrete (uhpfrc) with steel fiber. *Composite Structures*, 92(1):61 – 71, 2010.

[40] Su-Tae K., B. Y. Lee, J-K Kim, and Y. Yong Kim. The effect of fibre distribution characteristics on the flexural strength of steel fibre-reinforced ultra high strength concrete. *Composite Structures*, 25:2450–2457, 05 2011.

[41] D. J. Kim., Seung Hun P., Gum Sung R., and Kyung T. K. Comparative flexural behavior of hybrid ultra high performance fiber reinforced concrete with different macro fibers. *Construction and Building Materials*, 25(11):4144 – 4155, 2011.

[42] T. Kim, J. Olek, and H. Jeong. Alkali–silica reaction: Kinetics of chemistry of pore solution and calcium hydroxide content in cementitious system. *Cement and Concrete Research*, 71:36 – 45, 2015.

[43] C. Larive. Apport combinés de l'expérimentation et de la modélisation à la compréhension de l'alcali-réaction et de ses effets mécaniques. 06 1997.

[44] M.H. Lee, B.S. Khil, and H.D. Yun. Influence of cement type on heat of hydration and temperature rise of the mass concrete. *Indian Journal of Engineering and Materials Sciences*, 21(5):536 – 542, 2014. Adiabatic temperature rise;Analytical studies;Cement production;Crack indices;Different binders;Finite element thermal analysis;Heat of hydration;Mass concrete;.

[45] G. Di Luzio and G. Cusatis. Hygro-thermo-chemical modeling of high-performance concrete. ii: Numerical implementation, calibration, and validation. *Cement and Concrete Composites*, 31(5):309 – 324, 2009.

[46] G. Di Luzio and G. Cusatis. Solidification–microprestress–microplane (SMM) theory for concrete at early age: Theory, validation and application. *International Journal of Solids and Structures*, 50(6):957 – 975, 2013.

[47] P. Léger, P. Cote, and R. Tinawi. Finite element analysis of concrete swelling due to alkali-aggregate reactions in dams. *Computers & Structures*, 60(4):601 – 611, 1996.

[48] Boyan I. Mihaylov. Two-parameter kinematic approach for shear strength of deep concrete beams with internal frp reinforcement. *Journal of Composites for Construction*, 21(2):04016094, 2017.

[49] A. Mladenovič, S. Šturm, B. Mirtič, and J. Suput. Alkali-silica reaction in mortars made from aggregates having different degree of crystallinity. 53, 01 2009.

[50] L Monette, J Gardner, and P E. Grattan-Bellew. Structural effects of the alkali-silica reaction on non-loaded and loaded reinforced concrete beams. 01 2010.

[51] S. Multon. Evaluation experimentale et theorique des effets mecaniques de l'alcali-reaction sur des structures modeles. 2003.

[52] J F Toutlemonde F Multon S. S. Chemo mechanical assessment of beams damaged by alkali-silica reaction. 1:500–509, 2006.

[53] S. Muthulingam and B.N. Rao. Effects of rebar on chloride ingress in steel reinforced concrete components. *Journal of Structural Engineering (India)*, 43(2):135 – 149, 2016. Chloride;Chloride ingress into concretes;Concrete cover thickness;Rebars;Spatial and temporal distribution;Spatial and temporal variation;Steel reinforced concrete;Time to corrosion initiation;.

[54] A. Otsuki, G. Dodbiba, and T. Fujita. Measurement of particle size distribution of silica nanoparticles by interactive force apparatus under an electric field. 21:419–423, 07 2010.

[55] Francesco P., Dariusz G., Mateusz W., Bernhard A. Schrefler, and Luciano S. Modeling alkali-silica reaction in non-isothermal, partially saturated cement based materials. *Computer Methods in Applied Mechanics and Engineering*, 225-228:95 – 115, 2012.

[56] S. Hun Park, D. Joo Kim, G. Sung Ryu, and K. Taek Koh. Tensile behavior of ultra high performance hybrid fiber reinforced concrete. *Cement and Concrete Composites*, 34(2):172 – 184, 2012.

[57] M Pathirage, F. Bousikhane, M D Ambrosia, M. Alnaggar, and G. Cusatis. Effect of alkali silica reaction on the mechanical properties of aging mortar bars: Experiments and numerical modeling. page 105678951775021, 01 2018.

[58] B. Persson. Hydration and strength of high performance concrete. *Advanced Cement Based Materials*, 3(3-4):107 – 123, 1996. High performance concrete;High strength concrete;Internal relative humidity;Parallel strength tests;Self desiccation;Split tensile strength;.

[59] Rob B. Polder and Mario R. De Rooij. Durability of marine concrete structures - field investigations and modelling. *Heron*, 50(3):133 – 154, 2005. Blast furnace slag cement;Chloride;Marine environment;Probabilistic model;Reinforcement corrosion;.

[60] Zhaojun R. Influence of water repellent treatment on corrosion of steel in concrete with chloride ingress. volume 368-373, pages 2430 – 2436, Xi'an, China, 2012. Chloride induced corrosion;Chloride ingress;Corrosion current densities;Corrosion in concrete;Corrosion of steel;Corrosion potentials;Half-cell potential;Influence of water;Liquid surface;Mass loss ratio;NaCl solution;Polarization resistance method;Top surface;Water repellent surfaces;Water repellent treatment;Wetting and drying cycles;.

[61] R. Rezakhani and G. Cusatis. Generalized mathematical homogenization of the lattice discrete particle model. pages 261–271, 7 2013.

[62] Multon S. and Sellier A. Multi-scale analysis of alkali–silica reaction (asr): Impact of alkali leaching on scale effects affecting expansion tests. *Cement and Concrete Research*, 81:122 – 133, 2016.

[63] L.F.M. Sanchez, B. Fournier, M. Jolin, and J. Duchesne. Reliable quantification of aar damage through assessment of the damage rating index (dri). *Cement and Concrete Research*, 67:74 – 92, 2015.

[64] V Saouma and L. Perotti. Constitutive model for alkali-aggregate reactions. 103:194–202, 05 2006.

[65] E. A. Schauffert and G. Cusatis. Lattice discrete particle model for fiber reinforced concrete (LDPM-F): I theory. *ASCE Journal of Engineering Mechanics*, 138:826–833, 2012.

[66] J. Smith, G. Cusatis, D. Pelessone, E. Landis, J. O'Daniel, and J Baylot. Discrete modeling of ultra-high-performance concrete with application to projectile penetration. *International Journal of Impact Engineering*, 65(Supplement C):13 – 32, 2014.

[67] M. Staffa. Prevention of cracks in reinforced concrete walls due to hydration. *Beton- und Stahlbetonbau*, 89(1):4 – 8, 1994. Clarification ponds;Hydration heat;.

[68] T. E. Stanton. Expansion of concrete through reaction between cement and aggregate. *Proceedings of the American Society of Civil Engineers*, 66, 1940.

[69] X. Sun, K. Zhao, Y. Li, R. Huang, Z. Ye, Y. Zhang, and J. Ma. A study of strain-rate effect and fiber reinforcement effect on dynamic behavior of steel fiber-reinforced concrete. *Construction and Building Materials*, 158:657 – 669, 2018.

[70] Kim T. and Olek J. Chemical sequence and kinetics of alkali silica reaction part i experiments. *Journal of the American Ceramic Society*, 97(7):2195–2203.

[71] M. Thiery, A. Orcesi, and V. Baroghel-Bouny. Durability design of reinforced concrete structures submitted to carbonation by using an probabilistic modelling. pages 408 – 414, Cape Town, South africa, 2012. Chemical model;Concrete cover;Corrosion of reinforcement;Durability design;Engineering design;Inspection and repair;Material property;Optimal planning;Predictive models;Probabilistic framework;Probabilistic modelling;RC structure;Reliability Index;Target values;Time-dependent;.

[72] Kursat Esat Alyamac Yavuzhan TAS Zulfu Cinar ULUCAN and Merve Acikgenc ULAS. Estimation of concrete strength combining rebound hammer and windsor probe test methods. 09 2017.

[73] T. Vidal, A. Castel, and R. Francois. Corrosion process and structural performance of a 17 year old reinforced concrete beam stored in chloride environment. 37:1551–1561, 11 2007.

[74] A. Villani, E. Busso, K. Ammar, S. Forest, and M. Geers. A fully coupled diffusional-mechanical formulation: numerical implementation, analytical validation, and effects of plasticity on equilibrium. 05 2014.

[75] D. Voechovska, M. Omodikova, Jan P., D. Lehky, and B. Teply. Concrete structures under combined mechanical and environmental actions: Modelling of durability and reliability. *Computers and Concrete*, 20(1):99 – 110, 2017. Chloride ingress into concretes;Concrete carbonation;Durability assessment;Environmental action;Environmental loadings;Mechanical loading;Reinforced concrete beams;Synergy;.

[76] L. Wan-Wendner, R. Wan-Wendner, B. Liang, and G. Cusatis. Analysis of the behavior of ultra high performance concrete at early age. 74:120–135, 08 2016.

[77] L. Wan-Wendner, R. Wan-Wendner, R. Liang, and G. Cusatis. Analysis of the behavior of ultra high performance concrete at early age. 74:120–135, 08 2016.

[78] K. Wille, A. E. Naaman, S. El-Tawil, and G. J. Parra-Montesinos. Ultra-high performance concrete and fiber reinforced concrete: achieving strength and ductility without heat curing. *Materials and Structures*, 45(3):309–324, Mar 2012.

[79] Z. Wu, C. Shi, K. Khayat, and S. Wan. Effects of different nanomaterials on hardening and performance ofultra-high strength concrete (uhsc). *Materials and Structures*, 45(3):309–324, Mar 2012.

[80] R. Yuan Xu. *Shear Resistance of High Strength Concrete I-Beams with Large Shear Reinforcement Ratios*. PhD thesis, Univeristy of Toronto, 2012.

[81] P. Zhang, F.H. Wittmann, T. Zhao, and E.H. Lehmann. Neutron imaging of water penetration into cracked steel reinforced concrete. *Physica B: Condensed Matter*, 405(7):1866 – 1871, 2010.

[82] W. Zhao, B. Wang, L.-J. Zhao, and Zhong-X. Feng. Improving concrete strength based on the mixing process. *Chang'an Daxue Xuebao (Ziran Kexue Ban)/Journal of Chang'an University (Natural Science Edition)*, 35(1):148 – 153, 2015. Activated water;Chemical activities;Condensation rates;Contrast experiment;Critical component;Experimental research;Mixing process;Uniform distribution;.

[83] K. Zheng, P. Adriaensens, G. De Schutter, G. Ye, and L. Taerwe. Studies on the alkali–silica reaction rim in a simplified calcium–alkali–silicate system. *MATERIALS*, 9(8), 2016.

[84] Bažant Z.P. and Panula L. Temperature effect on basic creep. *Materials and structures (RILEM,Paris)*, 11(4), 1978.

[85] A. Steffens Z.P. Bažant. Mathematical model for kinetics of alkali–silica reaction in concrete. *Cement and Concrete Research*, 30(3):419 – 428, 2000.

[86] Y. XI Z.P. Bažant. Drying creep of concrete: constitutive model and new experiments separating its mechanisms. *Materials and structures*, 27:3–14, 1994.